

January 1985

THE VERTICAL REDISTRIBUTION OF A POLLUTANT TRACER  
DUE TO CUMULUS CONVECTION

PROPERTY OF  
DIVISION  
OF  
METEOROLOGY

ATMOSPHERIC SCIENCES RESEARCH LABORATORY  
OFFICE OF RESEARCH AND DEVELOPMENT  
U.S. ENVIRONMENTAL PROTECTION AGENCY  
RESEARCH TRIANGLE PARK, NORTH CAROLINA 27711

THE VERTICAL REDISTRIBUTION OF A POLLUTANT TRACER  
DUE TO CUMULUS CONVECTION

by

John A. Ritter and Donald Stedman  
Department of Atmospheric and Oceanic Science  
The University of Michigan  
Ann Arbor, Michigan 48109

Cooperative Agreement CR807485-01 and 02

Project Officer

Jason K.S. Ching  
Meteorology and Assessment Division  
Atmospheric Sciences Research Laboratory  
Research Triangle Park, North Carolina 27711

ATMOSPHERIC SCIENCES RESEARCH LABORATORY  
OFFICE OF RESEARCH AND DEVELOPMENT  
U.S. ENVIRONMENTAL PROTECTION AGENCY  
RESEARCH TRIANGLE PARK, NORTH CAROLINA 27711

## NOTICE

The information in this document has been funded partly by the United States Environmental Protection Agency under Cooperative Agreements CR807485-01 and -02 to The University of Michigan. It has been subject to the Agency's peer and administrative review, and it has been approved for publication as an EPA document.

## ABSTRACT

### THE VERTICAL REDISTRIBUTION OF A POLLUTANT TRACER DUE TO CUMULUS CONVECTION

by

John Andrew Ritter

This study presents a formalism that incorporates the physical processes responsible for the vertical redistribution of a conservative pollutant tracer due to a convective cloud field and demonstrates that the cloud venting process should not be neglected in regional-scale modeling.

Two modeling approaches are presented which, although both are based on the framework common to the works of Ogura and Cho (1973) and Johnson (1975), differ in the manner in which the cloud field is forced. In the first approach (herein called the implicit model), which is adapted from Johnson (1975), the vertical cloud development is limited by the satellite observed value, but the cloud forcing is determined solely from synoptic-scale heat and moisture budgets. In the second approach (herein called the explicit model), the vertical development is similarly limited, but the forcing functions are obtained in a unique way by explicitly incorporating the vertical distribution of cumulus cloud cover, thereby dynamically incorporating the influences of subsynoptic-scale phenomena. By comparing the results of the implicit and explicit models, we may gain some insight into the importance of subsynoptic-scale phenomena in determining the vertical pollutant transport due to cumulus convection.

The two models give internally consistent results for varying conditions and give similar results for the total convective upward mass flux ( $M_U$ ). The manner in which the upward mass flux is apportioned to the various cloud classes, however, differs for the two models and is shown to affect the vertical profile of detrainment for a conservative tracer. This is seen as a consequence of the vertical profile of forcing functions used in the respective models. Although the explicit model gave more reasonable profiles, the absolute values stemming from this model must be viewed with caution due to the sensitivity of the model to its required input. The implicit model, on the other hand, whose forcing functions are devoid of subsynoptic-scale effects, demonstrated an acceptable sensitivity to its input parameters if the data are prepared judiciously.

This study has provided two methods by which satellite data can be used to incorporate the subscale effects of cumulus clouds into regional transport models. It has also been shown that regardless of the method chosen, the concentration increase in the cloud-layer due to the venting action of cumulus clouds can be as, if not more important than, the in-situ production of some species and should therefore not be neglected in regional-scale transport models for scenarios involving convective cloud fields.

## TABLE OF CONTENTS

Abstract.....	iii
List of Tables.....	vi
List of Illustrations.....	vii
Acknowledgements.....	xii
Chapter	
1. Introduction.....	1
2. The Parameterization of Convective Cloud Venting.....	15
2.1 Model Perspective.....	15
2.2 Data Preparation.....	36
a) Synoptic-scale analysis.....	36
b) Surface analysis.....	55
c) Satellite data.....	58
d) Other data fields.....	66
2.3 The Entraining Plume Model.....	66
2.4 Determination of the Convective-scale Forcing from Synoptic-scale Variables.....	76
2.5 Determination of the Convective-scale Forcing from a 'Bulk' Perspective.....	80
2.6 Determination of the Convective Cloud Mass Flux..	91
3. Model Evaluation and Intercomparison.....	98
4. Sensitivity Analysis.....	123
5. Summary and Conclusions.....	131
Bibliography.....	136
Appendices.....	143

## LIST OF TABLES

Table 3-1.	Basic characteristics of the cloud field for each grid cell chosen for an evaluation of the models presented. Units of heat flux are $\text{W m}^{-2}$ (ex: explicit model; im: implicit model).....	99
Table 4-1.	Sensitivity analysis of the explicit model to the selection of the lower limit of integration in Equation (52).....	124
Table 4-2.	Sensitivity analysis of the explicit model to the selection of the approximate minimum bound for the determination of cloud half-lives.....	125
Table 4-3.	Sensitivity analysis of the explicit model to the selection of $\Delta H/Z_1$ .....	126
Table 4-4.	Sensitivity analysis of the implicit model to the profiles of $Q_R$ , $Q_1$ , $Q_2$ , $\partial\lambda/\partial p$ and $q_d$ .....	127
Table 4-5.	A budget analysis for the terms comprising $Q_1$ and $Q_2$ as given by Equations (41) and (42) respectively. The data are taken from that of case #1 at 700 and 800 mb. Units: $^{\circ}\text{K day}^{-1}$ .....	128

## LIST OF ILLUSTRATIONS

Figure 1-1.	The vertical distribution of mixed layer air due to the diurnal oscillation of the mixed layer height is illustrated. Parcels transported to the upper region of the mixed layer may become trapped at that level due to the termination of positive heat flux. Parcels in this region are transported by different mechanisms at night than those in the nocturnal boundary layer.....	3
Figure 1-2.	A depiction of the cloud venting process is shown. A cloud-base mass flux, $m_u$ , enters the cloud from the mixed layer. Cloud layer air enters the sides of the cloud by the entrainment process. Clouds detrain at their respective cloud tops. The total upward mass flux from the clouds induces a subsidence in the between cloud environment ultimately injecting cloud layer air into the mixed layer.....	5
Figure 2.1-1.	The Regional Oxidant Model domain with the network of 60 by 42 grid cells is shown. The dimensions of each grid cell are $1/4^\circ$ longitude by $1/6^\circ$ latitude.....	17
Figure 2.1-2.	Summer Experiment study area with individual $1/4^\circ$ longitude by $1/6^\circ$ latitude grid cells indicated....	18
Figure 2.1-3.	Box diagram showing the basic components of the modeling approaches used in this study.....	21
Figure 2.1-4.	Satellite photograph of the Summer Experiment study area for 2331Z 7/22/81.....	23
Figure 2.1-5.	The distribution of clouds in a hypothetical grid cell is illustrated. The dot(s) or circle(s) represent hypothetical updrafts for the clouds shown.....	24
Figure 2.1-6.	The model used in this study depicts a real cloud field by: (a) choosing a distribution of cloud updrafts to represent the ensemble of clouds present, and by (b) combining the updraft elements of the same height class (shown in part (a) of this figure) while conserving the total updraft area.....	25



Figure 2.1-7.	Model derived entrainment rates are assigned on the basis of cloud-top height, implying that taller clouds have entrained less and therefore have retained more of their buoyancy than shorter clouds have.....	27
Figure 2.1-8.	UV-DIAL depiction of pollutant stratification in the cloud layer.....	29
Figure 2.1-9.	A schematic solution of the integral equation used to determine the cloud-base mass flux is presented. On the left side is a model cloud field (analogous to that in Figure 2.1-6(b). On the right side is the vertical profile of the forcing terms.....	33
Figure 2.2-1.	The spatial distribution of the rawinsonde observation sites used in the analysis of the Summer Experiment observational program, July 1981 is shown above. The enclosed region represents the study area.....	38
Figure 2.2-2.	The computational grid domain used for the synoptic-scale analysis of the rawinsonde data is shown above. The enclosed region represents the study area.....	39
Figure 2.2-3.	A schematic depiction of how the first derivative of a feature with a wavelength $\lambda$ could be misrepresented by not having grid points located $1/4 \lambda$ apart. A '+' indicates where additional grid points should be located.....	40
Figure 2.2-4.	Objectively analyzed 500 mb geopotential heights (gpm) for 00Z 7/23/81.....	43
Figure 2.2-5.	Objectively analyzed 500 mb temperature (K) for 00Z 7/23/81.....	44
Figure 2.2-6.	Objectively analyzed 500 mb specific humidity ( $\times 10$ g/kg) for 00Z 7/23/81.....	45
Figure 2.2-7.	A schematic representation of a situation in which the interpolation of the horizontal components of the wind field do not yield the same results as the interpolation of the wind speed (see text for discussion).....	46
Figure 2.2-8.	Synoptic-scale relative vorticity fields ( $\times 10^6 \text{ s}^{-1}$ ) at 500 mb for 00Z 7/23/81: (a) from initial u and v component interpolation, (b) from the interpolated centroid point values of $\zeta$ and	

	(c) from the final wind field determined from Equation (9).....	49
Figure 2.2-9.	Synoptic-scale divergence fields ( $\times 10^6 \text{ s}^{-1}$ ) at 500 mb for 00Z 7/23/81: (a) from initial u and v component interpolation, (b) from the interpolated centroid point values of $\delta$ , and (c) from the final wind field determined from Equation (9).....	50
Figure 2.2-10.	Wind field (kt) at 500 mb for 00Z 7/23/81: (a) from initial u and v component interpolation, (b) from the Schaefer-Doswell variational technique.....	51
Figure 2.2-11.	Vertical velocity field ( $\text{mb hr}^{-1}$ ) at 500 mb for 00Z 7/23/81.....	54
Figure 2.2-12.	The spatial distribution of surface meteorological observation sites used in the analysis of the Summer Experiment observational program, July 1981.....	56
Figure 2.2-13.	The computational grid domain used for the surface meteorological data is shown above. The enclosed region represents the study area.....	57
Figure 2.2-14.	Surface observations of (a) temperature (K), and (b) dew-point temperature (K) for 00Z 7/23/81.....	59
Figure 2.2-15.	An illustration of the process by which the frequency distribution of cumulus cloud-top heights is used to give the vertical distribution of fractional cumulus cloud cover: (a) profile of IR pixel data obtained from satellite observations; (b) the corresponding profile of cumulus cloud coverage via a regression analysis between observed IR pixel data and fractional cumulus cloud cover observed from the satellite visible imagery; and (c) final normalized cloud cover distribution.....	63
Figure 2.2-16.	Regression curve showing the relationship between the IR pixel count and the area of cumulus coverage.....	65
Figure 2.3-1.	A vertical profile of the normalized mass flux distribution of $\eta(\lambda_1, p)$ , for a typical cloud class.....	69

Figure 2.3-2.	Example of model derived entrainment rates $\lambda_1(p)$ ...	75
Figure 2.5-1.	An illustration of the entrainment zone which exists between the mixed layer and the more stable cloud layer above is shown. $H_2$ represents the highest level to which mixed layer air can penetrate. $H_1$ marks the highest level at which most of the air can be identified as mixed layer air.....	83
Figure 3-1.	(a) fractional cumulus cloud coverage as a function of pressure as determined from satellite data, and (b) model derived entrainment rates as a function of cloud class for cell (5,20) at 20Z (case #1).....	100
Figure 3-2.	(a) fractional cumulus cloud coverage as a function of pressure as determined from satellite data, and (b) model derived entrainment rates as a function of cloud class for cell (7,20) at 20Z (case #2).....	101
Figure 3-3.	(a) fractional cumulus cloud coverage as a function of pressure as determined from satellite data, and (b) model derived entrainment rates as a function of cloud class for cell (12,16) at 20Z (case #3).....	102
Figure 3-4.	Vertical mass flux distribution for (a) explicit model, and (b) implicit model at 20Z (case #1).....	105
Figure 3-5.	Cloud-base mass flux distribution $m_B(p)$ for (a) explicit model, and (b) implicit model at 20Z (case #1).....	106
Figure 3-6.	Concentration increase in the cloud layer of a conservative tracer assuming a mixing ratio of 60 ppbv in the mixed layer and 40 ppbv in the cloud layer for (a) explicit model, and (b) implicit model at 20Z (case #1).....	108
Figure 3-7.	Vertical mass flux distribution for (a) explicit model, and (b) implicit model at 20Z (case #2).....	110

Figure 3-8.	Cloud-base mass flux distribution $m_B(p)$ for (a) explicit model, and (b) implicit model at 20Z (case #2).....	112
Figure 3-9.	Concentration increase for the same conditions of Figure 3-6 for (a) explicit model, and (b) implicit model at 20Z (case #2).....	113
Figure 3-10.	Vertical mass flux distribution for (a) explicit model, and (b) implicit model at 20Z (case #3).....	115
Figure 3-11.	Cloud-base mass flux distribution $m_B(p)$ for (a) explicit model, and (b) implicit model at 20Z (case #3).....	116
Figure 3-12.	Concentration increase for the same conditions of Figure 3-6 for (a) explicit model, and (b) implicit model at 20Z (case #3).....	118

## ACKNOWLEDGEMENTS

The work presented in this report is the culmination of the efforts of several people, all to whom I am gratefully indebted. This research topic was suggested to me by Dr. Jason Ching. I am grateful to him for the many fruitful discussions we have had and for the continued support for my work that he has shown. The enthusiasm, energy and personal interest exuded by my major advisor, Dr. Donald Stedman, did much to help me over numerous research and academic hurdles in the past several years. His friendship and example as a scientist has influenced me greatly during this period. I have benefited greatly from the insightful suggestions given to me by Dr. Francis Binkoski. Mr. O. Russell Bullock was extremely helpful in providing a firm base from which to start. The technical support of Adrian Busse, Dale Coventry, and Jim Regan has been invaluable. Administrative responsibilities were admirably fulfilled by Bobbi Walunas.

I would also like to thank the Meteorology and Assessment Division of EPA for providing me with the environment and computer resources necessary for the completion of this work which was funded by EPA under Cooperative Agreements CR807485-01 and -02.

## CHAPTER 1

### INTRODUCTION

In recent years there has been an increasing awareness and concern over the fate of pollutants that are emitted as a result of normal human activity and their resulting impact on the air quality and ultimately on the quality of human life for those who reside in the wake of the pollutant plume. Several studies have shown that pollutants are capable of being transported over long distances. Spicer et al. (1977) along with White et al. (1976) have shown that urban pollutant plumes can be identified up to 250 km from their sources. Wolff et al. (1977) have similarly shown enhanced ozone concentrations along the 'northeast corridor' extending from Washington, D.C., to Boston, Mass. The long-range transport of ozone under high pressure conditions has also been addressed by Samson and Ragland (1977). With the advent of faster computers and the knowledge gained from previous studies, the level of complexity of the numerical models used to study the transport and transformation processes of pollutants has increased tremendously (Rodhe and Crutzen, 1981; Baboolal et al., 1981; Eliassen et al., 1982; Lamb, 1983). Johnson (1983) reviews several different modeling approaches used today in the study of the long-range transport and transformation of pollutants.

The horizontal transport of pollutants has been the focal point of many of the current transport models. However, pollutants are also

subject to vertical dispersion above the mixed layer due to several mechanisms. Figure 1-1 illustrates the vertical redistribution of mixed-layer pollutants as a result of the diurnal oscillation of the mixed-layer height (Carson, 1973; Manins, 1982). We see from the figure that pollutants emitted into the mixed layer during the period of strong daytime convection become well-mixed throughout the layer. However, as the surface-heat flux subsides in the late afternoon, the pollutants located in the upper region of the layer remain there as the mixed-layer height collapses. Eventually, a nocturnal inversion is established which separates the now aged mixed layer, above the nocturnal inversion base, from the surface layer. The pollutants in the inversion layer, which were of mixed layer origin, are now free to be advected independently of the transport occurring in the surface layer (Zeman, 1979).

Another mechanism by which pollutants can be vertically dispersed is through the action of convective clouds. The role that such clouds play in influencing the transport and transformation of pollutants has received increasing attention in the past few years. Emmitt (1978) has traced the mixed-layer thermals associated with convective clouds from just above the cloud base to the surface. This indicates that pollutants emitted in the surface layer are able to be transported vertically into the cloud layer as a result of these 'cloud roots'. This upward transport of mixed-layer air causes a compensating amount of cloud layer air, deficient in pollutant load, to return to the mixed layer thereby diluting the mixed-layer concentrations. As a result of this process, the mixed-layer height, another important variable in transport models, is modulated. These processes are

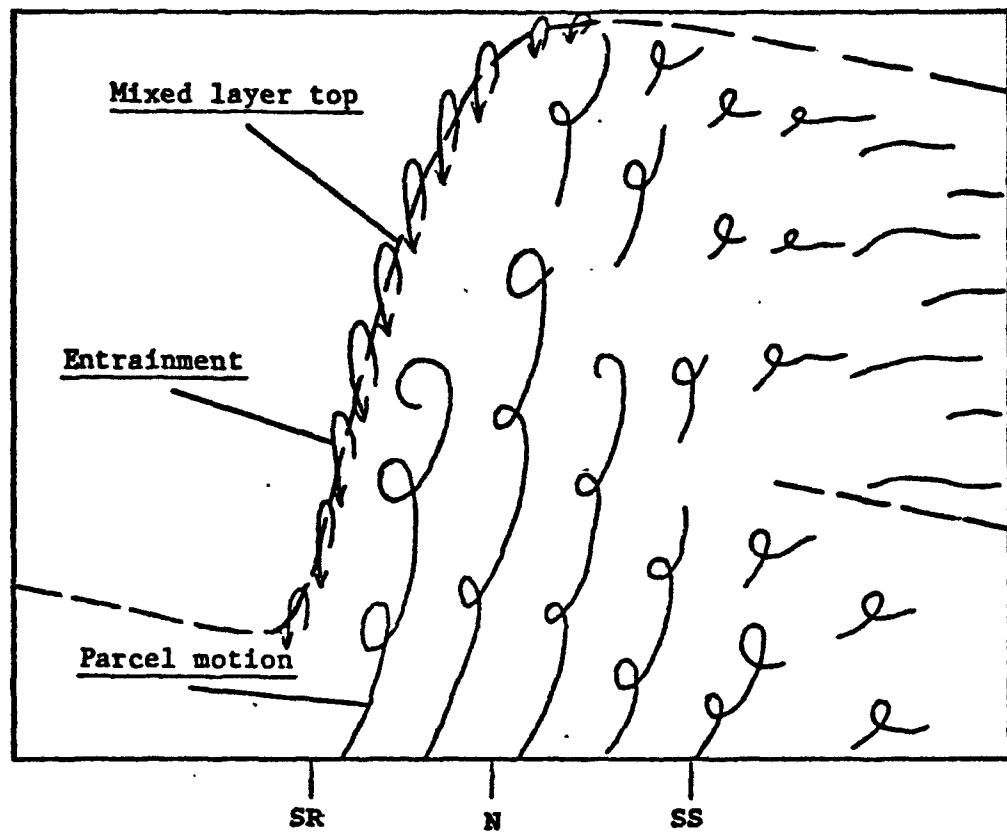


Figure 1-1. The vertical distribution of mixed layer air due to the diurnal oscillation of the mixed layer height is illustrated. Parcels transported to the upper region of the mixed layer may become trapped at that level due to the termination of positive heat flux. Parcels in this region are transported by different mechanisms at night than those in the nocturnal boundary layer.



illustrated in Figure 1-2, where  $m_u$  indicates the upward mass flux (in units of mass area<sup>-1</sup> time<sup>-1</sup>) entering through the cloud bases and where  $\bar{M}$  represents the downward compensating mass flux of cloud-layer air. Other studies have shown how the presence of clouds can modify the thermodynamic structure of the subcloud layer (Deardorff, 1975; Betts, 1976; Seguin and Garstang, 1976; Johnson, 1976). Convective clouds have long been known to redistribute heat and moisture (Riehl and Malkus, 1958, 1961; Ooyama, 1964; Charney and Eliassen, 1964; Kuo, 1965; Yanai et al., 1973; Arakawa and Schubert, 1974; Johnson, 1976). However, to date, the field of air pollution meteorology has been virtually silent about the influence these clouds may have in vertically redistributing pollutants. The proper treatment of this process must be incorporated into long-range transport models if the results are to be considered credible.

As a result of the growing concern for a more realistic depiction of the physical processes involved in long-range transport, the U.S. Environmental Protection Agency (EPA) has initiated the Northeast Corridor Regional Modeling Project (NECRMP). The focal point of this project is the development of the Regional Oxidant Model (ROM), a regional-scale Eulerian transport and photochemistry model (Lamb, 1983). In order to initialize and validate this model, several field studies have been undertaken, the results of which are summarized by Clarke et al. (1983). The results of these observational programs have given even more evidence of the importance of convective clouds in venting pollutants from the mixed layer (Vaughan et al., 1982). An especially interesting observation was made by Greenhut et al. (1983). They observed peak ozone concentrations of 130 ppb over Philadelphia's

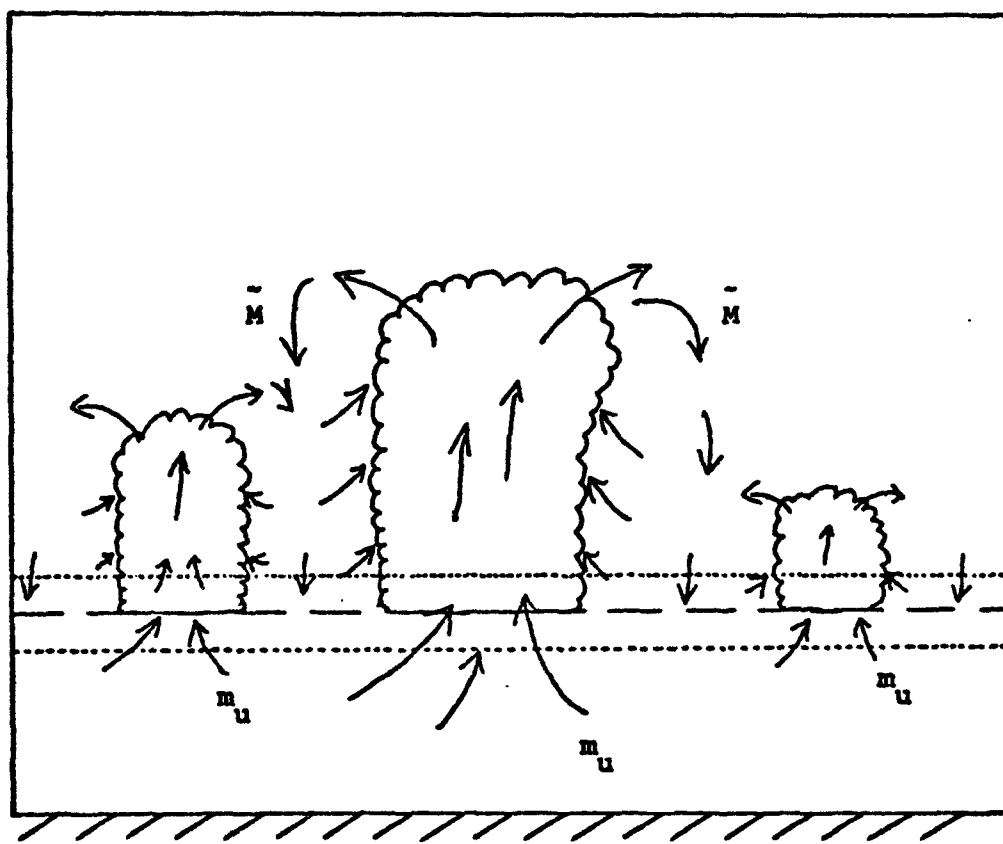


Figure 1-2. A depiction of the cloud venting process is shown. A cloud-base mass flux,  $m_u$ , enters the cloud from the mixed layer. Cloud layer air enters the sides of the cloud by the entrainment process. Clouds detraining at their respective cloud tops. The total upward mass flux from the clouds induces a subsidence in the between cloud environment ultimately injecting cloud layer air into the mixed layer.

urban area, whereas to the southeast and northwest values of 90 ppb were observed. In addition, in a cloud penetration by an aircraft they estimated that the flux of ozone in the updraft was two orders of magnitude larger than the turbulent eddy flux. These observations indicate that turbulent diffusion alone is inadequate to account for the redistribution of pollutants due to the presence of a convective cloud field and that the effects of the updrafts that are associated with these clouds must be incorporated into pollutant transport models.

Until the recent studies of Chatfield (1982) and Gidel (1983), the process of cloud venting was either ignored or a bulk eddy-diffusion constant was assumed (Chameides and Stedman, 1977; Liu, 1977). Chatfield used transition probabilities to parameterize the effects of cloud transport on various sulfur species in the tropics, while Gidel used an approach similar to the one proposed in this work. Although both of these works reached the important conclusion that an increasing specie mixing ratio with height in the free troposphere can be explained by the venting action of cumulus clouds, both works used an assumed distribution of vertical mass transport due to clouds. In the present work the distribution of cloud-base mass flux used to describe the vertical redistribution of a conservative tracer will not be assumed a priori, but will be determined by the model.

Parameterization techniques for determining how clouds influence, and are forced by, the large-scale thermodynamic fields have come through a long evolution. A brief history of this evolution will now be given so that a better perspective of this complex problem can be obtained.

The depth to which clouds may penetrate depends on the environmental profiles of temperature, moisture, and wind shear. Methods used to determine the extent of growth vary. Two fundamental approaches, however, are the parcel method and the slice method. In the parcel method, a parcel of cloud air is assumed to follow the moist adiabat upwards on an adiabatic diagram. The intersection of this moist adiabat and the line representing the environmental lapse rate defines the cloud top. In the slice method, Bjerknes (1938) allowed compensating, unsaturated downward motion to match the saturated ascent of the cloud parcel by applying the continuity equation as a constraint. This induced motion acts to dry and warm the environment by adiabatic compression, thereby altering the environment by increasing the stability of the cloud layer. In addition, the subsidence field acts to retard the growth of the mixed layer (Johnson, 1978; Pielke, 1974). If this process were allowed to continue, the convection could actually be cut off in that the subsidence field may cause the mixed-layer height to decrease until the moisture supply is no longer sufficient to sustain the cloud field. Therefore, in order for the convection to be maintained, a forcing mechanism must exist that will counteract the effects of stabilizing subsidence motion. Several such mechanisms exist. Over land, the diurnal heating of the surface layer, topographical influences, and land-sea breeze convergence zones are typical examples of these mechanisms. Over oceanic regions, however, the convergence of moist-air provides the major impetus for cloud growth. Bjerknes (1938) also found that the greatest efficiency of convection was attained when the area of the rising air was only a small percentage of the total area. This is an important point, the

relevance of which will be discussed in this work. The inclusion of synoptic-scale vertical motion into this framework was done by Cressman (1946), thereby allowing the dynamics of the environment to influence cloud development.

A major weakness of the slice method is that no provision has been made for the entrainment of environmental air into the cloud parcel. It has been observed, for example (Warner, 1955; Squires, 1958), that the water content in nonprecipitating cumulus clouds can not be approximated by the mixed-layer water-vapor mixing ratio, hence implying the existence of the entrainment process. Stommel (1947, 1951) envisioned the entrainment process in terms of a turbulent stream or 'jet' moving through a nonturbulent environment. In his studies, he determined the rate of entrainment from profiles of temperature and specific humidity taken both inside and outside of cumuli. Due to the continual entrainment of outside air, the mass flux within the jet was shown to increase with height. Scorer and Ludlam (1953) introduced the 'bubble' or thermal model for convection. This model, most applicable to small cumuli, models the rising element as a puff of air that expands as if it were contained in a conelike container with the vertex at the originating point of the thermal. Unlike the plume or jet approach of Stommel, entrainment in this model occurs at the leading face of the bubble. Squires and Turner (1962) furthered the development of the entraining plume or 'jet' proposed by Stommel by employing the results of Morton (1957) who found that the inflow velocity from a quiescent environment is proportional to the upward 'jet' velocity. The thermodynamical treatment of Squires and Turner was built on a firmer physical basis than previous efforts

and yielded results of in-cloud properties that were reasonably consistent with the available observational data. The latter two mixing models (plume or jet and bubble) have served as the basis for convection models up to the present. As would be expected, each method has strengths and weaknesses. As for the plume model, any mixing at the top, or leading face of the plume, is neglected. It is also assumed that the plume detrains into the environment only at the cloud top. The bubble theory, on the other hand, is incapable of treating rising thermals from a steady source, either below or within the bubble itself.

The previous discussion has dealt only with a single cloud element. However, if conditions present are conducive to cloud growth, as a result of any of the aforementioned mechanisms, a population, or ensemble, of clouds instead of a single cloud will actually be formed. The relationship, however, between such a convective cloud population and the larger synoptic field is a complex one that is not yet fully understood. Riehl and Malkus (1958, 1961) made some of the first advances in understanding this relationship. Their work showed that the transport of sensible heat and water vapor by cumulus clouds in the tropics is important in maintaining the energy budget of the tropical atmosphere. Efforts to parameterize this relationship could be categorized into three basic approaches: convective adjustment, boundary-layer convergence, and moisture convergence through an entire air column. A complete review of these methods is provided by Bates (1972) and will be briefly described here.

In the convective adjustment technique (Manabe and Strickler, 1964) the conditional instability of a layer is removed in such a way

that the total energy is conserved. Realizing that the tropical boundary layer has a high moisture content relative to the air above, Ooyama (1964), along with Charney and Eliassen (1964), related the convergence of moisture in the boundary layer to the growth rate for tropical cyclones. Charney and Eliassen named this process the Conditional Instability of the Second Kind (CISK). This was an important development since in this process the synoptic-scale features actually cooperate with a population of cumulus clouds, in that the cumulus clouds provide the heat which aids the growth of the synoptic-scale waves while the synoptic-scale feature supplies the moisture that maintains the cumulus clouds. Kuo (1965) parameterized the growth of tropical cyclones in terms of the net moisture convergence integrated over an entire column of the atmosphere and added to this the evaporation from the sea surface.

Ooyama (1971) was the first to introduce the concept of an ensemble, or spectrum of cloud sizes. The ensemble was defined in terms of a dispatcher function which gives the rate of generation of bubbles from the surface layer. The issue of a cloud spectrum was again addressed by Arakawa and Schubert (1974). They pointed out that the parameterization scheme used by Ooyama (1971) was not closed since the exact nature of the dispatcher function was not known. They closed the parameterization problem by explicitly linking the characteristics of a cumulus ensemble to the large-scale fields of temperature, moisture and radiative cooling. Their results showed that cumulus detrainment cooled and moistened the environment while the cumulus induced subsidence caused large-scale warming and drying. The cloud ensemble they employed was divided into cloud classes based

on the fractional rate of mass entrainment, which was uniquely described for each cloud class. The budgets of moist static energy, mass and total water content were then determined for each cloud class. The cloud-base mass flux was subsequently determined by the solution of these budget equations subject to the environmental profile of moist static energy and the forcing resulting from the large-scale fields of temperature, moisture and radiative cooling. Their method was designed to be used in the U.C.L.A. general circulation model and was prognostic in nature. The control of the cloud field in the temporal sense was accomplished by defining a cloud work function which is a measure of the kinetic energy generation for each cloud class. The required assumptions were that each cloud class be in a 'quasi-equilibrium' with the large-scale forcing and that the region under consideration is small in comparison to the large-scale, but large enough to contain a statistically representative sample of the cloud population.

Ogura and Cho (1973) and Nitta (1975) have used the Arakawa-Schubert theory in a diagnostic sense to determine how, for different situations, the cumulus field interacted with, and was determined by, the large-scale budgets of heat and moisture. Cho and Ogura (1974) applied this same approach to yet another tropical data set and found that deep and shallow cumulus clouds were controlled by separate mechanisms. Lewis (1975) tested the diagnostic model described above on a situation involving a prefrontal squall line. He compared the observed frequency of tall clouds (from a WSR-57 radar) and total area covered, to that obtained from the model with favorable results. Johnson (1975, 1976) incorporated convective-scale downdrafts into



the diagnostic approach of Ogura and Cho (1973) and found that the magnitude of the downdraft mass flux in the lower troposphere was between one-quarter and one-half that of the updraft mass flux. He concluded that neglecting the contribution of convective-scale downdrafts to the net mass flux budget in precipitating cases could result in an excessively warm and dry lower troposphere. Johnson (1977) incorporated lateral detrainment into his diagnostic model, following the results of Fraedrich (1976) who found that lateral detrainment and not cloud top detrainment was the dominant detrainment mechanism. Johnson found that the inclusion of this process may decrease the net cumulus mass flux by 15% - 20%. Johnson (1980) further modified the diagnostic model to include the effects of mesoscale downdrafts.

As the above discussion indicates, the formalism of the Arakawa-Schubert approach has proven to be flexible in regard to the inclusion of additional mechanisms that may provide a more realistic depiction of the actual interaction between the convective and large-scale fields. It should be noted that neither the Arakawa-Schubert scheme nor its diagnostic counter-part require any empirical or observed cloud data as input. This can be very advantageous when working with, for example, a data set that is zonally averaged or when only rawinsonde data are available. There are however, two major problems that are encountered when this approach is applied to a mid-latitude situation on a regional scale with a grid spacing of  $\approx 20$  km on a side. The first problem is the assumption that each grid cell contains a representative sample of the cumulus population. This may be easily violated if only a few cumulonimbus clouds (with a radius of approximately 5 km) are present in the cell. Secondly, the

connection between the large-scale and convective-scale motions, as defined by the synoptic-scale rawinsonde data, precludes the ability of the model to be influenced by forces or phenomena that have spatial scales smaller than that of the rawinsonde separation distance or time scales shorter than the 12 hours between rawinsonde observations. Examples of these phenomena would be land-sea breeze circulations (Pielke, 1974), orographic influences (Orville, 1968), mesoscale convergence patterns (Fritsch and Maddox, 1981a,b; Chen and Orville, 1980), or inhomogeneities caused by differing land use patterns.

In regard to the first problem mentioned above, it will be pointed out later in this work that the limitations of this problem may be mitigated if a frequency distribution of cumulus cloud top heights is available to augment the input data. It will also be shown that the limitations inherent to the second problem mentioned above can be avoided if the same frequency distribution is used to directly force the cloud field; although in this case, some of the calculations are sensitive to parameters that may be difficult to determine in an operational sense.

The process of cloud venting is a very complex one due to the spatial distribution, temporal nature, and subgrid-scale nature of these clouds. This study presents a formalism, based on the diagnostic counterpart of the Arakawa-Schubert scheme, that incorporates the physical processes responsible for the vertical redistribution of a conservative pollutant tracer due to a convective cloud field and demonstrates that the cloud venting process should not be neglected in regional-scale modeling.

The following chapter describes the parameterization techniques utilized in this study, as well as a description of the various data bases employed and how they were determined. The results of the modeling approaches used are described in Chapter 3. A sensitivity analysis is provided in Chapter 4, while Chapter 5 presents a summary of the findings of this study.

## CHAPTER 2

### THE PARAMETERIZATION OF CONVECTIVE CLOUD VENTING

#### 2.1 Model Perspective

This section will give a broad overview of the modeling approaches employed herein. The overview will include a discussion on the goal and motivation for this study, as well as an outline of some of the problems encountered and assumptions inherent to the approaches taken. The mathematical formalization for these approaches will be presented in detail in Sections 2.3 - 2.6. The preparation and description of the data bases used in this study are outlined in Section 2.2.

The goal of this study is to determine the impact that cumulus clouds have on venting a conservative tracer from the subcloud layer and to investigate the subsequent redistribution of the tracer in the vertical. Two modeling approaches are presented which, although both are based on the framework common to the works of Yanai et al., (1973, 1976), Ogura and Cho (1973), Arakawa and Schubert (1974), Nitta (1975) and Johnson (1975, 1977), differ in the manner in which the cloud field is forced. The first approach (called an implicit model) is adapted from Johnson (1975) wherein the cloud forcing functions are determined from the synoptic-scale heat and moisture budgets as determined from rawinsonde and radiative cooling data. Realizing that clouds may also be forced from subsynoptic-scale phenomena, an

alternative model (called an explicit model) was developed to provide a formalism in which satellite data can be used in a unique way to determine the cloud forcing functions for use in the above framework. By comparing the results of the implicit and explicit models, we may gain some insight into the importance of subsynoptic-scale phenomena, which have not been dynamically included into the implicit model, in determining the cloud-top detrainment of a conservative pollutant that has been vented from the subcloud layer.

The motivation for this effort was to develop a formalism that could be integrated into EPA's ROM (Lamb, 1983) which would account for the influence that a convective cloud field has on subcloud layer pollutant levels. Since the ROM will be used to study the transformation and transport of pollutants across the northeast quadrant of the U.S., an assessment of the influence that such a cloud field may have on the subcloud pollutant levels would be of great value. The related study area for the ROM is shown in Figure 2.1-1. The model domain is comprised of a network of 60 by 42 grid cells. The dimensions of each grid cell are  $1/4^\circ$  longitude by  $1/6^\circ$  latitude. It is this scale on which the calculations of cloud-base mass flux will be made. Since the ROM is not yet fully operational, the models presented in this report will be applied to the region associated with the Summer Experiment study conducted jointly by the National Aeronautics and Space Administration (NASA) and the EPA during July 1981. Figure 2.1-2 illustrates the Summer Experiment study area. The dimensions of the grid cells have been chosen to match those of the ROM in order to facilitate the subsequent adaptation of the models described in this report into said model.

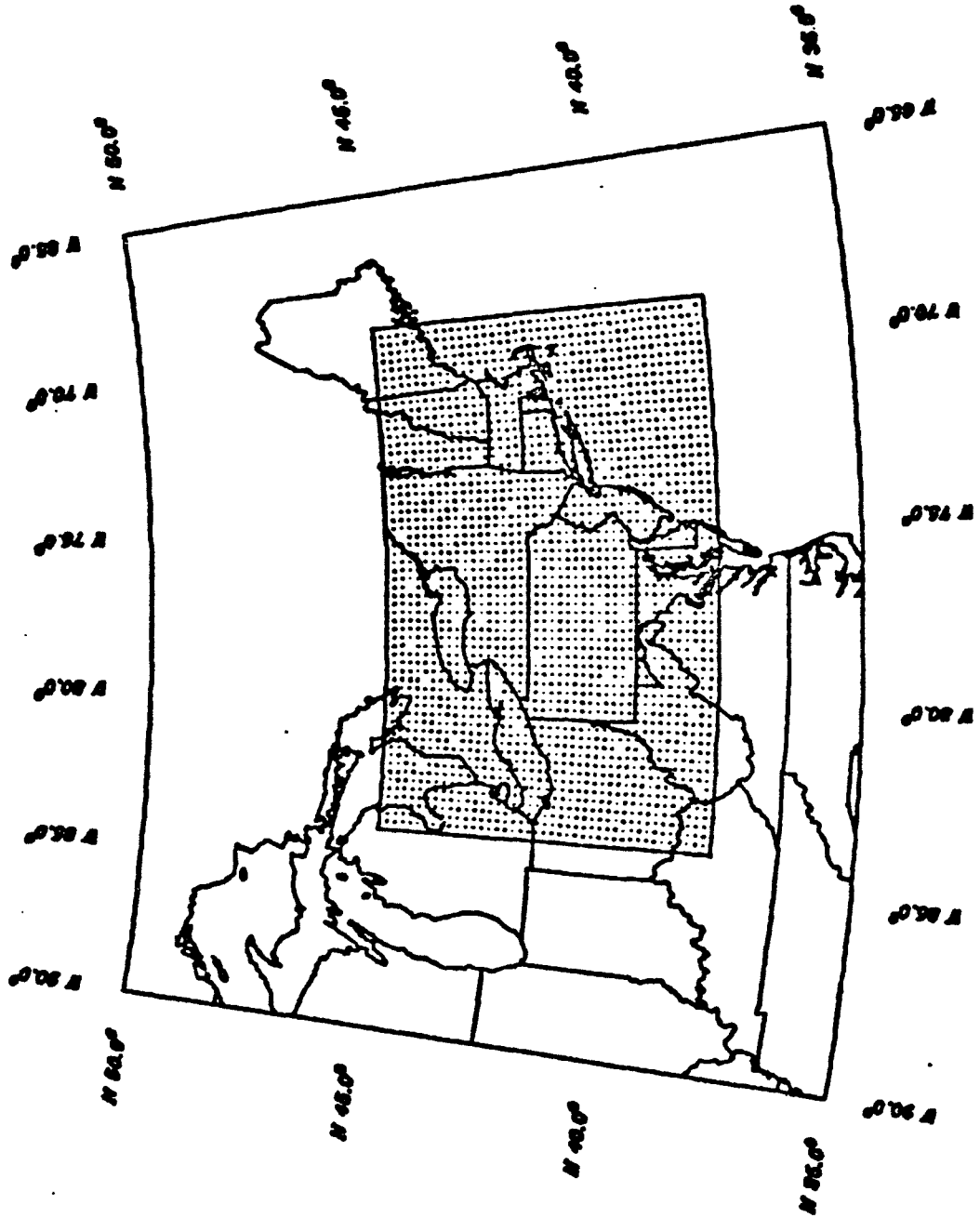


Figure 2.1-1. The Regional Oxidant Model domain with the network of 60 by 42 grid cells is shown. The dimensions of each grid cell are  $1/4^\circ$  longitude by  $1/6^\circ$  latitude.

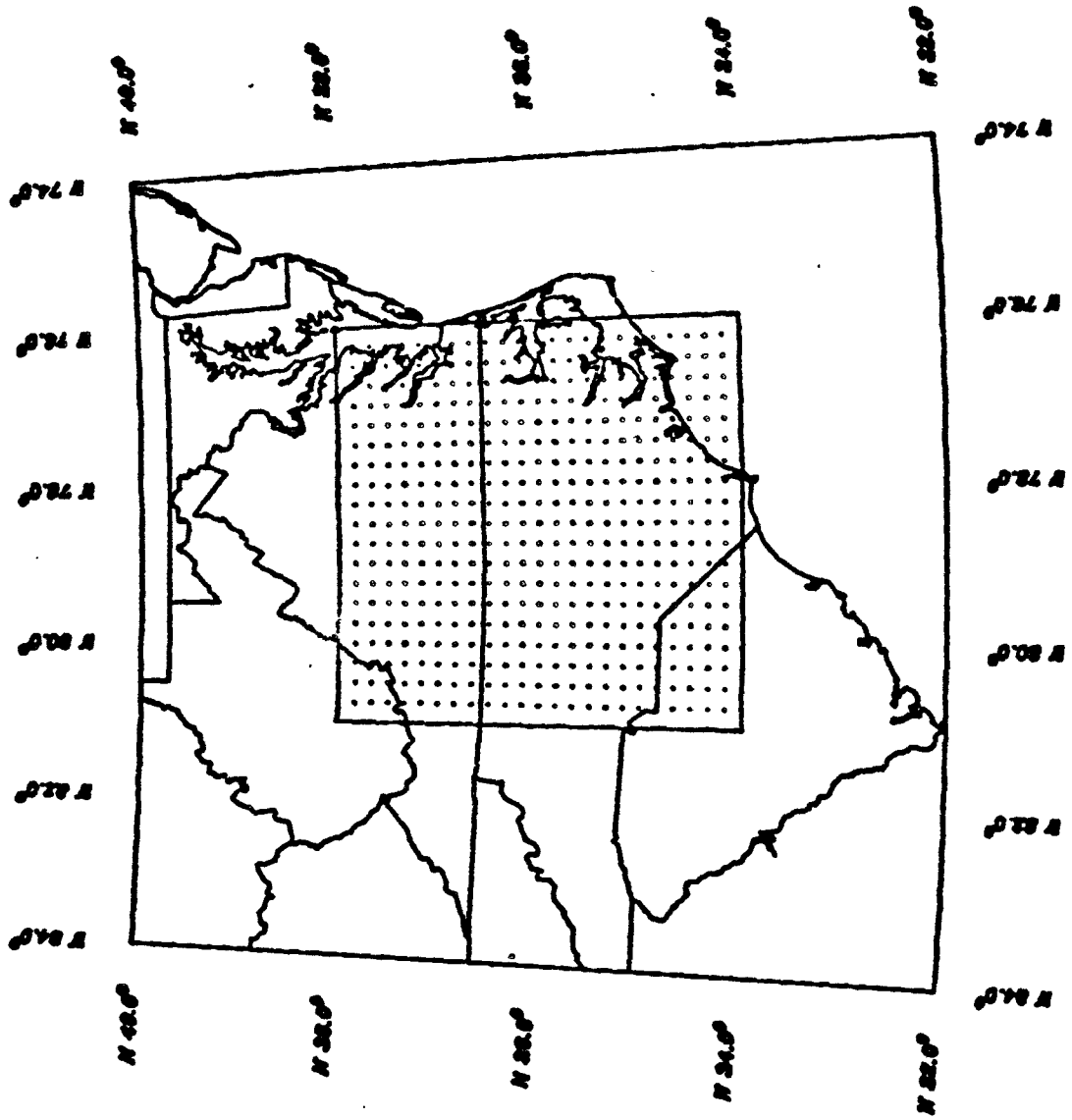


Figure 2.1-2. Summer Experiment study area with individual  $1/4^\circ$  longitude by  $1/6^\circ$  latitude grid cells indicated.

If an account is to be made of the vertical transport of pollutants due to convective clouds, one must not only incorporate the appropriate physics of the process, but one must also require that the real cloud field, as determined from satellite imagery, be adequately depicted by the model cloud field. This is one example of an instance where an actual process or situation has to be approximated by a numerical idealization of the same. As is the case in any modeling approach, many assumptions will have to be made in the course of this work. Some of the assumptions, however crude they may seem to be, are actually at the state-of-the-art and only underscore the need for more observational programs so that these assumptions can be refined.

The basic tool used for this study (for both the implicit and explicit approaches) is the one-dimensional steady-state entraining plume model (Simpson, 1971; Stommel, 1947), realizing that questions still exist as to its usefulness (Warner, 1970). This approach has been used by several authors (Yanai et al., 1973; Arakawa and Schubert, 1974; Ogura and Cho, 1973; Nitta, 1975; Johnson, 1975, 1977) to determine the redistribution of heat and moisture due to cumulus ensembles. These authors related the convective-scale updraft flux of moist static energy to the cloud forcing functions determined from the synoptic-scale heat, moisture and radiation budgets. The updraft flux of moist static energy was then parameterized in terms of the cloud-base mass flux via the one-dimensional steady-state entraining plume theory. Therefore, once the cloud forcing terms (the synoptic-scale heat, moisture and radiation budgets) were known the cloud-base mass flux was determined. This approach, common



to the above mentioned authors, is adapted in this work for the implicit model. The computer code used for the implicit model is an adaptation of the code that has been graciously provided by Johnson. The explicit model, however, although it follows the same basic framework as the implicit approach, employs available satellite data in a unique way to determine the forcing terms that the implicit model obtains from the synoptic-scale heat, moisture and radiation budgets.

Once the input data field has been prepared, the process of which is by no means trivial (and is discussed at length in Section 2.2), the determination of the cloud-base mass flux of a conservative tracer and its subsequent redistribution in the vertical can be divided into the following three parts and is illustrated in Figure 2.1-3:

- (1) The determination of the allowable cloud classes;
- (2) The specification of the cloud forcing terms; and
- (3) The parametric link between parts (1) and (2) such that the cloud-base mass flux for each cloud class can be determined.

The first objective is then, given that clouds do exist in a region, to determine the allowable cloud types, as deemed admissible by the vertical profile of environmental moist static energy ( $\tilde{h}$ ), which is defined by:

$$\tilde{h} \equiv c_p \tilde{T} + gz + L\tilde{q} \quad (1)$$

where  $c_p$  is the specific heat of constant pressure,  $g$  is the gravitational constant,  $z$  is the geopotential height,  $L$  is the latent heat

## MODEL SCHEMATIC

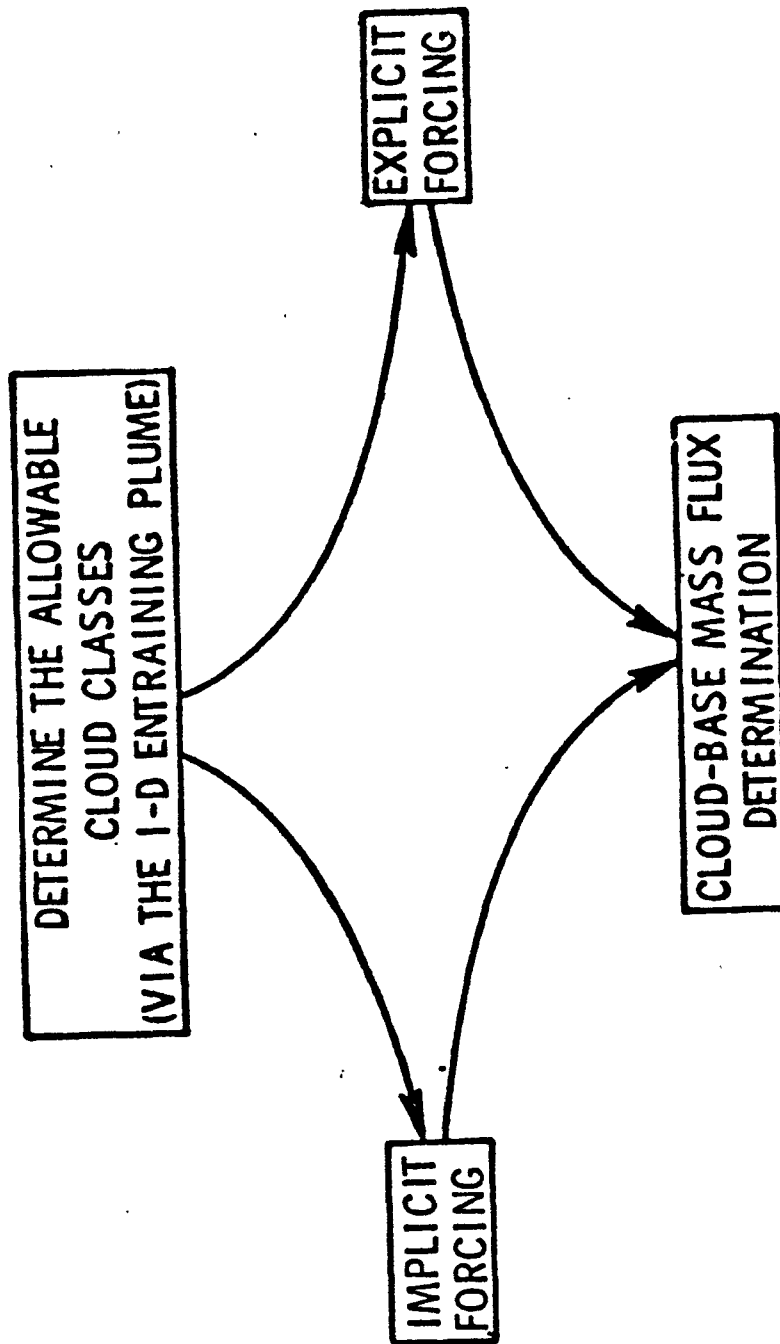


Figure 2.1-3. Box diagram showing the basic components of the modeling approaches used in this study

of condensation and  $\bar{\cdot}$  represents the environmental average over the grid cell at a specific height of the particular variable in question (in this case, temperature (T) and specific humidity (q)). At this point it is valuable to note the differences between the actual cloud field and the cloud field perceived by the model(s). Figure 2.1-4 shows a satellite picture taken at 2331Z on July 22, 1981 which encompasses the Summer Experiment area. The distribution of clouds and their respective updrafts in a hypothetical grid cell is illustrated in Figure 2.1-5. Owing to the random and subgrid scale nature of the cloud distribution, the models parameterize the clouds in terms of cloud updraft categories. Assuming that there is no overshoot of the updraft above its equilibrium level, the height of the updrafts can be given by the cloud-height distribution, as shown in Figure 2.1-6(a). The model further simplifies the picture by combining updraft elements of the same height while conserving the total updraft area. The transition from Figure 2.1-6(a) to 2.1-6(b) illustrates this point. The determination of the allowable height classes depicted in Figure 2.1-6(a), from the model's perspective, is accomplished by applying the principles of conservation of mass and energy to a steady-state entraining plume, making the assumptions that the updraft radius is constant with height and that neighboring updrafts do not interact with each other. Section 2.3 describes in detail the resulting relationship between the updraft mass flux, the initial or cloud-base mass flux, and the rate at which environmental air is entrained into the updraft. Such a relationship allows a direct determination of the desired updraft mass flux for each cloud class if the cloud class has an entrainment rate that is uniquely



Figure 2.1-4.

Satellite photograph of  
the Summer Experiment  
study area for 2331Z  
7/22/81.

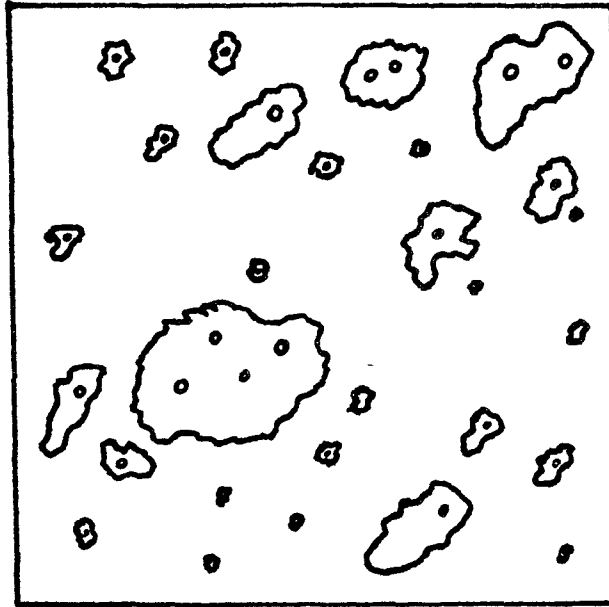


Figure 2.1-5. The distribution of clouds in a hypothetical grid cell is shown. The dot(s) or circle(s) represent hypothetical updrafts for the clouds shown.

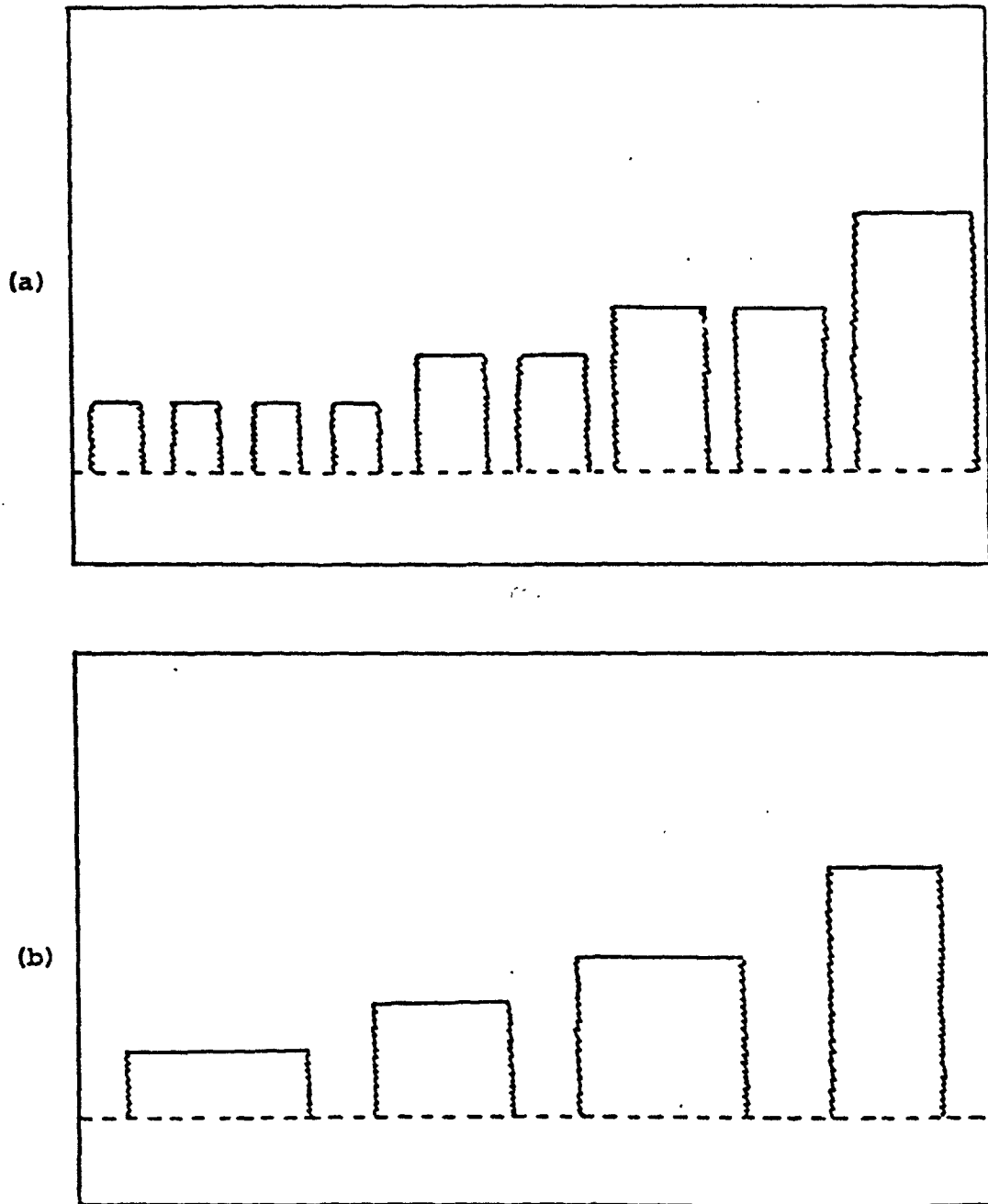


Figure 2.1-6. The model used in this study depicts a real cloud field by: (a) choosing a distribution of cloud updrafts to represent the ensemble of clouds present, and by (b) combining the updraft elements of the same height class (shown in part (a) of this figure) while conserving the total updraft area.

ascribed to it. As described in Section 2.3, the process of determining the cloud-height categories explicitly assigns a unique entrainment rate to each cloud class. Figure 2.1-7 illustrates that the entrainment rates, denoted by  $\lambda_1$ , ascribed to the cloud classes should show a negative correlation with cloud depth. This is reasonable since a cloud that has attained a greater height has entrained drier environmental air at a slower rate and hence has retained its buoyancy. However, since the profiles of  $T$  and  $q$ , and hence  $h$ , are interpolated from rawinsonde observation sites that may be on the order of 200 km away, it is not expected that the resulting profiles will reflect the influence that the cumulus field has had on the environment. Situations should therefore be expected to occur in which the calculated values of  $\lambda_1$  will increase with cloud-top height for a short distance instead of decreasing as would normally be expected. If in these cases, the satellite data indicate that clouds do exist in the grid cell of interest, it is assumed that a situation of conditional stability, indicated by  $d\tilde{h}^*/dp > 0$ , exists locally over the depth of the cloud field, where  $\tilde{h}^*$  is the saturated environmental moist static energy defined by,

$$\tilde{h}^* \equiv c_p \tilde{T} + gz + L\tilde{q}^* \quad (2)$$

and where  $\tilde{q}^*$  is the saturated environmental specific humidity. In these situations  $\lambda_1$  is assumed to decrease linearly with pressure so that  $\lambda_1$  decreases with increasing cloud top height throughout the cloud layer.

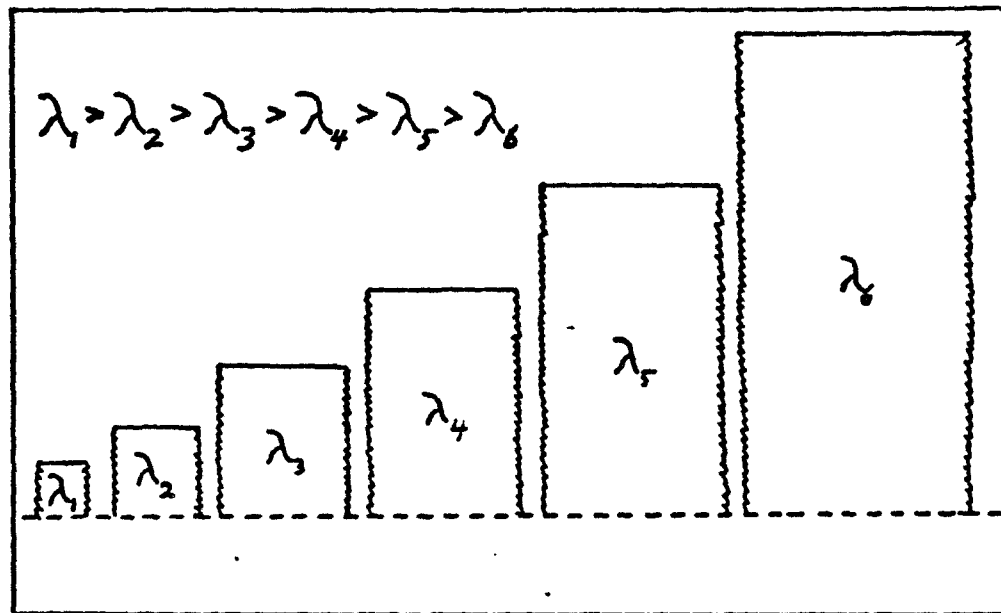


Figure 2.1-7. Model derived entrainment rates are assigned on the basis of cloud-top height, implying that taller clouds have entrained less and therefore have retained more of their buoyancy than shorter clouds have.



An interesting feature in the approach of assigning a unique entrainment rate to each cloud class, which is based on cloud-top height, and assuming that clouds detrain only at their cloud tops, is that the pollutant concentrations at any level are, neglecting any local sources or sinks, the result of the convective venting of a particular cloud class. A distinct layering of pollutants would therefore be expected. Such an occurrence is evident in Figure 2.1-8. This figure shows a time-height cross section of aerosol concentrations as measured by NASA's UV-DIAL system which has been tuned to measure atmospheric aerosols (Browell et al., 1983). The three segments shown in the figure represent results taken along different portions of the chosen flight path. The latitude and longitude, time, and vertical coordinate (in meters) are respectively indicated along the bottom, top, and side of each segment. Higher aerosol concentrations are indicated by the darker areas. The stratification of the aerosol layers is most evident in the top segment. At the time of 920 we see a mixed layer with moderate aerosol content extending up to ~500 m. Lower aerosol concentrations are present in the layer extending from 500 - 1000 m. The data indicate that significantly higher aerosol concentrations are found between 1000 and 1800 m, above which the values decrease only slightly. The origin of these aerosols is unclear, but the venting of aerosols from the mixed layer by convective clouds and their subsequent stratification is a possible explanation.

The second part of determining the cloud-base mass flux distribution is the quantification of the cloud forcing functions. In the formulation of Johnson (1975) and others who have used this framework

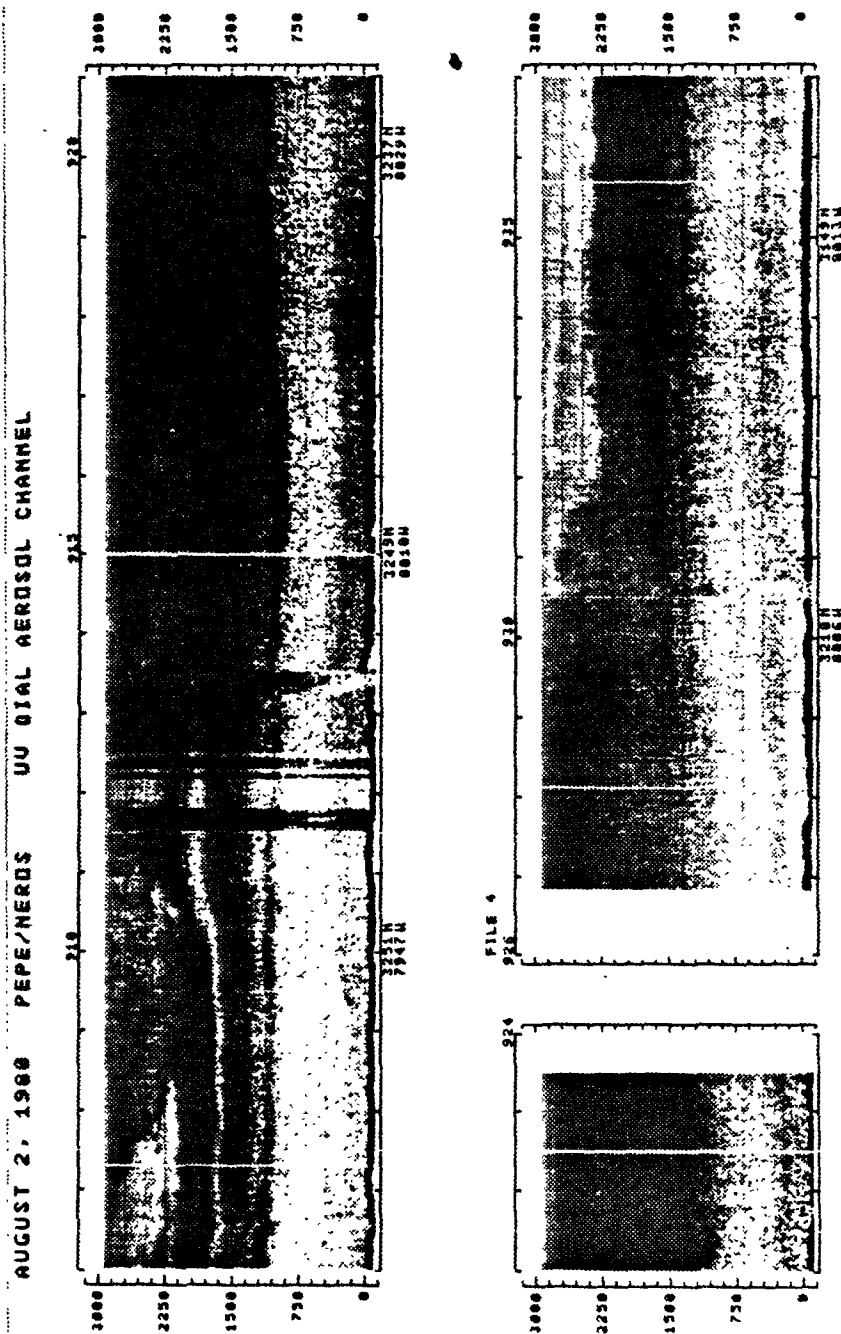


Figure 2.1-8. UV-DIAL depiction of pollutant stratification in the cloud layer.

the forcing functions are determined solely by the synoptic-scale heat, moisture and radiation budgets. In most of the applications of this approach, the influence of subsynoptic-scale phenomena on the resulting calculations was not a matter of critical importance since the main problem being addressed was the interaction between the convective and synoptic scales. In these cases the regions of interest were mainly over tropical ocean areas where topographical and diurnal perturbations could be considered to be minimal (Yanai et al., 1973; Ogura and Cho, 1973; Nitta, 1975). The cloud forcing functions used for these studies were obtained from rawinsonde data (with an average spacing of 400-500 km) that had been filtered in space and time to remove small-scale variations in the data. Johnson (1976) applied his model to both a semi-tropical and a tropical region. The rawinsonde data for the latter case were obtained from Reed and Recker (1971), who determined the average structure of a tropical wave resulting from a 'composite' of eighteen tropical disturbances. Lewis (1975), however, applied the model of Ogura and Cho (1973) to a mid-latitude continental region, wherein the average rawinsonde spacing was ~85 km, thereby incorporating many subsynoptic-scale features into the input data. In an operational mode for mid-latitude situations, the resolution of the standard rawinsonde observations is much less. As a result, the phenomena associated with meso-scale cyclogenesis, land-sea breeze convergence zones, local radiative inhomogeneities, and topographical influences are difficult, if not impossible to resolve from the observations made twice daily from the standard rawinsonde observational network. This issue will be addressed again in Section 2.2 in relation to

the minimum resolvable wave feature allowed by the rawinsonde network. Therefore, by determining the cloud forcing functions from rawinsonde data alone, as described in Section 2.4, clouds formed by other mechanisms, such as those mentioned above, will be unaccounted for. It is therefore conceivable that even though clouds are observed in a region or grid cell, the synoptic-scale data may have inadequate resolution for the determination of the forcing functions. Conversely, subsynoptic-scale phenomena may be suppressing cloud activity that the synoptic-scale rawinsonde data indicate should exist. In such a situation, a model based on rawinsonde data without the additional information provided by satellite data would fail.

A formalism for determining the cloud forcing functions from satellite data is presented in Section 2.5. In principle, this method would then bridge the spectral gap by allowing the satellite observed cloud field, which is the result of numerous forcing mechanisms on all scales, to determine the forcing of the cloud field. This has a distinct advantage over the previous method in that the actual forcing mechanisms do not need to be identified and therefore, the determination of their individual corresponding parametric forms can be avoided. Another problem that is avoided is that of the sensitivity of the synoptic-scale heat and moisture budgets to  $\partial \tilde{\omega} / \partial p$  since, as shown in Section 2.4, it is multiplied by the environmental static energy, which is generally a large number. However, this approach has the limitation that the computations are sensitive to a few parameters that may be difficult to obtain in an operational sense. These problems will be discussed further in Chapter 4.

The approach described in Section 2.5 to determine the convective forcing functions in light of the digital visible and infrared satellite imagery is centered around earlier works by Kuo (1965, 1974). In his work he determined the area of a cumulus cloud by proposing a relationship between the half-life of the cloud, the moisture required to form the cloud, and the net moisture convergence supplied by the large-scale flow and ground evaporation. Here, we invert this process and solve for the effective net moisture convergence using a vertical distribution of cumulus cover determined from satellite data. This quantity is labeled the 'bulk' forcing term in Section 2.5 and replaces the standard forcing terms that have been previously mentioned. It is termed a 'bulk' forcing term since the individual forcing terms are unknown. This method utilizes several critical assumptions which are outlined in Section 2.5.

The third and final step in determining the cloud-base mass flux of a conservative tracer is presented in Section 2.6 wherein the theoretical formulation that connects the steady-state entraining plume model, utilized in the first step, with the forcing terms, determined by either Section 2.4 or 2.5, is given. Briefly stated, Section 2.6 determines a parametric form of the vertical flux divergence of moist static energy, which is shown in Section 2.4 to be related to the cloud forcing terms. This parameterization is done in terms of the updraft mass flux and results in an integral equation that is solved for the cloud-base mass flux distribution, given the cloud forcing terms as a function of height. The solution of this integral equation is illustrated in Figure 2.1-9. The figure shows that if one starts the solution from the top of the cloud field, meaning

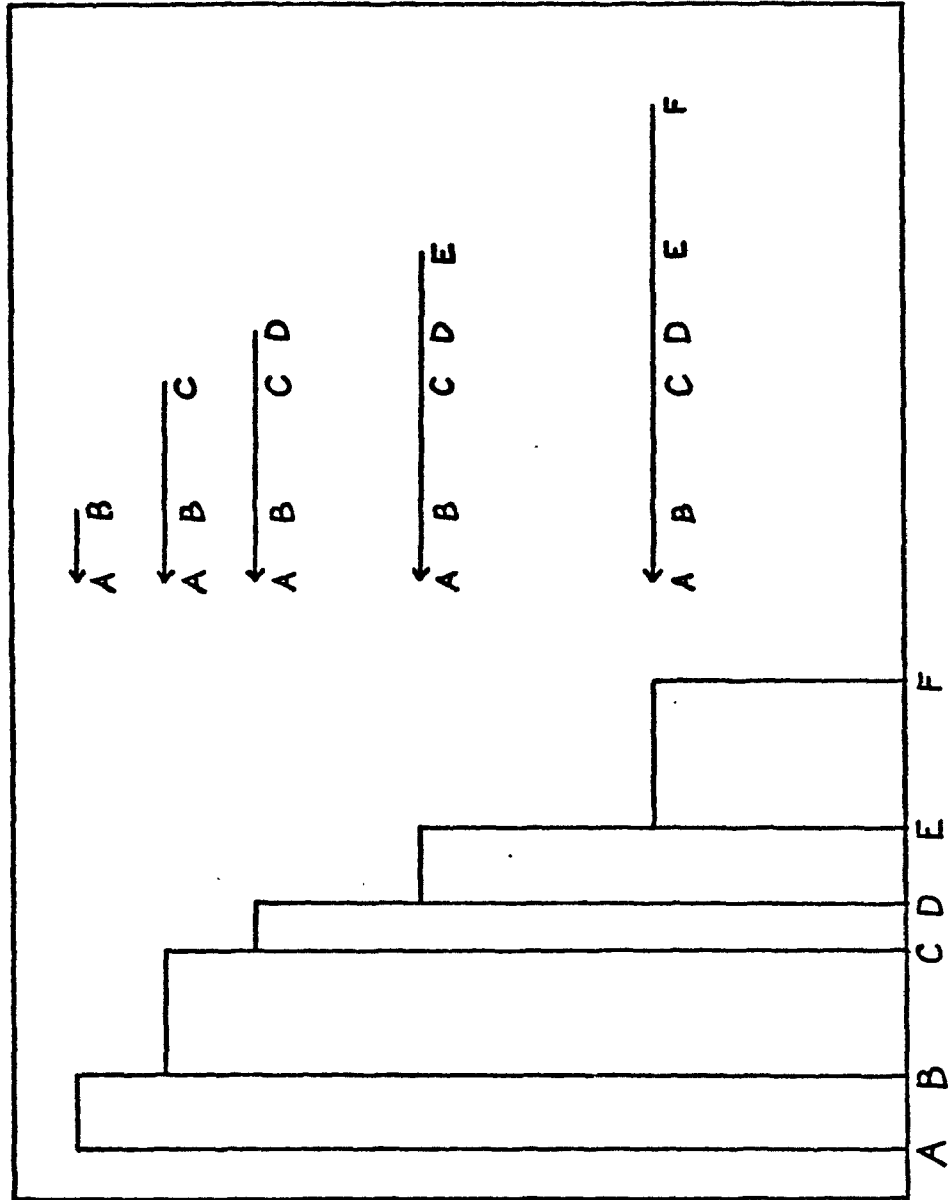


Figure 2.1-9. A schematic solution of the integral equation used to determine the cloud-base mass flux is presented. On the left side is a model cloud field (analogous to that in Figure 2.1-6(b)). On the right side is the vertical profile of the forcing terms.

that the cloud-base mass flux for the tallest cloud category is determined first, the amount of forcing supplied at the maximum cloud-top level is totally assigned to the tallest cloud class. The updraft mass flux for this cloud class is then determined such that the forcing present at the cloud top is satisfied. Once this is accomplished, the updraft mass flux at any level within this cloud class can be determined via the 1-D entraining plume model. The process is then repeated for the second highest cloud class. Now, the forcing supplied at the cloud top level for this cloud class must be partitioned between it and the cloud class just considered. Since it has already been determined how much 'forcing' was required for the previous cloud class, the remainder is left to force the present cloud class. This process is continued until the cloud-base mass flux for the shortest cloud class is determined, thus giving the spectral distribution of cloud-base mass flux according to cloud class.

As a result of either the implicit or explicit formulation, the cloud distribution depicted in Figure 2.1-6(b) is solved for such that the cloud forcing functions are satisfied at all levels in the model atmosphere. The resulting cloud-base mass flux for each cloud class is defined as:

$$m_B(\lambda) = -\sigma(\lambda)\omega_B(\lambda) \quad (3)$$

where  $\lambda$  is the entrainment rate that is uniquely ascribed to each cloud class,  $\sigma$  is the fractional updraft area and  $\omega_B$  is the updraft vertical velocity at the cloud base for the  $\lambda_i^{\text{th}}$  cloud class. Note

that in solving for  $m_B(\lambda)$ , from Equation (3) we see that without additional information on  $\omega$  we are unable to determine the updraft area that the model has required to satisfy the cloud forcing functions. Therefore, only the product of  $\sigma$  and  $\omega$ , namely  $m_B$ , is determined as a function of cloud class. However, due to the unique nature of the satellite data set used in this study, it will be shown in Section 2.5 that this data can be cast into the form shown in Figure 2.1-6(b), which can then be used to determine  $\sigma(\lambda)$  and subsequently, with the aid of Equation (3),  $\omega_B(\lambda)$ .

Before leaving this section, one additional concept needs to be mentioned, namely that of conservation of mass within each grid cell, which can be expressed as:

$$\bar{M} \equiv -\bar{\omega} = M_u + M_d + \tilde{M} \quad (4)$$

where  $\bar{M}$  is the grid cell averaged net mass flux and is taken to be the negative of the observed vertical motion field (so that an upward mass flux is positive),  $M_u$  is the integral of the updraft mass flux over all cloud categories and  $\tilde{M}$  is the residual, between-cloud compensating mass flux. Since the application of this model will be limited to cases where the clouds are nonprecipitating, the value of  $M_d$ , the convective scale downdraft mass flux, is set equal to zero. The units in Equation (4) have those appropriate for mass flux when divided by the gravitational constant  $g$ , which is omitted for clarity.

Results of the model are discussed in Chapter 3 for a few isolated cells in the Summer Experiment region. A sensitivity analysis of the model is given in Chapter 4, wherein the most crucial parameters for



the model's operation are identified. When interpreting the results of this model, one must be aware of the approximations that have been made. For example, even though satellite data may have been used to bridge the spectral gap in the forcing functions, the grid averaged profile of moist static energy is still derived from rawinsonde data. In addition, the entraining plume theory that is employed in this effort may not be strictly applicable to small clouds. In view of these assumptions, a formalism for obtaining reasonable estimates for the cloud-base mass flux and the subsequent vertical redistribution of a conservative tracer is obtained.

## 2.2 Data Preparation

The models described in Sections 2.3 through 2.6 require the specification of several different environmental parameters. The three major data bases required to determine these parameters are: (a) synoptic or large-scale meteorological data (determined from rawinsonde observations); (b) surface meteorological data and (c) statistics of the hourly observed cloud field determined from satellite data. The following three subsections will describe the methods used to prepare these data bases for use in the cloud venting models described in this report. Subsection (d) will list the remaining data fields that have been used as input.

### (a) Synoptic-scale analysis

The synoptic-scale analysis is based upon the twice-daily rawinsonde observations that encompass the study region in both space and time. These data were obtained on magnetic tape from the data

archives of the National Center for Atmospheric Research (NCAR).

Figure 2.2-1 shows the study region in relation to the spatial distribution of the 29 rawinsonde observation sites used for this study.

The data field thus obtained, was truncated at 500 mb and spatially interpolated (the process of which will be explained later in this subsection) to the computational grid domain shown in Figure 2.2-2 with the vertical resolution of the data chosen to be 25 mb for temperature (T) and specific humidity (q) and 50 mb for the horizontal wind components (u and v). Since the average spacing between rawinsonde sites is  $\approx 400$  km, the minimum resolvable feature from this data set has a wavelength of  $\approx 800$  km. In order to adequately depict such features in the computational domain, the spacing of the grid points should therefore represent that of the rawinsonde network. However, since the first derivatives of the synoptic-scale variables will be required in several instances, a grid spacing of  $\approx 400$  km would not be adequate.

Figure 2.2-3 illustrates this problem showing a typical streamline, which by definition, is everywhere parallel to the wind field. From this figure we see that unless the grid spacing is taken to be  $1/4$  of the minimum resolvable wavelength, the spatial derivatives of the scalar quantity represented by the wave would be inaccurate. Therefore, the computational grid was chosen to have a grid spacing of  $\approx 200$  km or  $2^\circ$  in latitude and  $2.5^\circ$  in longitude. As shown in Figure 2.2-2, this grid extends from  $34^\circ\text{N}$  latitude to  $41^\circ\text{N}$  latitude and from  $71^\circ\text{W}$  longitude to  $86^\circ\text{W}$  longitude. Since the ensuing computations are sensitive to not only the scalar field values, but also to their first derivatives, it is appropriate to use an interpolation

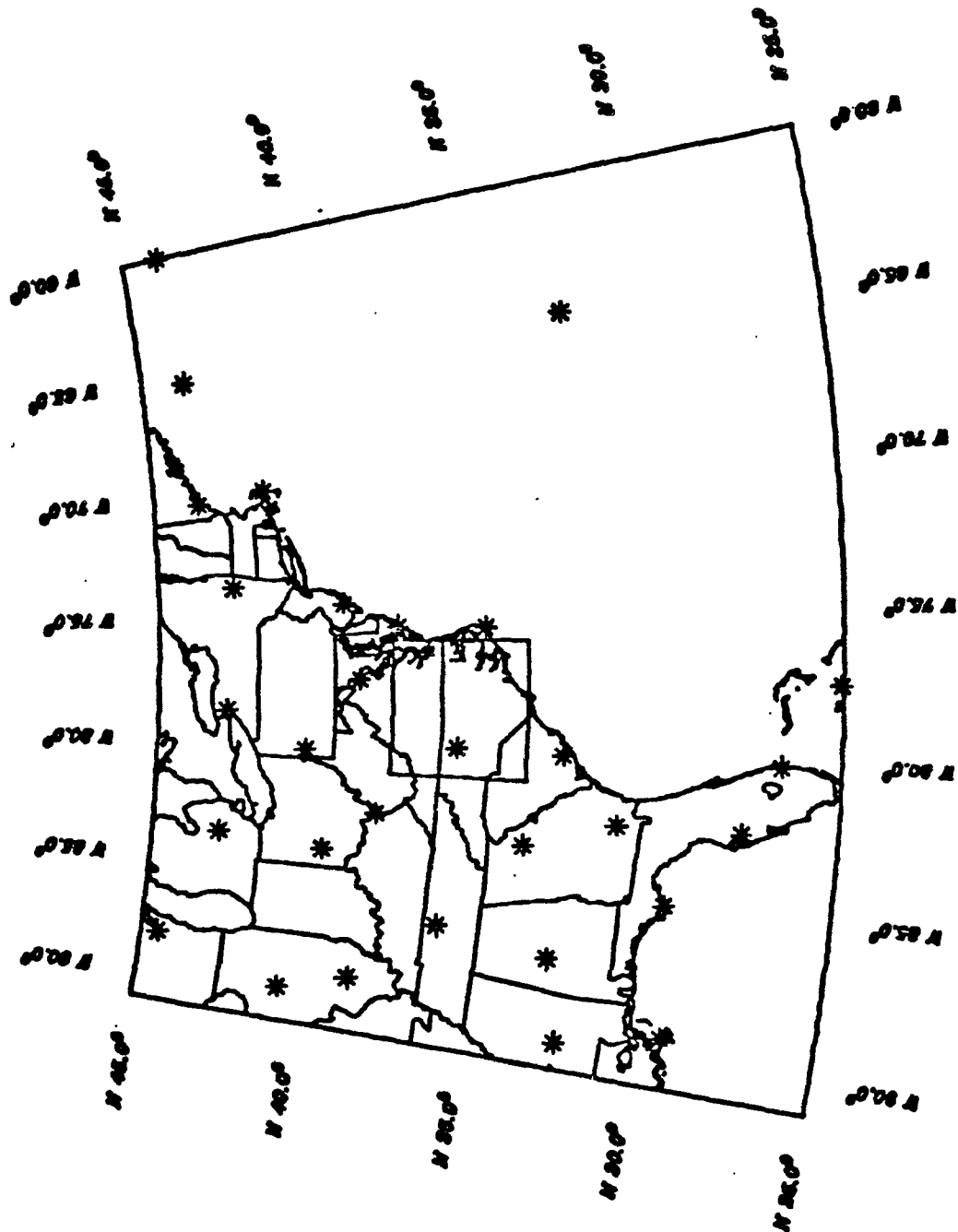


Figure 2.2-1. The spatial distribution of the rawinsonde observation sites used in the analysis of the Summer Experiment observational program, July 1981 is shown above. The enclosed region represents the study area.

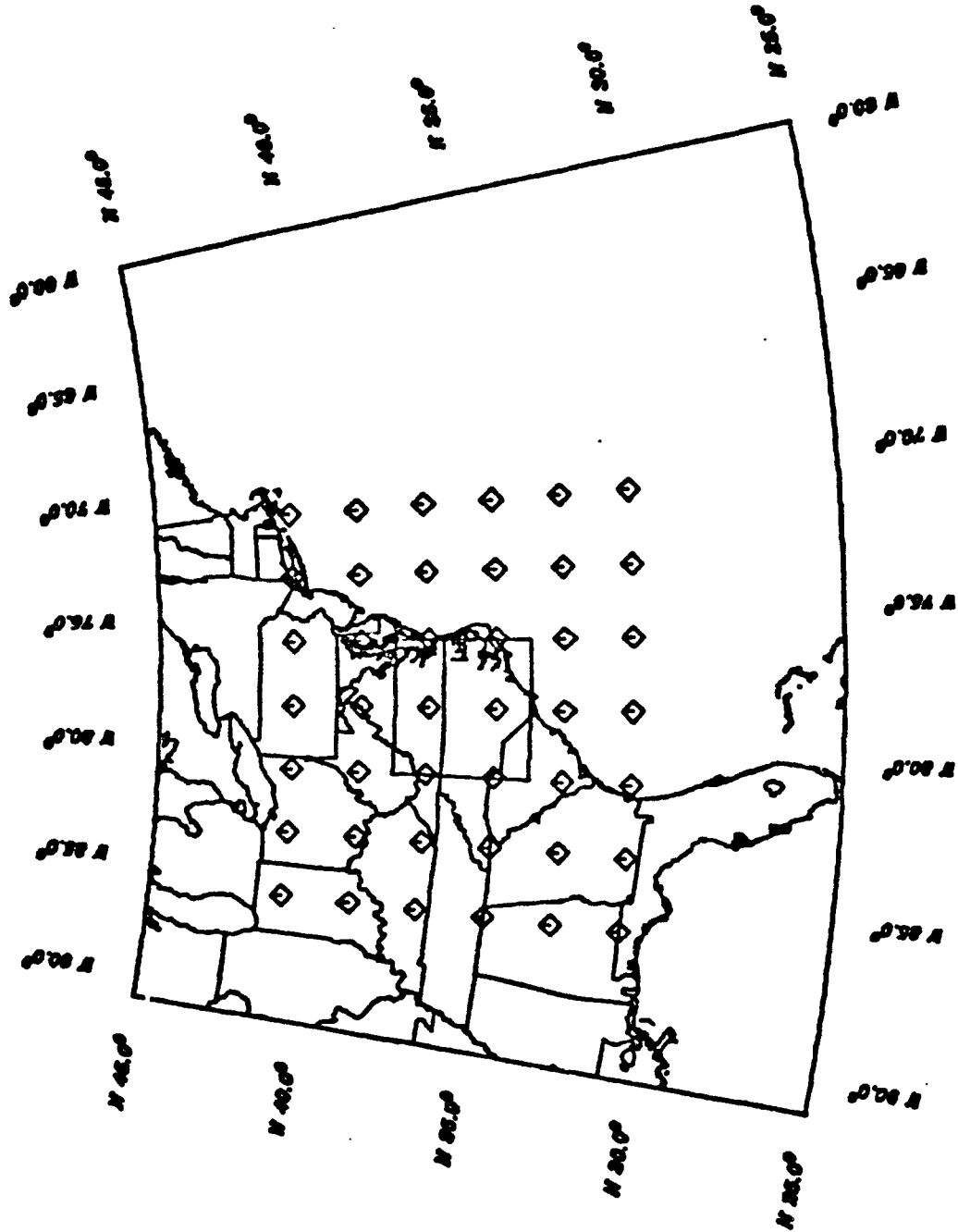


Figure 2.2-2. The computational grid domain used for the synoptic-scale analysis of the rawinsonde data is shown above. The enclosed region represents the study area.

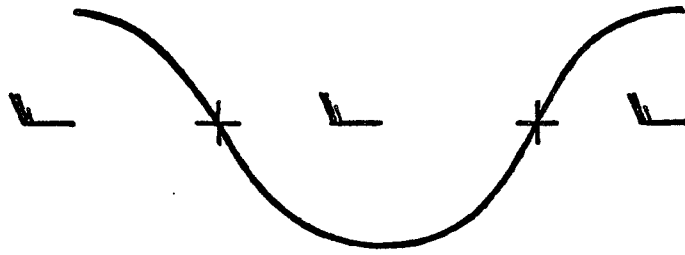


Figure 2.2-3. A schematic depiction of how the first derivative of a feature with a wavelength  $\lambda$  could be misrepresented by not having grid points located  $1/4 \lambda$  apart. A '+' indicates where additional grid points should be located.

method that will filter out small scale variations. Such a method has been developed by Barnes (1964, 1973) and has been employed by Bullock (1983) for use in EPA's ROM. The present study will use an adaptation of Bullock's work to obtain the spatially interpolated scalar fields that are required.

In his work, Bullock compared the results obtained from using several different forms for the weighting function required in spatial interpolation schemes. Bullock noted that in cases such as the one under consideration for this study, where a significant portion of the computational domain is over the ocean (a data sparse region), a 'hybrid' approach was appropriate. In this approach, a tangent-plane approximation is first utilized to determine an initial grid of the scalar field under consideration by extending the gradients of the data field beyond the coastline. This is accomplished by obtaining a tangent plane for each random data point such that a least-squares approximation is satisfied for the nearest N data points. The initial grid point values are then determined from the nearest N random data points, whose tangent planes are extrapolated to the grid point in question by employing the weighting function given by:

$$WT = (1 - (D_i/D_{\max})^2)/D_i \quad (5)$$

where  $D_i$  is the distance from the grid point to the  $i^{\text{th}}$  random data point and  $D_{\max}$  is the distance to the furthest random point used.

The result of the first phase of the 'hybrid' approach is the generation of a uniform distribution of initial data points. This is a requirement for the proper operation of the second part of the

'hybrid' approach which utilizes a scale-dependent filtering technique developed by Barnes (1964, 1973) to obtain the final scalar field.

The weighting function derived by Barnes has the form:

$$WB = \exp(-D^2/4C) \quad (6)$$

where the value of C is dependent on the wavelengths of the features that are to be filtered out of the analysis. The value of C used in this study filters all waves < 800 km. Barnes also showed that the amplitude of all waves will be reduced somewhat by this gridding procedure, but that the amplitude can, for the most part be restored by applying a correction pass to the resulting data field. The technique involves applying the same weighting function (Equation (6)) to the residuals between the initial and resultant data fields, and then adding this result to the previously obtained grid point value.

It should be noted that due to the smoothing nature of the tangent-plane approximation, its application to a data field implicitly filters features of unknown wavelengths out of the system prior to the application of the scale-dependent filtering technique of Barnes. This can be seen by the lack of any scale dependent parameter in the weighting function given by Equation (5). For this reason, as noted by Bullock (1983), until an analytical relationship between the number of points used to determine the tangent-planes, the number of tangent-planes used to determine the grid point values and the resultant scale-filtering can be found, the value of N must be subjectively chosen for the particular situation of interest.

The 'hybrid' scheme employed by Bullock works well for objectively interpolating a scalar field. Figures 2.2-4, 2.2-5 and 2.2-6 show

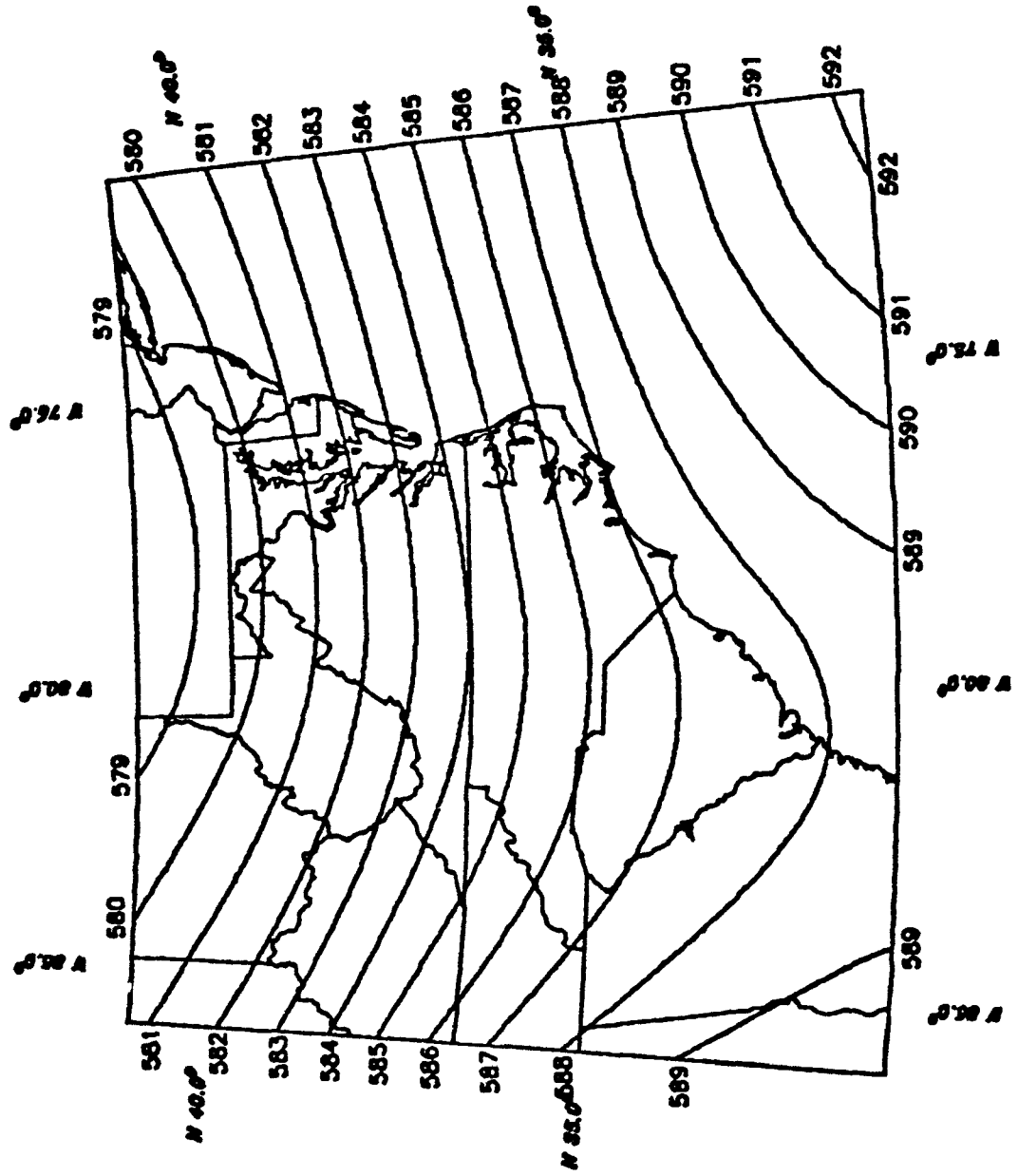


Figure 2.2-4. Objectively analyzed geopotential heights (gpm) for 00Z 7/23/81.



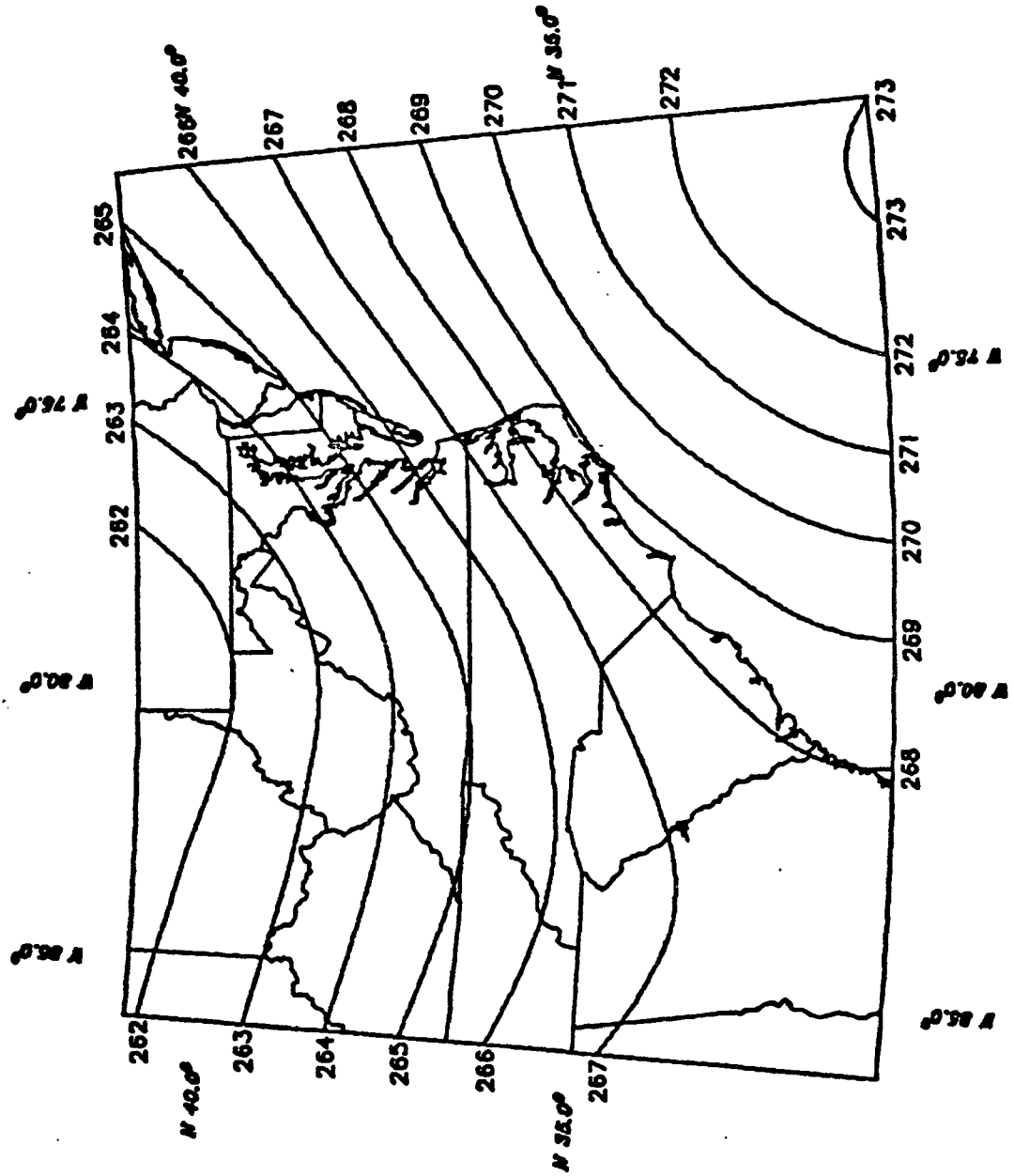


Figure 2.2-5. Objectively analyzed 500 mb temperature (K) for 00Z 7/23/81.

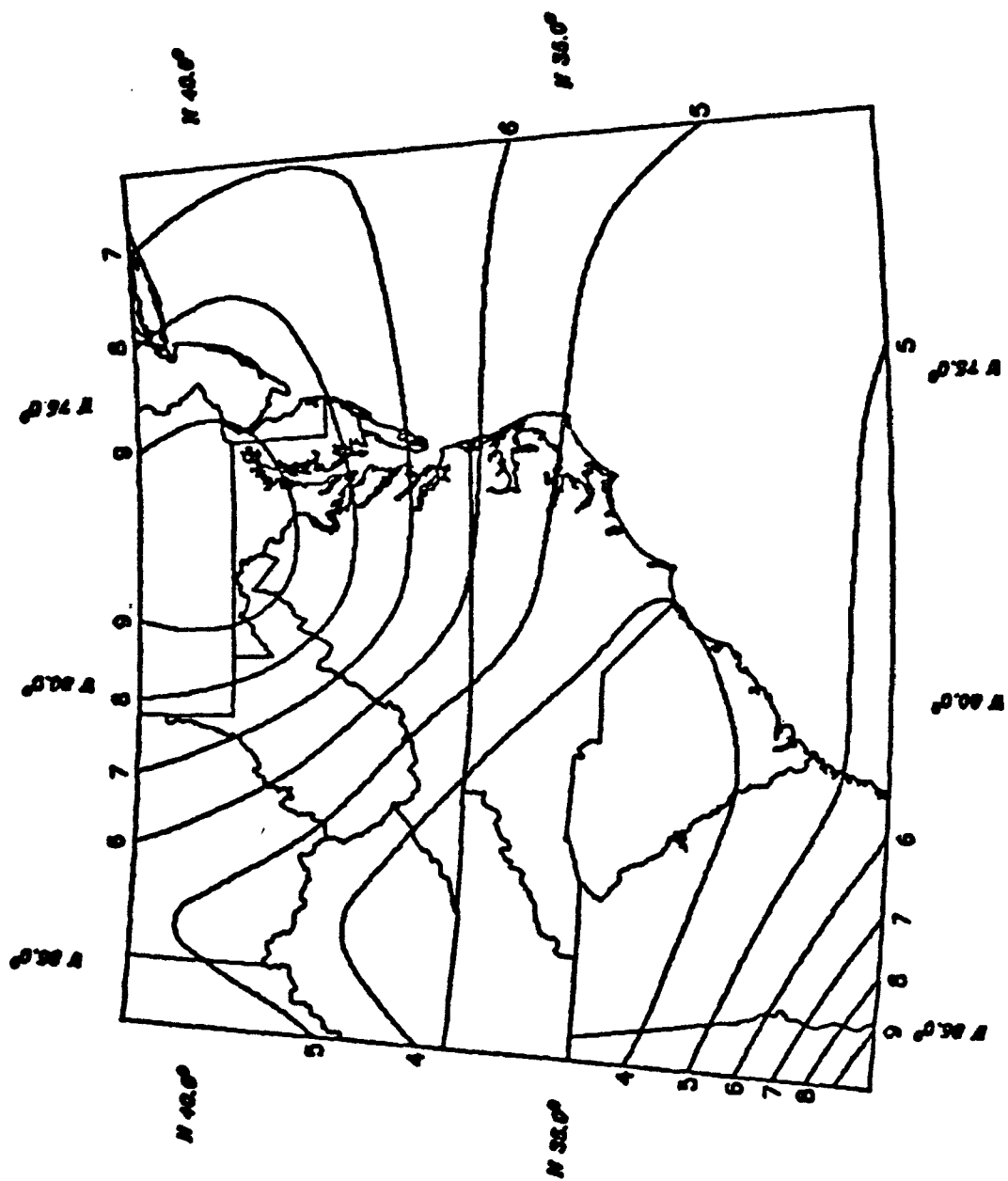


Figure 2.2-6. Objectively analyzed 500 mb specific humidity ( $\times 10$  g/kg) for 00Z 7/23/81.

the respective fields of geopotential height (gpm), temperature (K), and specific humidity (g/kg) at 500 mb for 00Z on July 23, 1981 using this approach. However, as pointed out by Schaefer and Doswell (1979) the horizontal interpolation of a vector quantity such as the observed wind field presents a problem. The following example, which is taken from their paper illustrates the situation. Consider the two wind observation sites shown in Figure 2.2-7 that lie on an east-west line.

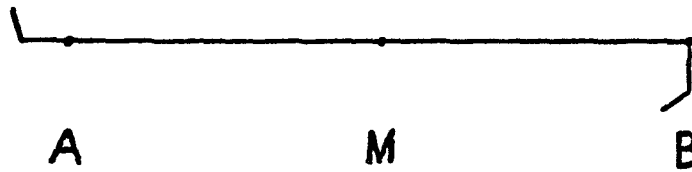


Figure 2.2-7 A schematic representation of a situation in which the interpolation of the horizontal components of the wind field do not yield the same results as the interpolation of the wind speed (see text for discussion).

The observation at point A shows that the wind is from the west at 10 m/s and that at point B is from the south at 10 m/s. Interpolating the wind speed and the wind direction separately to point M gives the value of 10 m/s from the southwest. However, when the individual  $u$  and  $v$  components are interpolated to the point M, the wind direction is still from the southwest, but the magnitude is now 7.07 m/s. Thus, an ambiguity exists in the interpolation of a vector field. The approach adopted by Bullock to solve this problem, which was subsequently utilized for this study, followed the method outlined by Schaefer and Doswell (1979). In their paper, they partitioned the

velocity field into irrotational and nondivergent parts according to the Helmholtz theorem:

$$\underline{V} = \nabla_h \chi + \underline{k} \times \nabla_h \psi \quad (7)$$

where  $\chi$  is the velocity potential (irrotational part),  $\psi$  is the stream-function (nondivergent part) and  $\nabla_h$  is the horizontal gradient operator. The fields of relative vorticity ( $\zeta$ ) and divergence ( $\delta$ ) are related to  $\psi$  and  $\chi$  in the following way:

$$\nabla_h^2 \chi = \delta \quad \text{and} \quad \nabla_h^2 \psi = \zeta \quad (8)$$

The velocity field can therefore be determined from Equation (7) by solving Equation (8) for a distribution of  $\chi$  and  $\psi$ , given a field of divergence ( $\delta$ ) and relative vorticity ( $\zeta$ ). However, in order for a solution to Equation (8) to be determined, boundary conditions must be specified. Instead of assuming a priori the relative role that the irrotational part ( $\chi$ ) or the nondivergent part ( $\psi$ ) will play in determining the boundary conditions, as several authors have done in the past, Schaefer and Doswell (1979) allowed the boundary conditions to be determined by an initial spatial interpolation of the u and v wind field components. The 'hybrid' method, which has been previously described, was used for this purpose. Briefly, the method of solution used by Schaefer and Doswell is a variational analysis technique in which the vorticity and divergence of the final wind field is constrained to match the given field of relative vorticity ( $\zeta$ ) and divergence ( $\delta$ ) while the difference between the initial wind field,

obtained from the component interpolation, and the final wind field is also minimized. The expression given by Schaefer and Doswell for the final wind field is then:

$$\underline{V} = \underline{V}_0 + (\nabla \lambda_2 + \underline{k} \times \nabla \lambda_1)/2 \quad (9)$$

where  $\underline{V}_0$  is the initial wind field and  $\lambda_{1,2}$  are the Lagrange multipliers given by:

$$\nabla^2 \lambda_1 = 2(\zeta - \underline{k} \cdot \nabla \times \underline{V}_0) \quad (10)$$

and

$$\nabla^2 \lambda_2 = 2(\delta - \nabla \cdot \underline{V}_0) \quad (11)$$

where  $\zeta$  and  $\delta$  are the given relative vorticity and divergence fields. These fields are determined, following Bullock (1983), by the methods developed by Bellamy (1949) and Endlich and Clark (1963), in which point values of relative vorticity and divergence are determined for the centroids of triangles formed by rawinsonde observation sites, assuming that the wind varies linearly over the triangular region. Figures 2.2-8(a), (b) and (c) show the synoptic-scale 500 mb relative vorticity field ( $\times 10^6 \text{ s}^{-1}$ ) for 00Z 7/23/81 obtained from: (a) the initial u and v component interpolation; (b) the interpolated centroid point values of  $\zeta$ ; and (c) from the final wind field determined from Equation (9). Figures 2.2-9(a), (b), and (c) show the corresponding synoptic-scale 500 mb divergence values ( $\times 10^6 \text{ s}^{-1}$ ). Figures 2.2-10(a) and (b) show the corresponding wind fields from

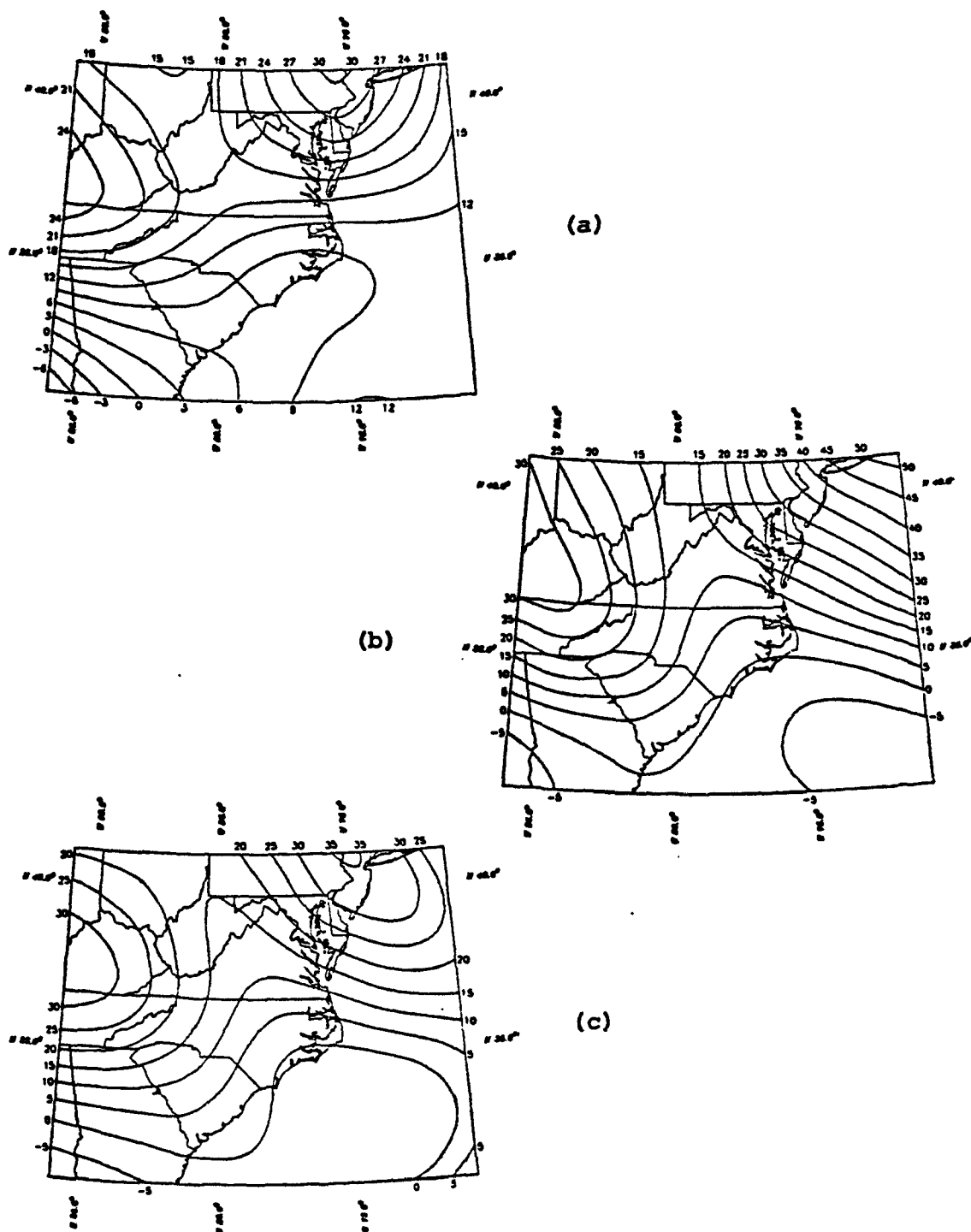


Figure 2.2-8. Synoptic-scale relative vorticity fields ( $\times 10^6 \text{ s}^{-1}$ ) at 500 mb for 00Z 7/23/81: (a) from initial  $u$  and  $v$  component interpolation, (b) from the interpolated centroid point values of  $\zeta$ , and (c) from the final wind field determined from Equation (9).

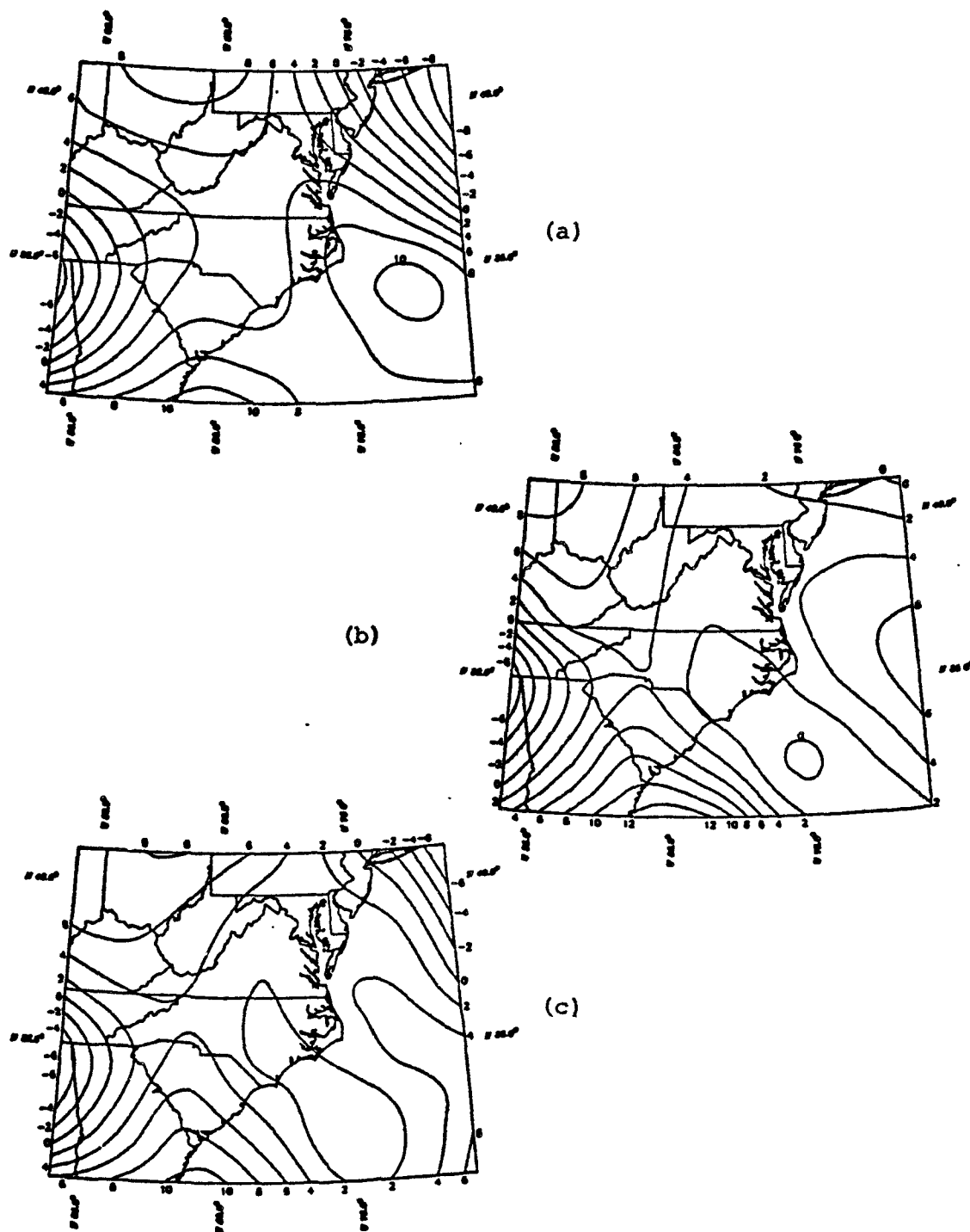


Figure 2.2-9. Synoptic-scale divergence fields ( $\times 10^6 \text{ s}^{-1}$ ) at 500 mb for 00Z 7/23/81: (a) from initial u and v component interpolation, (b) from the interpolated centroid point values of  $\delta$ , and (c) from the final wind field determined from Equation (9).

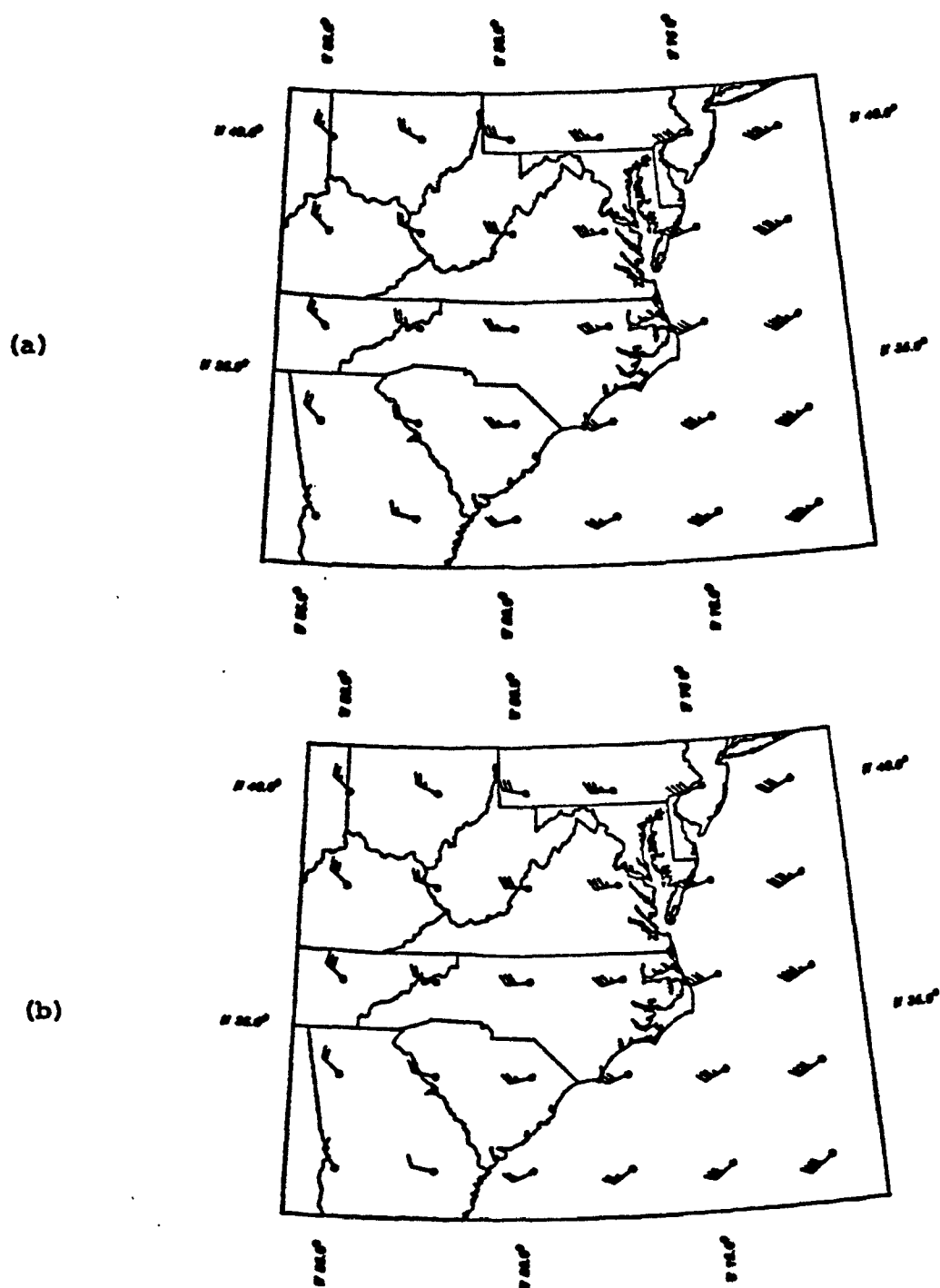


Figure 2.2-10. Wind field (kt) at 500 mb for 00Z 7/23/81:  
(a) from initial u and v component interpolation,  
(b) from the Schaefer-Doswell variational technique.



(a) the initial u and v component interpolation and (b) those resulting from the Schaefer-Doswell variational analysis scheme.

We note that although the wind field does not appear to have changed by much, the relative vorticity and divergence fields shown in Figures 2.2-8(a) and 2.2-9(a) have been altered to have more of the characteristics of the 'measured' relative vorticity and divergence fields shown in Figures 2.2-8(b) and 2.2-9(b).

The determination of the synoptic-scale horizontal wind field by the method described above will now enable a reliable determination of the synoptic-scale vertical velocity to be made. We integrate the continuity equation (expressed in pressure coordinates),

$$\nabla_h \cdot V + \frac{\partial \omega}{\partial p} = 0 \quad (12)$$

to obtain,

$$\omega(p) = \int_p^{p_s} (\nabla \cdot V)_{ave} dp \quad (13)$$

where  $(\nabla \cdot V)_{ave}$  is the layer averaged divergence and  $p_s$  is assumed to be 1000 mb, where it is assumed that  $\omega(p_s) = 0$ . An attempt to account for the influence that topography may have on the vertical motion field was met with several difficulties. Since topographical influences are subsynoptic-scale phenomena, this influence would have been filtered out of the analysis due to the scale-dependent filtering technique used in the spatial interpolation. In addition, we see from Equation (13) that since the computed vertical velocity field is determined solely from the layer averaged divergence field,

which, in turn is determined from the synoptic-scale relative vorticity and divergence fields, a relationship between the induced vertical velocity due to topography and the existing synoptic-scale vorticity and divergence fields in three dimensions is required. Such a relationship is, at best, unclear and therefore, the impact of topographical features on the vertical velocity field, as influenced by changes in the synoptic-scale relative vorticity and divergence fields, will be left as an area of future research. Figure 2.2-11 shows the computed vertical velocity field ( $\text{mb hr}^{-1}$ ) at 500 mb for 00Z 7/23/81. Comparing this figure with the satellite photograph for this same time, shown in Figure 2.1-3, we see a general agreement between areas of upward motion (negative in the pressure coordinate system) and cloudiness. It should be noted that although considerable effort was made to determine gridded field of various parameters over the ocean area, the reliability of these values becomes increasingly questionable with increasing distance from the coastline.

Thus, by using a scale-dependent filtering technique for the interpolation of a scalar field and a variational analysis approach for the spatial interpolation of the wind field, a reasonable depiction of the synoptic-scale fields required for the execution of the model can be obtained. Once these variables are determined for the computational grid shown in Figure 2.2-2, they are linearly interpolated in time over the twelve hours between rawinsonde observations, having the result of ignoring the diurnal variation of the meteorological field. This is a problem that needs to be addressed in future works, but for the purpose of this effort, will be ignored.

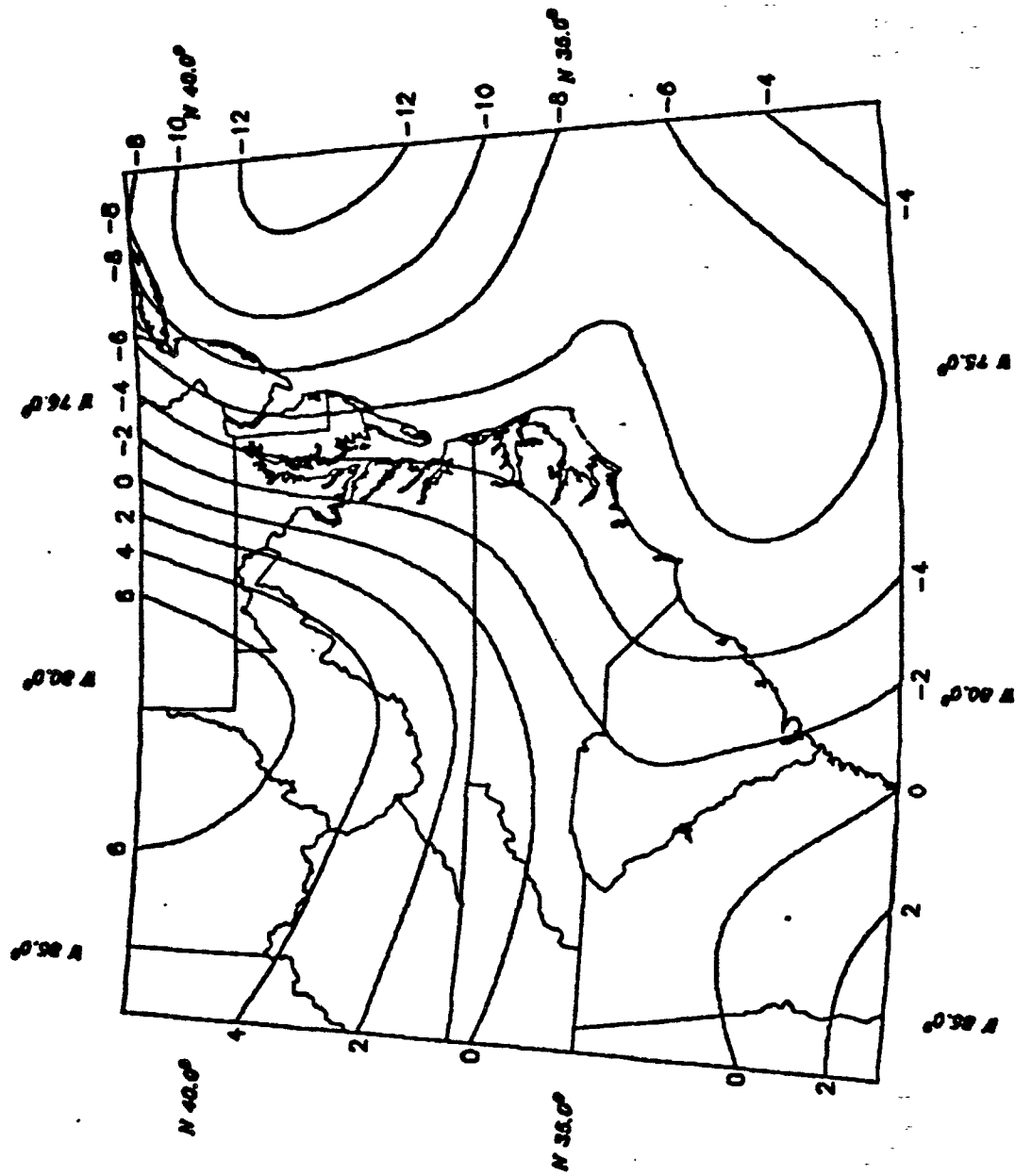


Figure 2.2-11. Vertical velocity field ( $\text{mb hr}^{-1}$ ) at 500 mb for 00Z 7/23/81.

Once the temporal interpolation is done, the values are subsequently interpolated to the center of the cells shown in Figure 2.1-2 using an overlapping polynomial technique following Bullock (1983).

Vertical profiles of temperature, specific humidity, and wind data are thus obtained for each grid cell. These profiles are then used to define 'the environment' for each cell for both the implicit and explicit approaches. The vertical distribution of cloud forcing functions required for the implicit approach used in this study is based on combining these profiles with the radiational cooling profile as described in Section 2.4.

(b) Surface analysis

As in the case of the rawinsonde data used for the synoptic-scale analysis, the surface meteorological data employed in this study were also obtained from NCAR. Figure 2.2-12 shows the spatial distribution of the surface observation sites used in this study. Since the density of the surface observational network does not exhibit a discontinuity similar to that found in the synoptic-scale case, the 'hybrid' approach was not necessary and a straight-forward application of Barnes' technique, described in the previous subsection, was used. Figure 2.2-13 shows the computational grid that the surface data was thus interpolated to. Since the first derivatives of the resulting scalar fields were not required, the grid spacing shown in Figure 2.2-13 approximated the average station spacing of 110 km or  $1.0^\circ$  latitude by  $1.25^\circ$  longitude. The scalar fields of temperature and dew-point temperature were then interpolated, using the method of overlapping polynomials, to the center of the grid cells shown in

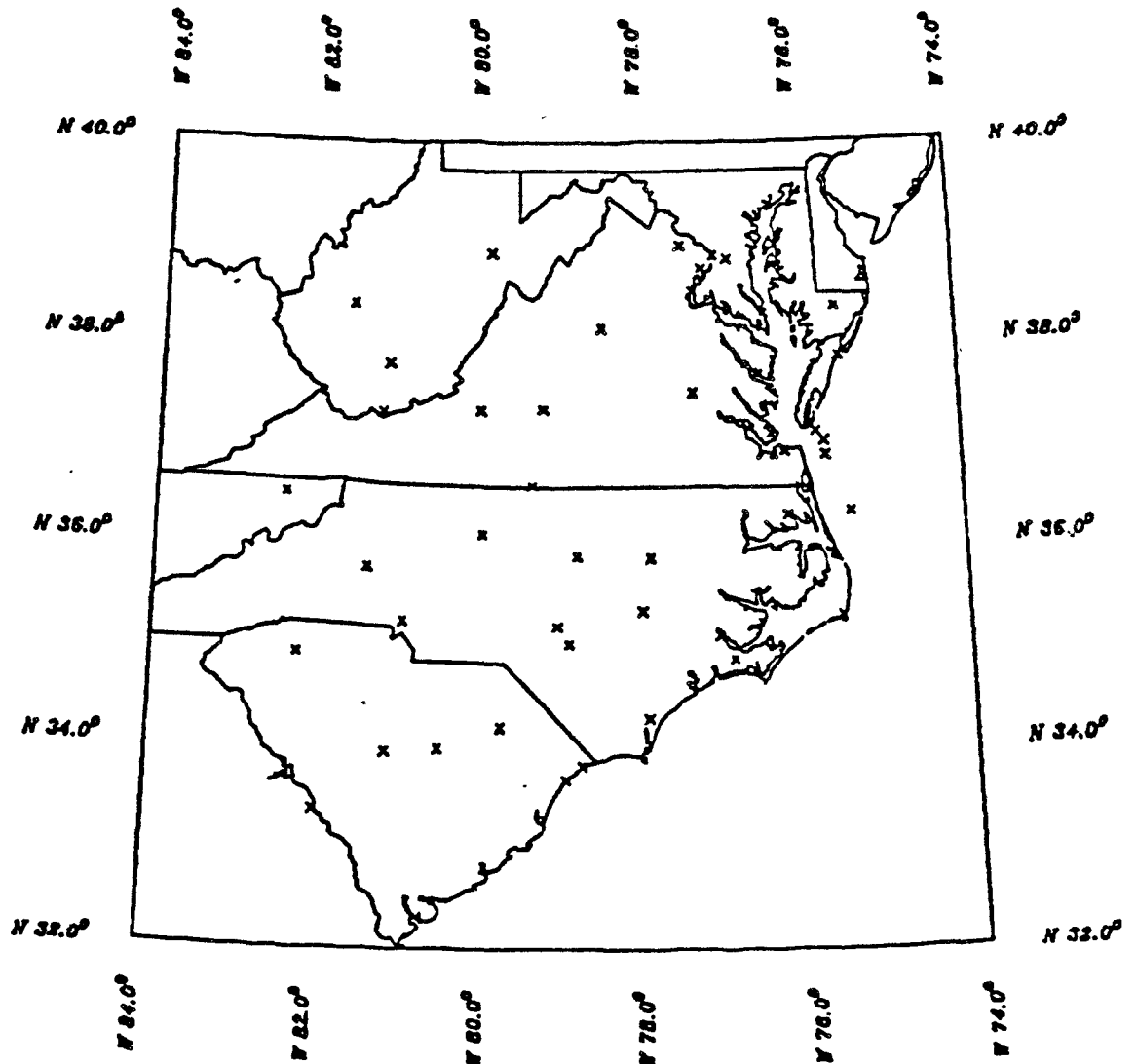


Figure 2.2-12. The spatial distribution of surface meteorological observation sites used in the analysis of the Summer Experiment observational program, July 1981.

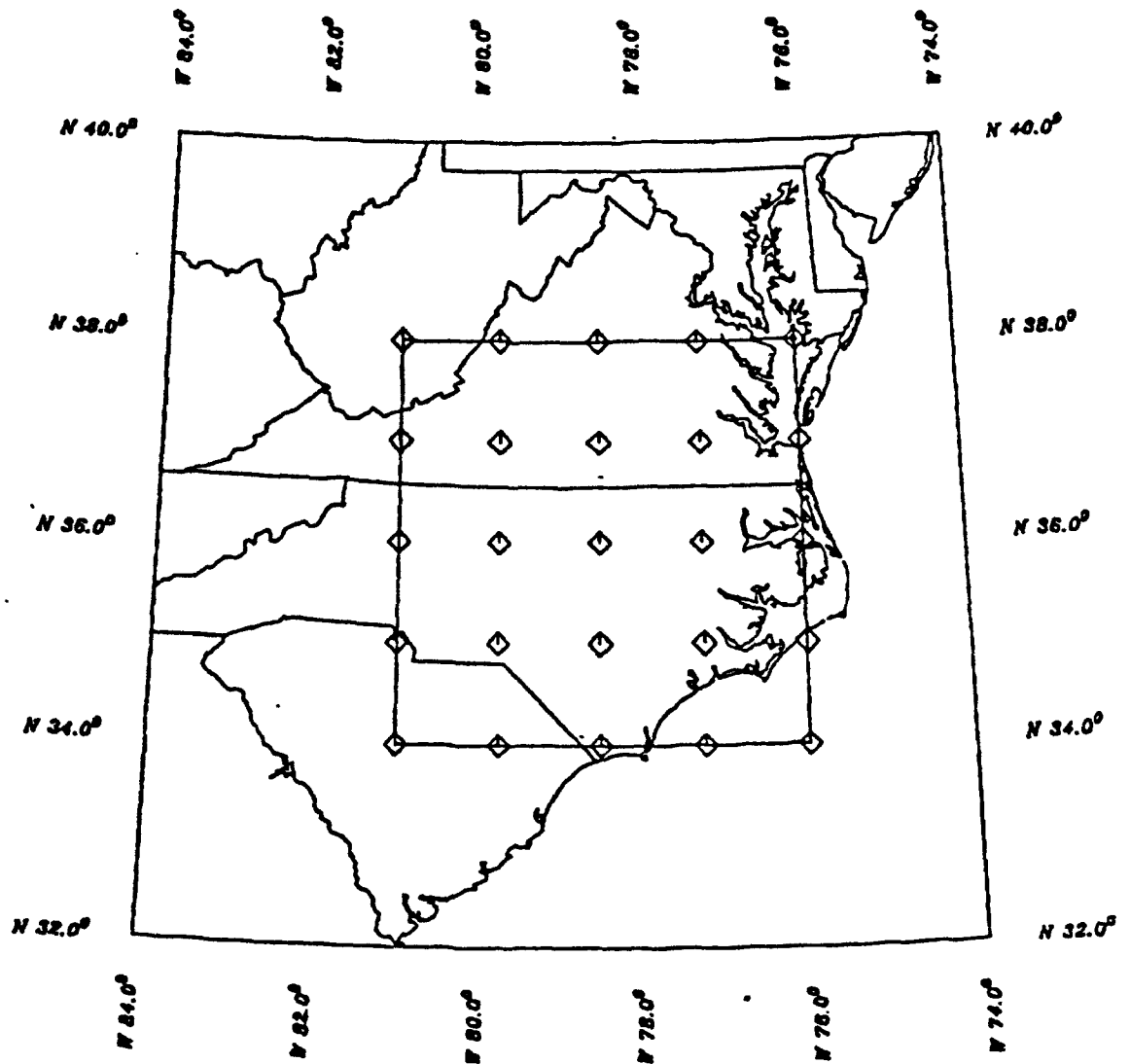


Figure 2.2-13. The computational grid domain used for the surface meteorological data is shown above. The enclosed region represents the study area.

Figure 2.1-2. The resulting temperature and dew-point temperature analyses for 00Z 7/23/81 are shown in Figures 2.2-14(a) and (b).

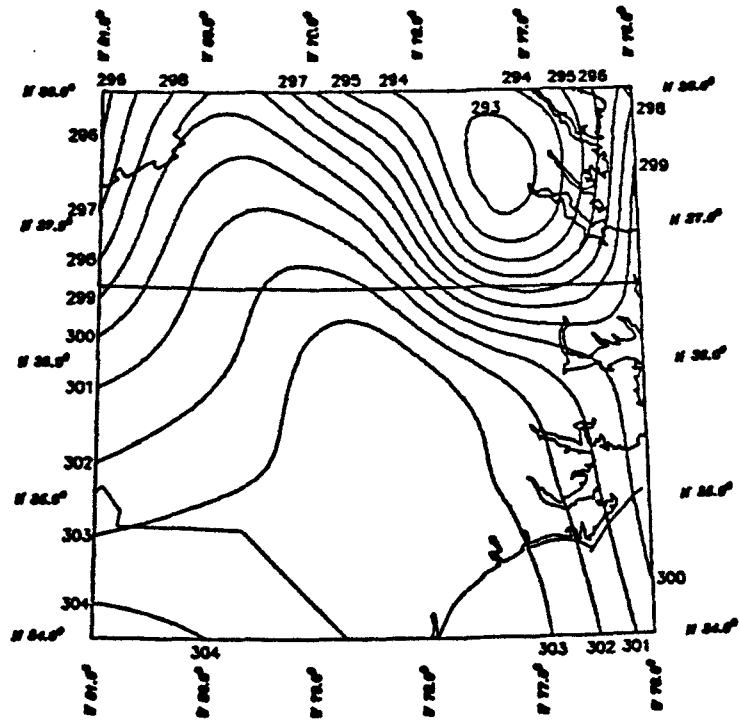
Since the data available from NCAR were archived at 3 hr intervals, an interpolation in time was required. This was done with a standard cubic spline routine.

(c) Satellite data

Cloud statistics for this study were provided by scientists at Colorado State University (CSU) working under a contract from the U.S. EPA. The digital satellite data used in this study were obtained from the Geostationary Operational Environmental Satellite (GOES) and were made available by the Environmental Data Information Service of the National Oceanic and Atmospheric Administration (NOAA/EDIS). This information was then processed through CSU's Interactive Research Imaging System (IRIS) to give the total cloud cover, cumulus cloud cover, average cumulus height and frequency distribution of cumulus heights for each grid cell in the region of interest (shown in Figure 2.1-2).

The IRIS method employed by the CSU scientists is bispectral in nature since it uses both visible and infrared (IR) information to determine the desired parameters (Reynolds and Vonder Haar, 1977). This is accomplished in basically three steps. First, a cloud classification is done by combining the visible and IR data into a color-coded display that is shown on a video monitor. A subjective determination is then made to distinguish between areas of cirrus and cumulus clouds. Finally, the determination of the cloud-top temperatures is made. The information from the IR channel (centered at  $11.5\ \mu\text{m}$ )

(a)



(b)

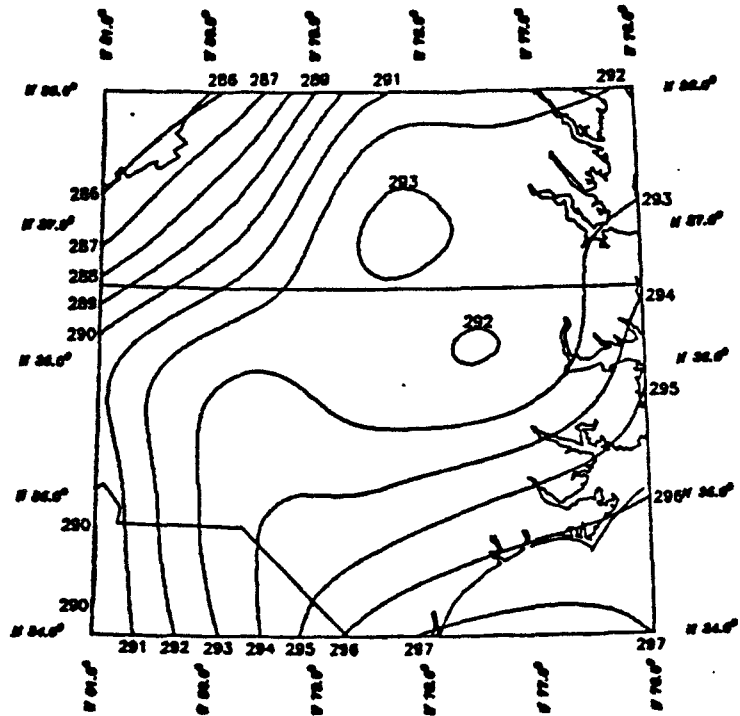


Figure 2.2-14. Surface observations of (a) temperature (K),  
(b) dew-point temperature (K) for 00Z  
7/23/81.



would, by itself, give only a coarse estimation of the cloud-top temperature. This is because many cumulus clouds are much smaller than the 4 x 8 km resolution of an IR picture element (pixel) and a straight-forward determination of the cloud-top temperature would therefore bias the result towards the apparent warmer values of the background surface temperatures. In order to avoid this problem the IRIS bases the cloud-top temperature calculation on the observed temperature (as sensed by the IR instrument), the background surface temperature (as determined from the minimum observed temperature in the region), and the fractional cloud cover (determined from the visible channel) in the following way (Behunek et al., 1983):

$$T_{CT} = (T_0 - (1 - A)T_B)/A \quad (14)$$

Where  $T_{CT}$  is the desired cloud-top temperature,  $T_0$  is the observed temperature,  $T_B$  is the background temperature and  $A$  is the fractional cloud cover determined from the visible channel (the resolution of which is approximately 2 km<sup>2</sup>). Cloud-top temperatures are determined in this way until 2000 EDT. After this time the data from the visible channel becomes hard to interpret leaving the IR channel as the only source of information. The final step in the process is that of transforming the determined cloud-top temperatures into cloud-top heights. This was done by obtaining rawinsonde information for stations within and surrounding the area of interest and interpolating in space and time to each cell of the region. Employing the resulting temperature profile, the distribution of cloud-top temperatures were translated into cloud-top heights.

There are several factors which can introduce error into the above analysis. The mere determination of the existence of clouds is subject to the horizontal resolution of the visible imagery, implying that clouds on the scale of cumulus humilis or thin cirrus clouds would not be detected. The determination of the cloud-top height would be affected by atmospheric water-vapor emission, response time of the IR instrument, interference by multilayered clouds and errors in the rawinsonde data. The determination of the cloud location is influenced by the viewing angle since the sub-satellite point is at  $75^{\circ}\text{W}$ ,  $0^{\circ}\text{N}$ .

The effect of water-vapor emittance  $DT_{\text{WV}}$  was considered to be small since most of the water vapor resides in the subcloud layer. Additionally, since the background temperature used in determining the cloud-top temperature was satellite derived, it implicitly includes the water-vapor emission as opposed to using surface-based temperature observations. The response time of the IR instrument can induce an error of 1 to  $5^{\circ}\text{C}$ ,  $DT_{\text{RES}}$ , depending on the actual cloud-top and background temperatures and the configuration of the cloud field. Due to the large size of the IR pixel an obscuring cloud field may, at times, be present. This situation has the potential for introducing large errors into the calculation of  $T_{\text{CT}}$ . It was therefore decided that  $T_{\text{CT}}$  would not be determined for any pixel in which cumulus clouds comprised less than 70% of the total cloud field. The differential thermal radiative heat loss between that of the cloud and its immediate environment,  $DT_{\text{EQ}}$ , was assumed to be small (Pitts et al., 1975), which enabled  $T_{\text{CT}}$  to be adequately represented by the environmental temperature at the same height. Other significant errors may include

$DT_{HR}$ , representing the error in the horizontal interpolation of the RAOB data, and  $DT_{VI}$ , the error in the vertical interpolation of  $C_{CT}$ .

The CSU scientists gave the following values to the above mentioned errors (Behunek et al., 1983):

$DT_{EQ}$	-0.5°C
$DT_{WV}$	-0.5°C
$DT_{RES}$	+2.0°C
$DT_{HR}$	+1.0°C
$DT_{VI}$	+1.0°C

The maximum error in determining  $T_{CT}$  would therefore be +3.0°C, which, using a lapse rate of 6.5°C/km yields an error of 462 m or 1514 ft.

It is the frequency distribution of cumulus cloud-top heights that makes this data set unique. These data, as received from CSU, are given in terms of IR pixels for each 500 ft layer from 500 to 20,000 ft for each grid cell shown in Figure 2.1-2. This information is then transformed into a cloud-cover distribution as a function of height. It is done in the following manner and is illustrated in Figures 2.2-15(a), (b) and (c). The satellite data are received in the form shown in Figure 2.2-15(a). It is first assumed that, starting with the maximum cumulus cloud top, which is represented by the highest non-zero 500 ft layer, each succeeding non-zero layer below this point represents an increase in the cumulus cloud cover. The total number of IR pixels observed for each grid cell shown in Figure 2.1-2 is then determined by integrating the pixel count over all of the 500 ft vertical layers for each cell. A regression analysis is then applied to the data pair of the total pixel count for each grid cell and the corresponding fractional cumulus cloud cover observed in the visible wavelength region. This analysis was done for all of the grid cells for which satellite data were

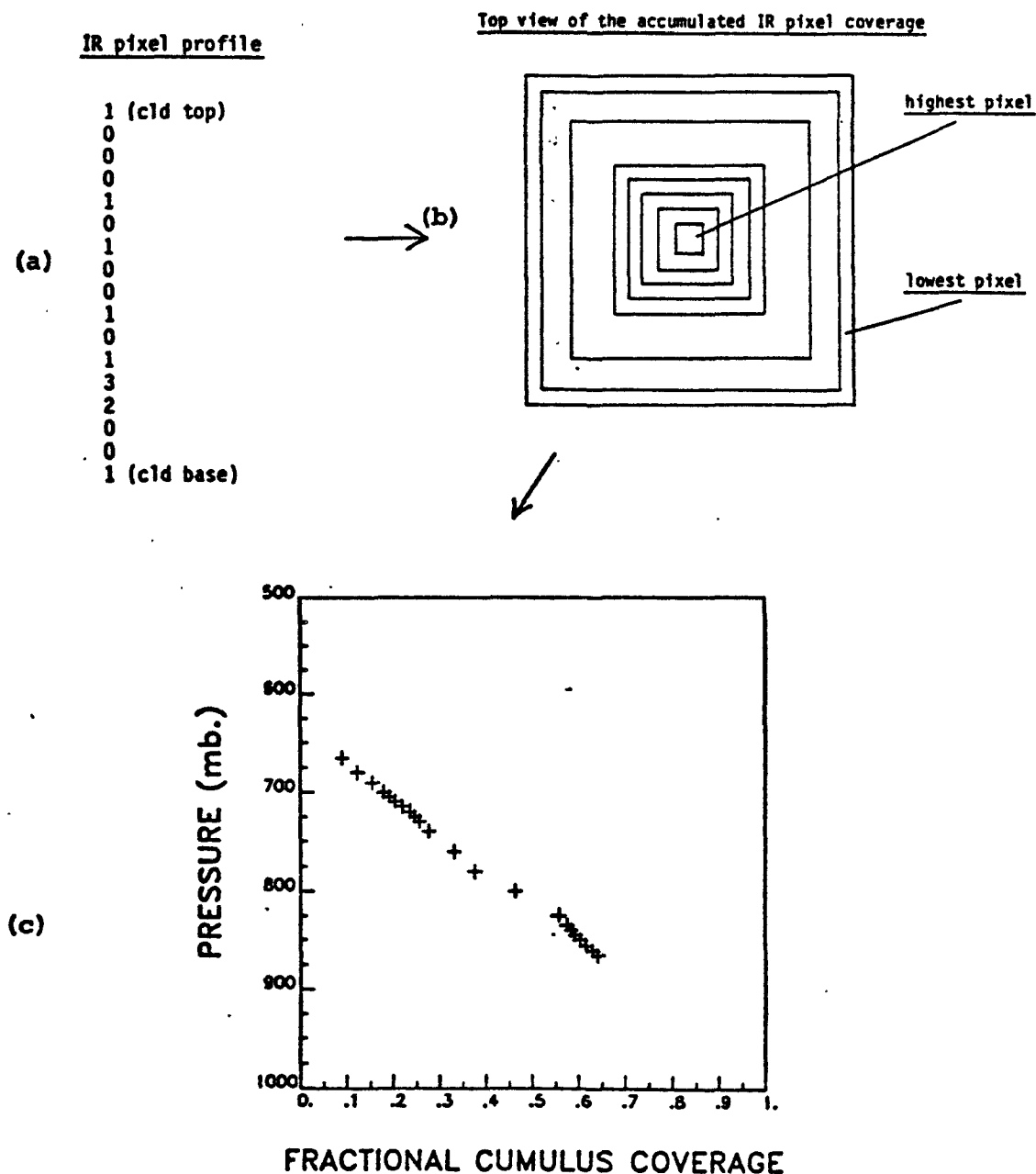


Figure 2.2-15. An illustration of the process by which the frequency distribution of cumulus cloud-top heights is used to give the vertical distribution of fractional cumulus cloud cover:

- (a) profile of IR pixel data obtained from satellite observations,
- (b) the corresponding profile of cumulus cloud coverage via a regression analysis between observed IR pixel data and fractional cumulus cloud cover observed from the satellite visible imagery, and
- (c) final normalized cloud cover distribution.

available. In order to guard against a bias that may be introduced by the large number of grid cells in which there were zero IR pixels detected at any level, the data were grouped according to pixel count before the regression analysis was done. Figure 2.2-16 shows the data used for this analysis and the resulting regression curve. The figure is, according to the author's knowledge, a unique representation of satellite data and will itself serve as a source of future research. The equation of this curve which was then used to relate the number of IR pixels at a given height to the cumulus area coverage was determined to be:

$$A = 12.719 + 6.28927N + 0.685818N^2 \quad (15)$$

where N is the number of pixels and A is the resulting area coverage of cumulus clouds. The correlation coefficient for this analysis was 0.99. This relationship was then applied to the vertical IR pixel profile for each cell to give the vertical distribution of cumulus cloud cover shown in Figure 2.2-15(b). This profile was subsequently normalized to ensure a correspondence between the cloud cover obtained from the IR pixel data and that which was observed from the satellite's visible imagery. The result of this process is shown in Figure 2.2-15(c). The vertical distribution of cloud forcing functions required for the explicit approach used in this study is based on this profile, as determined for each grid cell, and will be discussed further in Section 2.5.

## REGRESSION ANALYSIS

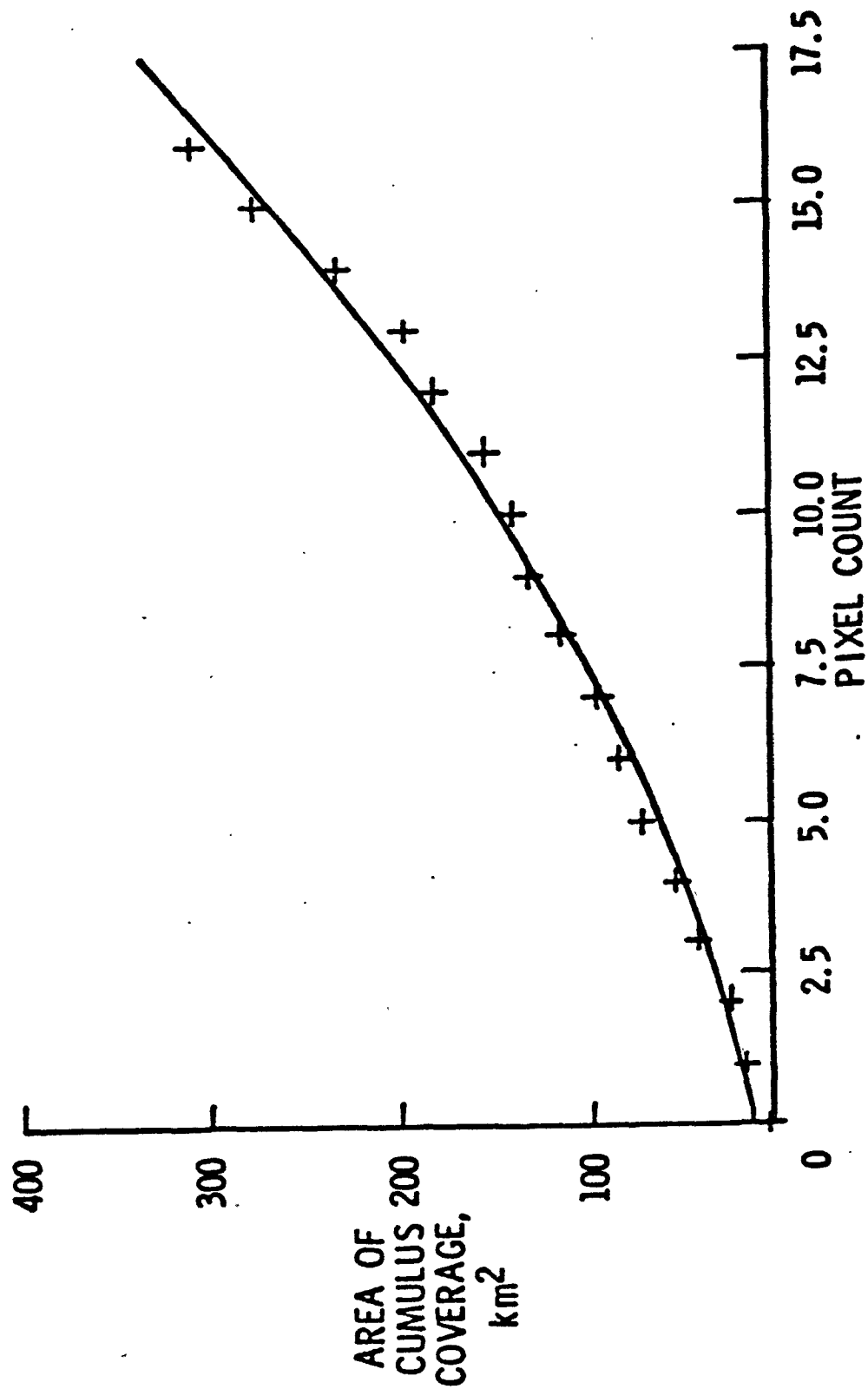


Figure 2.2-16. Regression curve showing the relationship between the IR pixel count and the area of cumulus coverage.

## (d) Other data fields

The vertical distribution of radiative heating rates used in this study were taken from the tabulated values of Doplick (1970) that correspond to the latitude and month of the study. The vertical profile of liquid water content was taken from Johnson (1975). Topographical data, used in the determination of the cloud-base height, were acquired from the data archives of NCAR.

### 2.3 The Entraining Plume Model

As indicated in Section 2.1, the first step in determining the cloud-base mass flux of a conservative tracer is to determine the cloud classes that are allowable, given the environmental profiles of temperature and moisture. This section will present the mathematical formalization of this selection process based on the conservation principles of mass and energy in a steady-state entraining plume.

We begin by assuming that the cloud field can be partitioned into cloud classes, represented by the assumed height of their respective updrafts, as shown in Figures 2.1-6(a) and (b). We further assume that each class can be uniquely represented by a positive constant which is chosen to be the fractional rate of mass entrainment  $\lambda$  given by

$$\frac{1}{m_u(\lambda_i, z)} \frac{\partial}{\partial z} m_u(\lambda_i, z) = \lambda_i \quad (16)$$

where  $\lambda_i$  is the fractional rate of mass entrainment for the  $i^{\text{th}}$  cloud

class and  $m_u(\lambda_i, z)d\lambda$  is the updraft mass flux attributed to the cloud class with entrainment rate  $\lambda_i$  such that  $\lambda_i - d\lambda/2 < \lambda_i < \lambda_i + d\lambda/2$ . It is assumed that the cloud field can be adequately described by a continuum of entrainment rates. Equation (16) therefore relates the updraft mass flux to the entrainment rate for the  $i^{\text{th}}$  cloud class. It is important to realize that although the value of  $\lambda_i$  is expected to vary according to the height of the cloud class as shown in Figure 2.1-7, we see from Equation (16), that  $\lambda_i$  is assumed to be independent of height for any individual cloud class. The actual determination of  $\lambda_i$  for each cloud class will be presented later in this section. For now however, the properties of an individual updraft will be discussed.

In this study we require not only the updraft mass flux at the cloud base, but also its distribution as a function of height above cloud base. To determine the vertical distribution of  $m_u$  we perform a transformation to the pressure coordinate system by applying the hydrostatic relationship to Equation (16) to obtain,

$$\frac{1}{m_u(\lambda_i, p)} \frac{\partial m_u(\lambda_i, p)}{\partial p} = -\frac{\lambda_i H}{p} \quad (17)$$

where the scale height  $H = RT_v/g$  (with  $R$  being the gas constant and  $T_v$  being the virtual temperature). The updraft mass flux in the  $i^{\text{th}}$  cloud class is then found by integrating Equation (17),

$$\int_{p_B}^p \frac{\partial \ln m_u(\lambda_i, p)}{\partial p} dp = - \int_{p_B}^p \frac{\lambda_i H}{p} dp \quad (18)$$



or

$$m_u(\lambda_i, p) = m_B(\lambda_i) \exp\left[-\int_{p_B}^p \frac{\lambda_i H}{p} dp\right] \quad (19)$$

where  $m_B(\lambda_i) = m_u(\lambda_i, p_B)$  is the cloud base mass flux distribution function of the  $i^{\text{th}}$  cloud class. Letting,

$$\eta(\lambda_i, p) = \exp\left[-\int_{p_B}^p \frac{\lambda_i H}{p} dp\right] \quad (20)$$

we obtain the simpler expression,

$$m_u(\lambda_i, p) = m_B(\lambda_i) \eta(\lambda_i, p) \quad (21)$$

where  $\eta$  is the normalized mass flux distribution of the  $i^{\text{th}}$  cloud class. The value of  $\eta$  increases from unity at cloud base to a maximum at cloud top, above which its value is set equal to zero.

Figure 2.3-1 illustrates profiles of  $\eta$  for a sample cloud class.

Following Johnson (1975), we now employ the assumption from the steady-state entraining plume theory that the flux divergence of the moist static energy equals the rate at which environmental moist static energy is entrained (Squires and Turner, 1962),

$$\frac{\partial}{\partial p} [m_u(\lambda_i, p) h_u(\lambda_i, p)] = \tilde{h}(\lambda_i, p) \frac{\partial}{\partial p} m_u(\lambda_i, p) \quad (22)$$

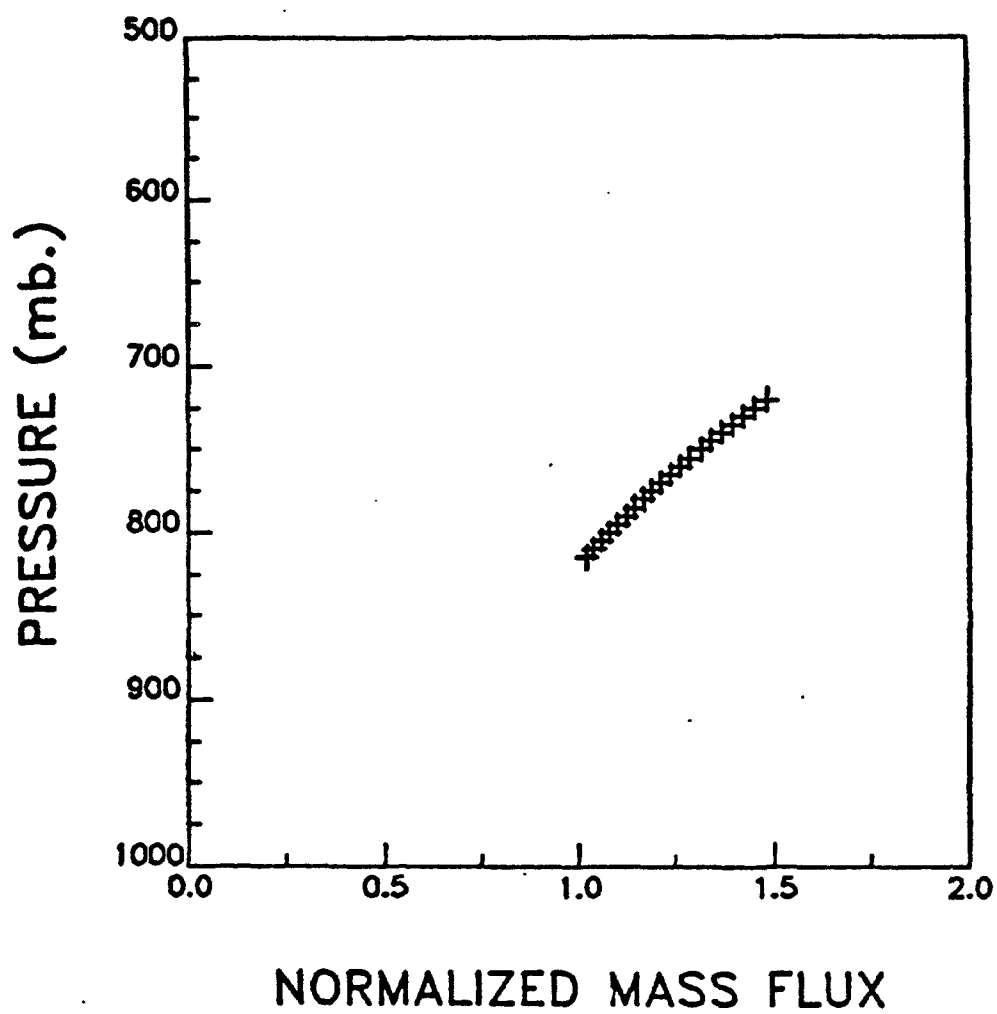


Figure 2.3-1. A vertical profile of the normalized mass flux distribution of  $\eta(\lambda_i, p)$ , for a typical cloud class.

where

$$h_u \equiv c_p T_u + gz + Lq_u \quad (23)$$

is the moist static energy within the updraft plume and  $\tilde{h}$  is the environmental moist static energy given by Equation (1). Equation (22) can be viewed as an energy conservation relationship for the updraft plume. It is this relationship, in conjunction with the appropriate boundary conditions for  $h_u$  that will enable us to assign a unique entrainment rate  $\lambda_1$  to each cloud class. Solving Equation (22) for  $h_u$ , using Equation (21) we get,

$$h_u(\lambda_1, p) = \frac{1}{n(\lambda_1, p)} \left[ h_u(p_B) - \int_{p_B}^p n(\lambda_1, p) \frac{\lambda_1 \tilde{h}}{p} dp \right] \quad (24)$$

which gives the moist static energy within the updraft plume at any pressure level between the cloud base (denoted by  $p_B$ ) and cloud top for the  $i^{\text{th}}$  cloud class which is uniquely described by  $\lambda_1$ . Therefore, once the cloud-top and cloud-base values of  $h_u$  have been determined, Equation (24) can be solved recursively for  $\lambda_1$ . Several different assumptions have been made in previous works regarding the determination of these boundary conditions. Yanai et al. (1973) and Ogura and Cho (1973) made the assumption that the cloud and environmental temperatures were the same at the cloud top and cloud bottom while Nitta (1975) assumed that the virtual temperature difference, neglecting the influence of liquid water, between the environmental and cloud air was negligible at the

two boundaries. Johnson (1975) compared the results obtained from assuming these different boundary conditions on the resulting mass flux distribution with those obtained by explicitly including the effects of liquid water on the cloud buoyancy. He found that more reasonable results were obtained when the virtual temperature calculations accounted for the presence of liquid water. We will employ Johnson's approach here with the following arguments reflecting his work.

Therefore, the cloud top is defined as the point at which,

$$T_u(\lambda_1, p)[1 + .608q_u(\lambda_1, p) - q_l(p)] = \tilde{T}(p)[1 + .608\tilde{q}(p)] \quad (25)$$

where  $q_l$  is the liquid water mixing ratio. With the assumptions regarding the cloud-top and cloud-base temperatures made, the evaluation of the moist static energy at these two levels can now be made.

Neglecting the pressure difference between the cloud and its environment we can use a Taylor's series to expand about the saturation point to obtain an expression for the updraft specific humidity  $q_u$ ,

$$q_u \cong \tilde{q}^* + \left( \frac{\partial \tilde{q}^*}{\partial T} \right)_p (T_u - \tilde{T}) \quad (26)$$

Using the updraft moist static energy  $h_u$  and the saturated, environmental moist static energy  $\tilde{h}^*$ , given respectively by Equations (23) and (2), we obtain the following expressions for the temperature and moisture excesses between the updraft and the environment:

$$T_u - \tilde{T} \cong \frac{1}{c_p} \frac{1}{1+\gamma} (h_u - \tilde{h}^*) \quad (27)$$

and

$$q_u - \tilde{q}^* \cong \frac{1}{L} \frac{\gamma}{1+\gamma} (h_u - \tilde{h}^*) \quad (28)$$

where

$$\gamma \equiv \frac{L}{c_p} \left( \frac{\partial \tilde{q}^*}{\partial T} \right)_p \quad (29)$$

Using

$$\tilde{q}^* = \frac{.622e_s}{(P - .378e_s)} \quad (30)$$

where  $e_s$  is the saturation vapor pressure, and the Clausius-Clapeyron equation, the following expression for  $\gamma$  can be obtained,

$$\gamma \equiv \frac{L}{c_p} \left( \frac{\partial \tilde{q}^*}{\partial T} \right)_p \cong \frac{.622L^2 e_s P}{c_p R_w T^2 (P - .378e_s)^2} \quad (31)$$

following Johnson (1975), Equations (25), (27) and (28) can be combined to give the following expression for the cloud-top moist static energy

$$h_u \cong \tilde{h}^* - \frac{L\mu(1+\gamma)}{1+.608\mu\gamma} [.608(\tilde{q}^* - \tilde{q}) - q_l] \quad (32)$$

where

$$\mu \equiv \frac{c_p T}{L} \quad (33)$$

Note that the value given for  $h_u$  in Equation (32) is independent of  $\lambda_1$  since we have assumed that only one class of clouds detrains, or has its cloud tops, at any given level.

This relationship, in conjunction with Equation (24) enables one to solve for the entrainment rate  $\lambda$  that is to be ascribed to each cloud class, given that the environment is conditionally unstable and therefore will permit clouds to occur. The procedure is as follows:

1. assuming  $q_k = 0$  at cloud base, use Equation (32) to determine the cloud base moist static energy  $h_u(p_B)$ .
2. move up an increment  $\Delta p$  from the cloud base, taken to be 5 mb in this study, and calculate the cloud-top moist static energy  $h_u(p_D)$  from Equation (32) where  $p_D$  indicates the detrainment level (cloud-top level)
3. iteratively solve the following equation for  $\lambda$ :

$$h_u(p_D) - \frac{1}{\eta(\lambda_1, p_D)} \left[ h_u(p_B) + \int_{p_B}^{p_D(\lambda_1)} \eta(\lambda_1, p) \frac{\lambda_1 \bar{H}}{p} dp \right] = 0 \quad (34)$$

4. repeat steps 2 and 3 until the top of the model atmosphere is reached or at least until the maximum cloud top height is reached.

In actual practice, there were instances where the zeros of Equation (34) were nonexistent. In those cases, the value of  $\lambda$  was chosen to correspond to the minimum of the equation.

Upon completion of steps 1-4 one will necessarily have obtained the distribution of  $\lambda_1(p)$  which is the vertical profile of the

entrainment rates as a function of assumed cloud-top pressures.

This, therefore completes the first phase of the task of solving for the cloud-base pollutant flux distribution. Figure 2.3-2 illustrates a profile of  $\lambda_1(p)$  thus obtained. By defining the cloud field in terms of cloud classes, each of which has had a unique entrainment rate ascribed to it, one is able to explicitly link the cloud-base pollutant flux due to a particular cloud class to the increase in the concentration of a conservative tracer occurring at its detrainment height, i.e. cloud top. If this air parcel is followed in a Lagrangian sense, only those clouds that have cloud tops at the altitude of the air parcel will contribute to the parcel's increase in pollutant concentration.

Using the same conservation principle for a conservative tracer as was used for moist static energy in Equation (22), a determination of the in-cloud concentration of the particular tracer can be determined from an equation analogous to Equation (24) with a variable representing the tracer mixing ratio replacing the terms for the updraft moist static energy,  $h_u$ . Such a relationship for the in-cloud tracer concentration does have the short-coming of neglecting any sources and sinks for the tracer that may be present in the cloud. Within the guidelines of constructing an operational module for use in a regional oxidant transport model, it was assumed that the impact that such processes would have on the regional scale ozone distribution would be small.

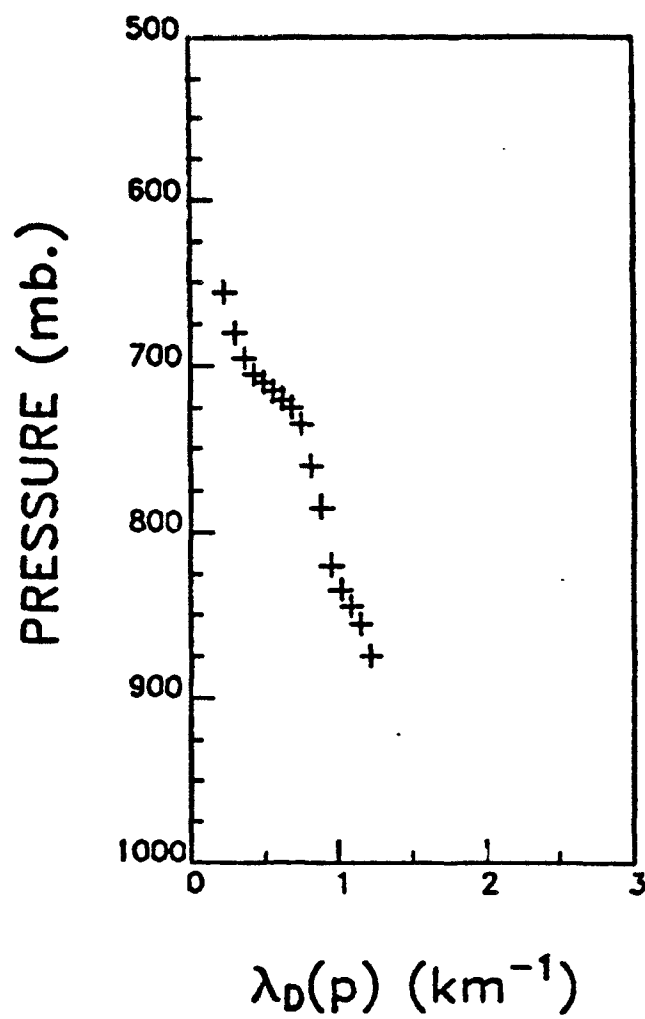


Figure 2.3-2. Example of model derived entrainment rates  $\lambda_i(p)$ .



#### 2.4 Determination of the Convective-scale Forcing from Synoptic-scale Variables

Having obtained a continuum of allowable cloud classes via the methodology outlined in Section 2.3, we now proceed to determine the cloud forcing functions required for the implicit approach used in this study. As noted in Section 2.1 and illustrated in Figure 2.1-3, the determination of the forcing functions constitutes the second step in the process of determining the cloud-base mass flux distribution for a convective cloud field. As mentioned in Section 2.1, the determination of the cloud forcing terms from synoptic-scale variables will be devoid of subsynoptic-scale features. A formalism designed to fill in this spectral gap is presented in Section 2.5, where the cloud forcing terms are determined from satellite data.

The convection associated with a cumulus cloud field is the result of many forces, but they are usually only parameterized in terms of the 'apparent heat source', 'apparent moisture sink', and radiative cooling. Of these forcing mechanisms, the 'apparent heat source' and 'apparent moisture sink' are deduced in terms of the environmental budgets of heat and moisture as the following analysis will show.

Another important point of this section is the demonstration of how the motion on the convective scale is influenced by the properties of the larger synoptic-scale. The pioneering efforts of Ooyama (1964) and Charney and Eliassen (1964) made great strides in the quest to understand the interactions between the synoptic and convective scales. They introduced the concept of Conditional Instability of the Second Kind (CISK) which describes how the cumulus and synoptic-scale

motions actually cooperate. In this process, the cumulus clouds provide the heat which aids the growth of the synoptic-scale waves while the synoptic-scale feature supplies the moisture that maintains the cumulus clouds. It has since been well established that the net effect of an ensemble of cumulus clouds is to cool and moisten the environment through detrainment of cloud air and to warm and dry the environment through subsidence induced motions (Betts, 1973a,b; Ooyama, 1971). It has therefore been the goal of cumulus parameterization to determine not how an individual cumulus cloud modifies the environment, but how an ensemble or group of such clouds influences the large-scale features. The derivation in this section will show how the synoptic-scale budgets of heat and moisture, combined with radiational cooling are related to the vertical flux divergence of the convective-scale moist static energy and follows the approach taken by Arakawa and Schubert (1974), Ogura and Cho (1973) and Johnson (1975).

Ignoring the effects of ice phase latent heat release, the heat budget for a parcel of air can be expressed in terms of the net rates of condensational heating ( $c$ ), evaporational cooling ( $e$ ) and radiative heating ( $Q_R$ ) in the following way:

$$\frac{Ds}{Dt} = L(c-e) + Q_R \quad (35)$$

where the dry static energy,  $s \equiv c_p T + gz$ ,  $L$  is the latent heat of condensation, and  $D/Dt$  is the total derivative operator defined as:

$$\frac{D}{Dt} \equiv \frac{\partial}{\partial t} + \mathbf{V} \cdot \nabla_h + \omega \frac{\partial}{\partial p}$$

Using specific humidity ( $q$ ) as the variable, the moisture budget can similarly be written as:

$$\frac{Dq}{Dt} = -c + e \quad (36)$$

Expanding the total derivative in (35), for example,

$$\frac{Ds}{Dt} = \frac{\partial s}{\partial t} + \underline{V} \cdot \nabla_h s + \omega \frac{\partial s}{\partial p} = L(c-e) + Q_R \quad (37)$$

and using the continuity equation,

$$\nabla \cdot \underline{V} + \frac{\partial \omega}{\partial p} = 0 \quad (38)$$

Equation (37) becomes,

$$\frac{\partial s}{\partial t} + \nabla_h \cdot (\underline{V}s) = \frac{\partial}{\partial p} (\omega s) = L(c-e) + Q_R \quad (39)$$

applying the Reynold's averaging technique by substituting

$$\underline{u} = \bar{u} + u', \quad \underline{v} = \bar{v} + v', \quad \underline{\omega} = \bar{\omega} + \omega', \quad s = \bar{s} + s'$$

and averaging over an area (grid square) large enough to contain a statistically representative sample of the cumulus cloud field and yet small in comparison to the synoptic field, we get:

$$\frac{\partial \bar{s}}{\partial t} + \nabla_h \cdot (\bar{\underline{V}} \bar{s}) + \nabla_h \cdot (\overline{\underline{V}' s'}) + \frac{\partial}{\partial p} (\bar{\omega} \bar{s}) + \frac{\partial}{\partial p} (\overline{\omega' s'}) = L(\bar{c} - \bar{e}) + \bar{Q}_R \quad (40)$$

assuming that  $\nabla_h \cdot (\overline{\mathbf{V}'s'}) \ll \partial(\overline{\omega's'})/\partial p$  we get:

$$Q_1 \equiv \frac{\partial \overline{s}}{\partial t} + \nabla_h \cdot (\overline{\mathbf{V}} \overline{s}) + \frac{\partial}{\partial p} (\overline{\omega} \overline{s}) = L(\overline{c-e}) + \overline{Q_R} - \frac{\partial}{\partial p} (\overline{\omega's'}) \quad (41)$$

for the heat budget and similarly:

$$Q_2 \equiv -L \left[ \frac{\partial \overline{q}}{\partial t} + \nabla_h \cdot (\overline{\mathbf{V}} \overline{q}) + \frac{\partial}{\partial p} (\overline{\omega} \overline{q}) \right] = L(\overline{c-e}) + L \frac{\partial}{\partial p} (\overline{\omega'q'}) \quad (42)$$

for the moisture budget, where  $Q_1$  and  $Q_2$  are respectively termed the 'apparent heat source' and 'apparent moisture sink' and gives a measure of the heating and moisture depletion that a cumulus cloud field has on the large-scale environment. These quantities are determined using the methods described in Section 2.2. Since the moist static energy is defined by  $h \equiv s + Lq$ , Equations (41) and (42) may be combined to give:

$$Q_1 - Q_2 - \overline{Q_R} = \frac{\partial \overline{h}}{\partial t} + \nabla_h \cdot (\overline{\mathbf{V}} \overline{h}) + \frac{\partial}{\partial p} (\overline{\omega} \overline{h}) = -\frac{\partial}{\partial p} (\overline{\omega'h'}) \quad (43)$$

The parameterization and interpretation of the r.h.s. of Equation (43), which represents the vertical flux divergence of moist static energy due to convective scale motion, forms the basis for calculating the cloud-base mass flux. This quantity can then be used to determine the vertical redistribution of a conservative tracer. The parameterization of the r.h.s. of Equation (43) is described in Section 2.6.

Rewriting equation (43), following Johnson (1975) we define

$$F(p) \equiv -\frac{1}{g} \int_{p_T}^{p_B} (Q_1 - Q_2 - Q_R) dp \quad (44)$$

which results in:

$$F(p_B) \equiv \left( -\frac{1}{g} (\overline{\omega' h'}) \right)_B \quad (45)$$

which is the total convective heat flux, sensible plus latent, at cloud base. From the meaning of  $Q_1$ ,  $Q_2$  and  $Q_R$  we can conceptually see then that  $F(p_B)$  is the summation of the cloud forcing terms, appearing in the integrand in Equation (44), over the depth of the cloud field. This term will be derived from another framework in Section 2.5 and will form the basis of a new approach in determining the cloud-base mass flux.

## 2.5 Determination of the Convective-scale Forcing from a 'Bulk' Perspective

Section 2.4 showed how the convective-scale 'apparent heat source' and 'apparent moisture sink' terms are deduced from the synoptic-scale budgets of heat and moisture. These terms, along with the radiative heating rate, have been used by many researchers to determine the convective cloud-base mass flux once the magnitude of these large-scale forcing mechanisms have been determined. Although this approach has been shown to give reliable results when applied to tropical regions (Yanai et al., 1973; Arakawa and Schubert, 1974; Johnson, 1975, 1977), it encounters several problems when applied to

a mid-latitude situation in an operational sense, some of which were mentioned in Section 2.1. As illustrated in Figure 2.1-3, this section proposes an alternative formalism for determining the convective-scale forcing that employs the use of visible and infrared satellite imagery. This approach has been labeled as the explicit method in Section 2.1.

The method described in this section centers around earlier works by Kuo (1965, 1974). In his works he obtained the area of a cumulus cloud by proposing a relationship between the half-life of the cloud, the moisture needed to form the cloud and the net moisture convergence as determined from synoptic-scale variables and ground evaporation. In this work Kuo's process has been inverted to determine the effective net moisture convergence based on a vertical distribution of cumulus cloud cover determined from satellite observations.

We begin by realizing that what the satellite observes includes not only those clouds that are actively venting pollutants from the mixed layer, but also those that have passed their development stage and are dissipating. In order to differentiate between these cloud types, we employ the concepts developed by Stull (personal communication) and Deardorff et al. (1980) to determine the active updraft area for each grid cell. As depicted in Figure 2.1-5, the fractional area covered by these updrafts is quite small.

The relationship between the updraft area and the total cloud area appears to be a very complex one. Zipser and LeMone (1980) found that cumulonimbus updrafts may occupy 15 - 18% of the total cloud area. It is expected, however, that although the ratio of updraft area to cloud area may vary substantially, the coverage of

updrafts in relation to the larger scale may be only a few percent (Bjerknes, 1938; Zipser and LeMone, 1980). It is this small number that must be determined if satellite data are to be explicitly used in obtaining cloud-base mass fluxes.

Once the total updraft area is determined, the ratio of updraft area to total cloud area, as determined by the satellite's visible imagery, is obtained. Upon assuming that this ratio is independent of cloud class one is able to determine the spectral distribution of updraft area by multiplying the vertical profile of cumulus coverage by this ratio. This distribution, along with a specification of the half-life and the moisture requirement for each cloud class is then utilized in determining the effective net moisture convergence which is used as the forcing function for the explicit method.

The approach we will follow in this section to obtain a value for the updraft area will parallel that of Stull (personal communication). Inherent to this approach is the recognition of the existence of an entrainment zone, the concept of which was developed by Deardorff et al. (1980), and is illustrated in Figure 2.5-1.

The entrainment zone is bounded on the top by height  $H_2$  which marks the highest level to which mixed-layer thermals can penetrate. In the absence of clouds, mixed-layer air will not penetrate above this level. The bottom of this zone is bounded by  $H_1$  which represents the highest level at which most of the air can be identified as mixed-layer air. The averaged height of the local mixed-layer top,  $Z_1$ , is assumed to be located near the middle of this zone of thickness  $\Delta H = H_2 - H_1$ . The occurrence of clouds, which we assume form at the 'top' of the mixed layer, is then dependent on whether or not

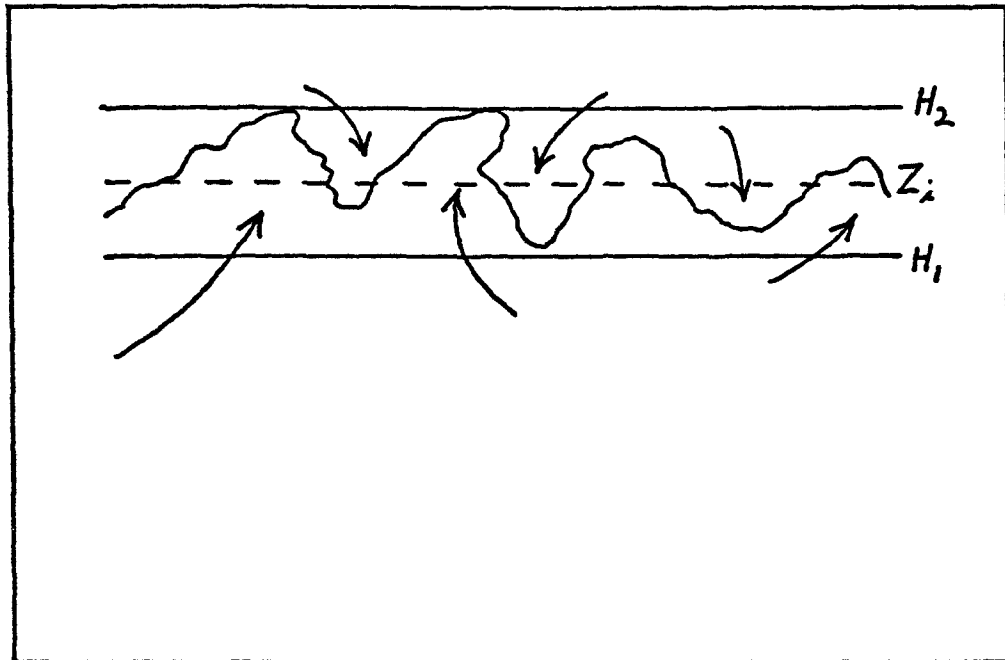


Figure 2.5-1. An illustration of the entrainment zone which exists between the mixed layer and the more stable cloud layer above is shown.  $H_2$  represents the highest level to which mixed layer air can penetrate.  $H_1$  marks the highest level at which most of the air can be identified as mixed layer air.



the local Lifting Condensation Level (LCL) lies within the entrainment zone. The location of the LCL was determined from the following equation:

$$Z_{LCL} \cong B(T-T_d)_{sfc} + Z_{sfc} \quad (46)$$

where  $B = 120$  m,  $(T-T_d)_{sfc}$  is the surface dew-point depression and  $Z_{sfc}$  is the terrain height. It was determined that an explicit determination of the local mixed-layer height was outside the scope of this work, however, for the purpose of executing the present model, it was assumed that:

$$Z_1 = Z_{LCL} \quad (47)$$

which is a reasonable assumption for a well-established, steady-state boundary layer. Once the local mixing height has been located by Equation (47), the thickness of the entrainment zone  $\Delta H$  is obtained following Stull (personal communication). In his work, he obtained the following relationship between  $Z_1$  and  $\Delta H$  from the results of Deardorff et al. (1980):

$$\frac{\Delta H}{Z_1} \cong 0.19 + 1.07 \frac{\theta w_*^2}{g \Delta \theta Z_1} \quad (48)$$

where  $\theta$  is the mixed-layer potential temperature,  $\Delta \theta$  is the potential temperature jump between the mixed layer and the overlying stable layer,  $g$  is the gravitational constant and  $w_*$  is the free convection scaling velocity. Stull states that values of  $\Delta H/Z_1$  normally range

from 0.20 to 0.25, realizing that in certain situations, a value of 0.5 may be attained. Physically, this means that the depth of the entrainment zone ranges from 20% to 25% of the mixed-layer depth. This is in stark contrast to previous studies in which the transition zone between the mixed layer and cloud layer is assumed to be infinitely thin (Ogura et al., 1977; Arakawa and Schubert, 1974). Due to the lack of better data Stull let

$$\frac{\Delta H}{Z_1} \approx 0.23 \quad (49)$$

Since boundary-layer mechanics are not explicitly incorporated in this effort, the value of 0.23 will likewise be assumed. Therefore, given the value of  $Z_1$  from Equation (47),  $\Delta H$  can be determined from Equation (49). The location of  $H_1$  and  $H_2$  are then determined by assuming that the locally averaged mixed-layer height ( $Z_1$ ) is located at the center of  $\Delta H$ .

As mentioned earlier in this section, the existence of clouds is dependent on the location of the LCL relative to the entrainment zone. Due to the transitory nature of  $Z_1$  in space and time, given that the LCL does lie within  $\Delta H$ , the fractional coverage of cumulus clouds can therefore best be described in a statistical sense. Stull utilized this premise by deriving a Gaussian probability density distribution function  $G(z)$ , which appeared to fit the data of Deardorff et al. (1980), such that the probability of finding the local  $Z_1$  within the entrainment zone  $\Delta H$ , over a specified local domain can be expressed as:

$$1 = \int_{H_1}^{H_2} G(\xi) d\xi \quad (50)$$

which means that one is certain to find the local mixed-layer top ( $Z_1$ ) within the entrainment zone. The probability of finding mixed-layer air at height  $z$  would then (following Stull) be:

$$P(z) = 1 - \int_{H_1}^z G(\xi) d\xi = \int_z^{H_2} G(\xi) d\xi \quad (51)$$

Therefore, the probability of finding clouds within the entrainment zone would be:

$$\sigma = P(Z_{LCL}) = \int_{Z_{LCL}}^{H_2} G(\xi) d\xi \quad (52)$$

Stull interpreted the value of  $\sigma$  resulting from this equation to give the fractional coverage of cumulus clouds. However, since the tracing fluid used by Deardorff et al. (1980) in his tank experiment was an inert substance which lacked the capability of releasing latent heat as water vapor would, we take the meaning of  $\sigma$  to be representative of the updraft area instead of total cloud area. The value of  $\sigma$  thus obtained can therefore be interpreted as the fractional area coverage of convective updrafts associated with forced and active cumulus convection. Forced clouds are those clouds that have not reached their Level of Free Convection (LFC) and are merely negatively buoyant remnants of boundary layer thermals. They can be identified in the atmosphere as cumulus humilis. Active clouds are those that have reached their LFC and have therefore become positively buoyant due to the release of latent heat.

The probability density distribution function in Equation (52) has been found to have the form of (Stull, personal communication):

$$G(z) = \frac{2.42}{\Delta H} \exp\left[-\frac{18(z - z_1 + \Delta H/8)^2}{\Delta H^2}\right] \quad (53)$$

I have found that the application of Equations (52) and (53) for determining the fractional coverage of cumulus updrafts was very sensitive to the value given to the lower limit of integration in Equation (52). This is undoubtedly a result of the inability to calculate  $Z_1$  and  $Z_{LCL}$  explicitly from a boundary-layer model, in view of the vertical resolution of the model and the smoothed nature of the input data. However, reasonable and consistent results were obtained by setting the lower limit of the integral to the value of  $Z$  corresponding to 5 mb above the LCL. This limit may, after all, be reasonable since this distance could correspond to the difference between LFC and LCL heights, implying that only active clouds are considered. This would be consistent with the satellite data since it is incapable of resolving forced clouds (those on the cumulus humilis scale), the cloud tops of which should be within the range of 5-10 mb above cloud base. The sensitivity of Equation (52) to the lower limit of the integral will be discussed in Chapter 4.

The ratio of total fractional updraft area, as given by Equation (52), to the total cloud area, is then:

$$\epsilon = \sigma/C \quad (54)$$

where  $C$  is the total observed cumulus cloud cover at cloud base as determined from the satellite's visible imagery. Assuming that this ratio is constant for all cloud classes, the fractional cloud updraft area for each cloud class can then be determined by:

$$\beta(p) = \epsilon [c(p) - c(p - \Delta p)] \quad (55)$$

where  $c(p)$  represents the satellite observed cloud cover at each 5 mb level (via Section 2.2c).

Since the result of Section 2.3 was a unique distribution of entrainment rates as a function of pressure, there exists within the domain of  $\lambda(p)$  a unique value of  $p$  for every  $\lambda_1$  such that the following one-to-one mapping occurs:

$$\beta(p) \rightarrow \beta^*(\lambda_1) \quad (56)$$

thereby giving the fractional updraft area as a function of entrainment rate (or cloud class) from:

$$\sigma(\lambda_1) = \beta^*(\lambda_1) \quad (57)$$

The spectral distribution of the fractional cloud updraft area is then related to the total fractional updraft area by,

$$\sigma = \int \sigma(\lambda_1) d\lambda \quad (58)$$

As mentioned in the beginning of this section, in order to invert Kuo's scheme, other parameters besides the spectral distribution of cloud updraft area must be determined in order to make the parameterization of the 'bulk' forcing term complete. We now determine the amount of moisture needed ( $\Gamma_c(\lambda_i)$ ) to form the updraft cross-sectional area  $\sigma(\lambda_i)$  of a cloud in the  $i^{\text{th}}$  cloud class. The moisture requirement can be divided into two terms. The first term represents the moisture needed to produce the expected temperature differential between the cloud updraft and the environmental temperature at that level, caused by latent heat release; while the second term gives the increase in moisture content in the cloud column over that in the environment, as shown in the following equation:

$$\Gamma_c(\lambda_i) = \frac{1}{g} \int_{p_T}^{p_B} \left[ \frac{c_p}{L} (T_u - \bar{T}) + q_u - \bar{q} \right] dp \quad (59)$$

where  $p_T$  and  $p_B$  are respectively the cloud-top and cloud-base pressures and  $T_u$  and  $q_u$  are determined from Equations (27) and (28). The following functional form was assumed for  $\tau(\lambda_i)$ , the half-life of clouds in the  $i^{\text{th}}$  cloud class:

$$\tau(\lambda_i) = [TMN + ((\lambda_n - \lambda_i)/\lambda_n)TMX] 2\bar{q}/q^* \quad (60)$$

where TMN and TMX are set to 15 and 30 minutes respectively and  $\lambda_n$  is the entrainment rate of the lowest cloud class. This ascribes half-lives of 15 and 45 minutes to clouds with respective entrainment rates of  $\lambda_i = \lambda_n$  and  $\lambda_i = 0$  and relative humidities of 50% at  $.5(p_B - p_T)_i$ . The computation of  $\tau(\lambda_i)$  is set to limit  $\lambda < 3.5$  and  $\bar{q}/q^* > 0.10$ . This scheme, although

apparently arbitrary, gives values that are within a factor of 2 or 3 of observed values (Lopez, 1977; Kitchen and Caughey, 1981).

The following relationship, essentially identical to that proposed by Kuo, will now be solved for the effective net moisture convergence ( $\Gamma_{f1}$ ) required for each cloud class:

$$\sigma(\lambda_1)\Gamma_c(\lambda_1) = \tau(\lambda_1)\Gamma_f(\lambda_1) \quad (61)$$

which states that during the half-life  $\tau(\lambda_1)$ , the amount of moisture  $\Gamma_f(\lambda_1)$  must be provided for the fractional updraft area  $\sigma(\lambda_1)$  corresponding to the  $i^{\text{th}}$  cloud class. Since the above computation employs a diagnostic determination of the cloud field from satellite data, the value of  $\Gamma_f(\lambda_1)$  thus obtained represents an effective 'bulk' forcing term due not only to the advection of moisture which could have been calculated on the synoptic scale, but also implicitly includes the integrated effect of every force that was occurring at the time of the satellite observation. Since the clouds that the satellite detected are the combination of forces that span the entire spectral scale, they do not therefore need to be individually named nor explicitly parameterized for, only the effective 'bulk' forcing term need be determined. The remaining problem is then how to distribute this 'bulk' forcing term in the vertical. From Equation (44) we saw that  $F(p)$  was the integrated effect of  $Q_1 - Q_2 - Q_R$  over the depth of the cloud field. This could now be considered analogous to the meaning of

$$\Gamma_f = \int \Gamma_f(\lambda_1)d\lambda \quad (62)$$

where  $\Gamma_f$  is the integrated effect of the net moisture convergence over all cloud classes. This quantity is then vertically distributed according to the vertical distribution of cumulus cloud cover, such that the forcing and cloud cover at any level are directly proportional to each other.

## 2.6 Determination of the Convective Cloud Mass Flux

Having obtained the function  $\lambda_D(p)$  from Section 2.3 and the convective-scale forcing terms from Sections 2.4 or 2.5, we are now ready to determine the parameterization for the convective-scale vertical flux divergence for moist static energy in terms of the cloud-base mass flux using the model of the steady-state entraining plume discussed in Section 2.3. The result of this section will be an integral equation which must then be subsequently solved for the cloud-base mass fluxes as a function of cloud class.

It is assumed that the fractional area covered by cumulus updrafts is  $\ll 1$ . With  $\sigma(\lambda)d\lambda$  defined as the fractional area occupied by updrafts with entrainment rates such that  $\lambda - d\lambda/2 \leq \lambda \leq \lambda + d\lambda/2$ , the grid-scale average of any variable  $\alpha$  can then, following Johnson (1975), be written as:

$$\bar{\alpha}(p) = \int_0^{\lambda_D(p)} \alpha_u(\lambda, p) \sigma_u(\lambda) d\lambda + (1 - \sigma_u) \bar{\alpha} \quad (63)$$

— where  $\alpha_u$  and  $\bar{\alpha}$  are the values of  $\alpha$  in the updraft and the environment, respectively, and where,



$$\sigma_u(p) = \int_0^{\lambda_D(p)} \sigma_u(\lambda) d\lambda \quad (64)$$

is the total cumulus updraft area at pressure level  $p$ . Using Equation (63), the large-scale dry static energy and specific humidity can be expressed as,

$$\bar{s} = \sigma s_u + (1 - \sigma) \tilde{s} \quad (65)$$

and

$$\bar{q} = \sigma q_u + (1 - \sigma) \tilde{q} \quad (66)$$

or as,

$$\bar{s} = \sigma(s_u - \tilde{s}) + \tilde{s} \quad (67)$$

and

$$\bar{q} = \sigma(q_u - \tilde{q}) + \tilde{q} \quad (68)$$

Now since  $\sigma \ll 1$ ,  $(s_u - \tilde{s}) < \tilde{s}$  and  $(q_u - \tilde{q}) < \tilde{q}$ , we can make the approximations,

$$\bar{s} \approx \tilde{s} \quad \text{and} \quad \bar{q} \approx \tilde{q} \quad (69)$$

which indicate that the normally observed rawinsonde data can give a good approximation to the values of  $s$  and  $q$  in the cloud environment.

With these approximations we can determine the vertical convective flux of, for example, specific humidity in the following way:

$$\begin{aligned}
\overline{q'w'} &= \overline{q} \overline{w} - \overline{q} \overline{w} = \int_0^{\lambda_D(p)} q_u(\lambda, p) \omega_u(\lambda, p) \sigma_u(\lambda) d\lambda + (1 - \sigma_u) \widetilde{q} \widetilde{w} \\
&\quad - \widetilde{q} \left[ \int_0^{\lambda_D(p)} \sigma_u(\lambda) \omega_u(\lambda, p) d\lambda + (1 - \sigma_u) \widetilde{w} \right] \\
&= \int_0^{\lambda_D(p)} \sigma_u(\lambda) \omega_u(\lambda, p) [q_u(\lambda, p) - \widetilde{q}] d\lambda
\end{aligned} \tag{70}$$

Employing Leibnitz's rule in obtaining the vertical flux divergence we get,

$$\begin{aligned}
\frac{\partial}{\partial p} (\overline{q'w'}) &= \int_0^{\lambda_D(p)} \sigma_u(\lambda) \frac{\partial}{\partial p} [\omega_u(\lambda, p) (q_u(\lambda, p) - \widetilde{q})] d\lambda \\
&\quad + \sigma_u(\lambda_D) \omega_u(\lambda_D, p) [q_u(\lambda_D, p) - \widetilde{q}] \frac{d\lambda_D}{dp}
\end{aligned} \tag{71}$$

A similar equation can be obtained for the vertical flux divergence of dry static energy. It is interesting to note at this point in the derivation that since  $m_u(\lambda_D, p)d\lambda$  represents the mass flux from those clouds whose entrainment rate is such that  $\lambda_D - d\lambda/2 < \lambda_D < \lambda_D + d\lambda/2$ , the last term in Equation (71) is therefore recognizable and the detrainment of water vapor into the environment from clouds with tops as pressure  $p$ . A physical explanation for the first term will be delayed until a few more substitutions can be made.

Desiring a relationship between the specific humidity in the updraft and that in the environment that involves the mass flux, we turn to the conservation equation for water vapor in the updraft

realizing that its form will be similar to that of Equation (22) for moist static energy. We therefore have,

$$\frac{\partial}{\partial p}(m_u(\lambda, p)q_u(\lambda, p)) = \bar{q}\frac{\partial}{\partial p}m_u(\lambda, p) + c(\lambda, p) \quad (72)$$

where the condensation rate,  $c$ , is a sink of water vapor in the updraft. Equation (72) can be rewritten as,

$$\frac{\partial}{\partial p}m_u(q_u - \bar{q}) = -m_u\frac{\partial \bar{q}}{\partial p} + c(\lambda, p) \quad (73)$$

Using this relationship and the definition  $m_u(\lambda, p) \equiv -\sigma(\lambda)\omega(\lambda, p)$ , we get,

$$\begin{aligned} \frac{\partial}{\partial p}(\overline{q'\omega'}) &= \int_0^{\lambda_D(p)} [m_u(\lambda, p)\frac{\partial \bar{q}}{\partial p} - c(\lambda, p)]d\lambda - \\ &\quad m_u(\lambda_D, p)\frac{d\lambda_D}{dp}[q_u(\lambda_D, p) - \bar{q}] \end{aligned} \quad (74)$$

Now, since

$$\bar{c}(p) \equiv \int_0^{\lambda_D(p)} c(\lambda, p)d\lambda \quad (75)$$

we obtain,

$$-\frac{\partial}{\partial p}(\overline{q'\omega'}) = -M_u(p)\frac{\partial \bar{q}}{\partial p} + \bar{c}(p) + \delta(p)[q_u(\lambda_D, p) - \bar{q}] \quad (76)$$

where

$$\delta(p) \equiv m_u(\lambda_D, p) \frac{d\lambda_D}{dp} \quad (77)$$

The large-scale water vapor conservation Equation (42) can therefore be written as,

$$\frac{-Q_2}{L} = -M_u \frac{\partial \tilde{q}}{\partial p} + \bar{e}_u + \delta[q_u(\lambda_D, p) - \tilde{q}] \quad (78)$$

Equation (78) indicates that the apparent moisture sink due to the action of cumulus clouds can be accounted for in terms of the environmental sinking  $M_u \partial \tilde{q} / \partial p$  which compensates the updraft cumulus flux and is reduced by the detrainment of water vapor  $\delta(q_u - \tilde{q})$  and the evaporation of liquid water from updrafts.

As mentioned earlier, a similar derivation can be done for the vertical flux divergence of dry static energy,  $s$ . The result of which is,

$$Q_1 - Q_R = -M_u \frac{\partial \tilde{s}}{\partial p} - L\bar{e}_u + \delta[s_u(\lambda_D, p) - \tilde{s}] \quad (79)$$

The interpretation of Equation (79) is very similar to that of Equation (78) in that the apparent heat source, less the radiative heating term, is due to the sinking which is compensating for the cumulus updraft mass flux, the detrainment of  $s$  from cloud tops and is reduced by evaporational cooling from the liquid water detrained from the updrafts.

Combining these last two equations, we get the following relationship between the large-scale heat and moisture budgets and the vertical flux divergence of moist static energy due to cumulus updrafts:

$$Q_1 - Q_2 - Q_R = \delta [h_u(\lambda_D, p) - \bar{h}] - M_u \frac{\partial \bar{h}}{\partial p} \quad (80)$$

which states that the large-scale budget of moist static energy is determined by radiative heating, the environmental sinking in response to the cumulus updraft mass flux and the detrainment of moist static energy from cloud tops. Writing Equation (80) in its expanded form we have,

$$Q_1 - Q_2 - Q_R = m_B(\lambda) \eta_u(\lambda_D, p) \frac{d\lambda_D}{dp} [h_u(\lambda_D, p) - \bar{h}] \quad (81)$$

$$- \frac{\partial \bar{h}}{\partial p} \int_0^{\lambda_D(p)} m_B(\lambda) \eta_u(\lambda, p) d\lambda$$

This is a Volterra integral equation of the second kind. The unknown variable  $m_B(\lambda)$ , is the function that is required in order to determine the total cloud-base mass flux of a conservative tracer and, with the aid of Equation (76), the vertical redistribution of the tracer that is vented from the boundary layer and deposited into the cloud layer can now be determined.

The solution of Equation (81) is illustrated in Figure 2.1-8. In this figure it is shown that, as a result of assuming that only one cloud class is detraining at any given level (from Section 2.3) and that a total cloud forcing can be assigned at each level (from Section

2.4 or 2.5), the solution for the cloud-base mass flux as a function of cloud class is accomplished by solving the above equation 'from the top down'.

## CHAPTER 3

### MODEL EVALUATION AND INTERCOMPARISON

Two models have been described in the previous chapter. The first is an adaptation for this work of the model developed by Johnson (1975). The second is an approach that uses the formulation of Kuo (1965, 1974) to determine the environmental forcing of a cumulus ensemble based on a unique usage of satellite data. These two models have been respectively called the implicit (im) and explicit (ex) models in that the first model implicitly assumes a cloud field as a result of conditional instability in the environment and the second model explicitly incorporates satellite data into the calculations. These two models will be evaluated using a real data base which has also been described in the previous chapter. Three cells in the Summer Experiment study area have been chosen for this purpose and represent situations of weak, moderate and strong convection for a nonprecipitating scenario. Several graphs will be shown for each of the three cases. In each graph, the values along the ordinate (pressure) are given at the detrainment level (cloud-top height) for each cloud class under consideration, remembering from Section 2.3 that these levels were determined on the basis of the fractional rate of mass entrainment. Table 3-1 lists some of the basic characteristics of the cloud field. It should be noted at this point that the code provided by Johnson was executed using data that he had

provided to ensure that it was functioning properly before any modification to the code was attempted.

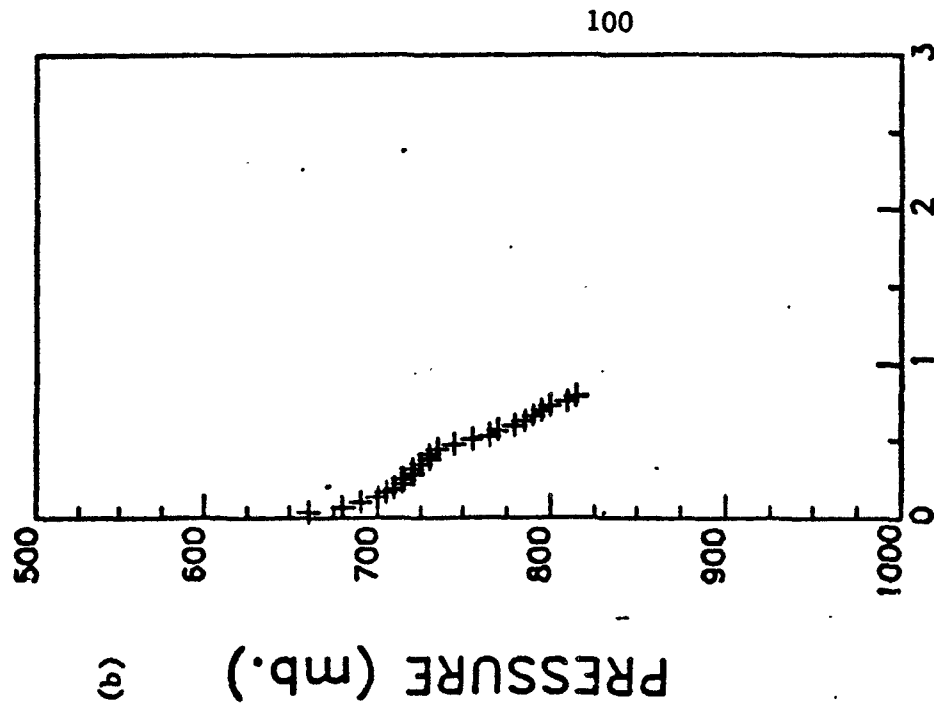
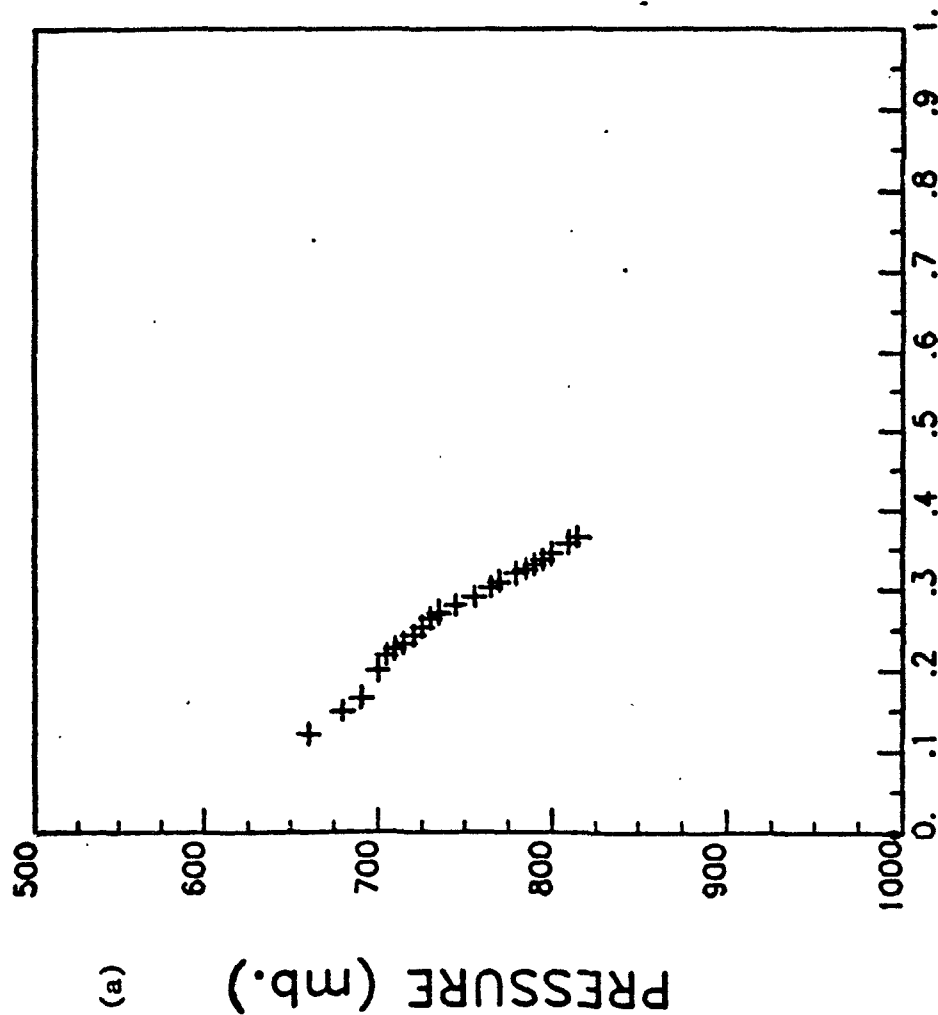
Table 3-1

case #	total cloud cov. (frac.)	cum. cloud cov. (frac.)	max. ht. (msl)	updraft area (frac.)	total cloud-base heat flux	
					(ex) (im)	
1	.574	.476	6000	.0107	264	107
2	.720	.533	2800	.0099	204	202
3	.331	.331	2200	.0072	166	66

Table 3-1. Basic characteristics of the cloud field for each grid cell chosen for an evaluation of the models presented. Units of heat flux are  $\text{W m}^{-2}$  (ex: explicit model; im: implicit model).

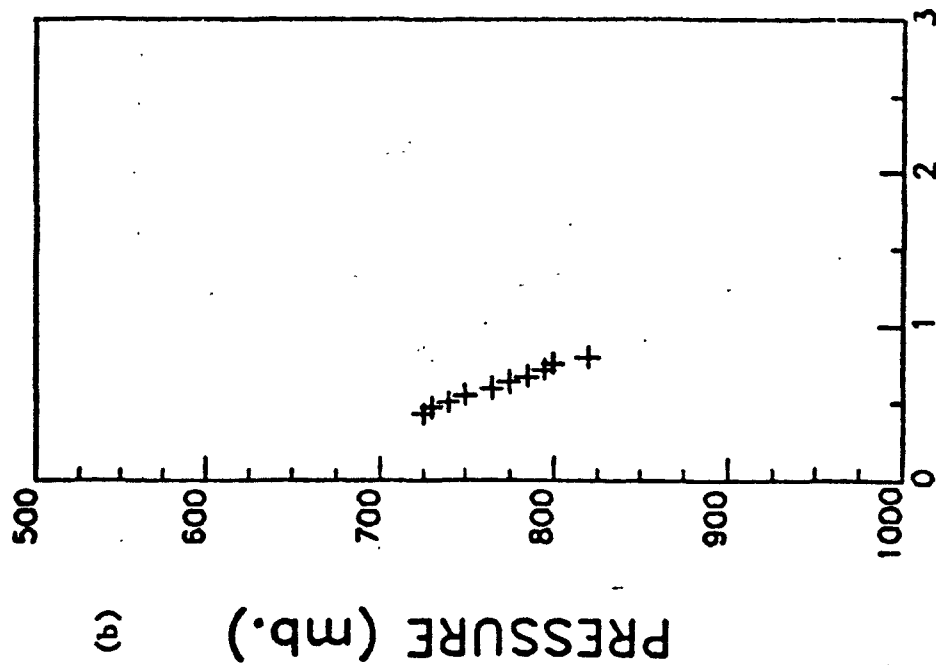
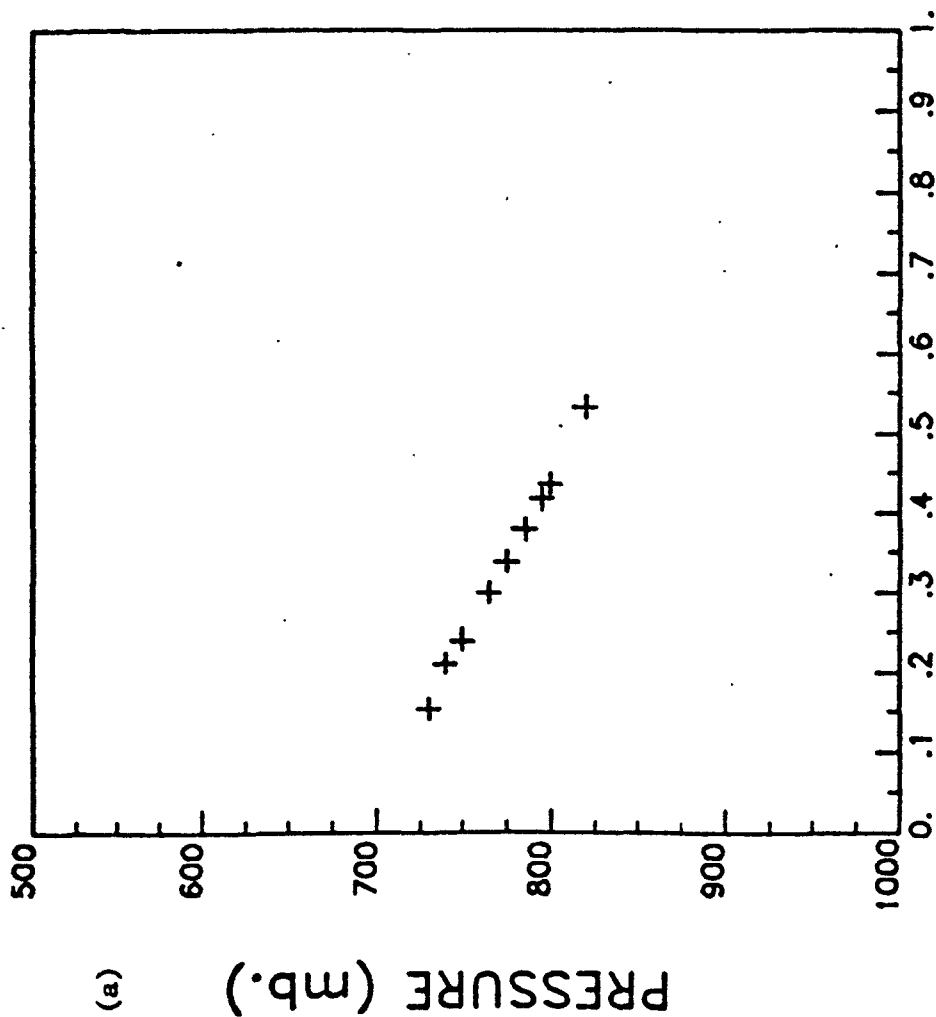
Figures 3-1, 3-2 and 3-3 illustrate the cumulus cloud cover profile (obtained from satellite data) along with the model derived entrainment rates for each cloud class for the three cases under consideration. The figures indicate that the model derived entrainment rates for the shortest cloud class are approximately the same for all three cases. The lack of spatial variability in these entrainment rates may illustrate a shortcoming in the model, which may be attributable to a lack of adequate spatial resolution in the synoptic-scale rawinsonde data. Since the entrainment rate profiles shown in these figures are incorporated into the formulation of both the explicit and implicit methods (see Figure 2.1-3), errors made in the determination of  $\lambda_D(p)$  will therefore be embedded into both methods. A more crucial determination, however, is  $d\lambda_D/dp$ , which, as one can see from Equation (81), is required to solve for the cloud base mass flux  $m_B(\lambda)$ . From Figures





## FRACTIONAL CUMULUS COVERAGE

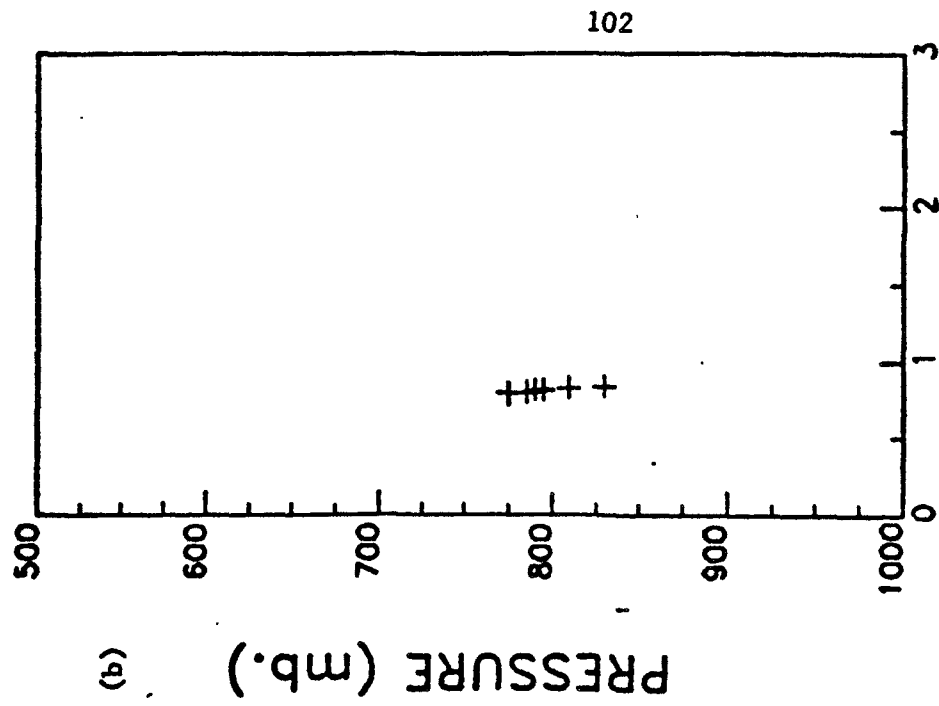
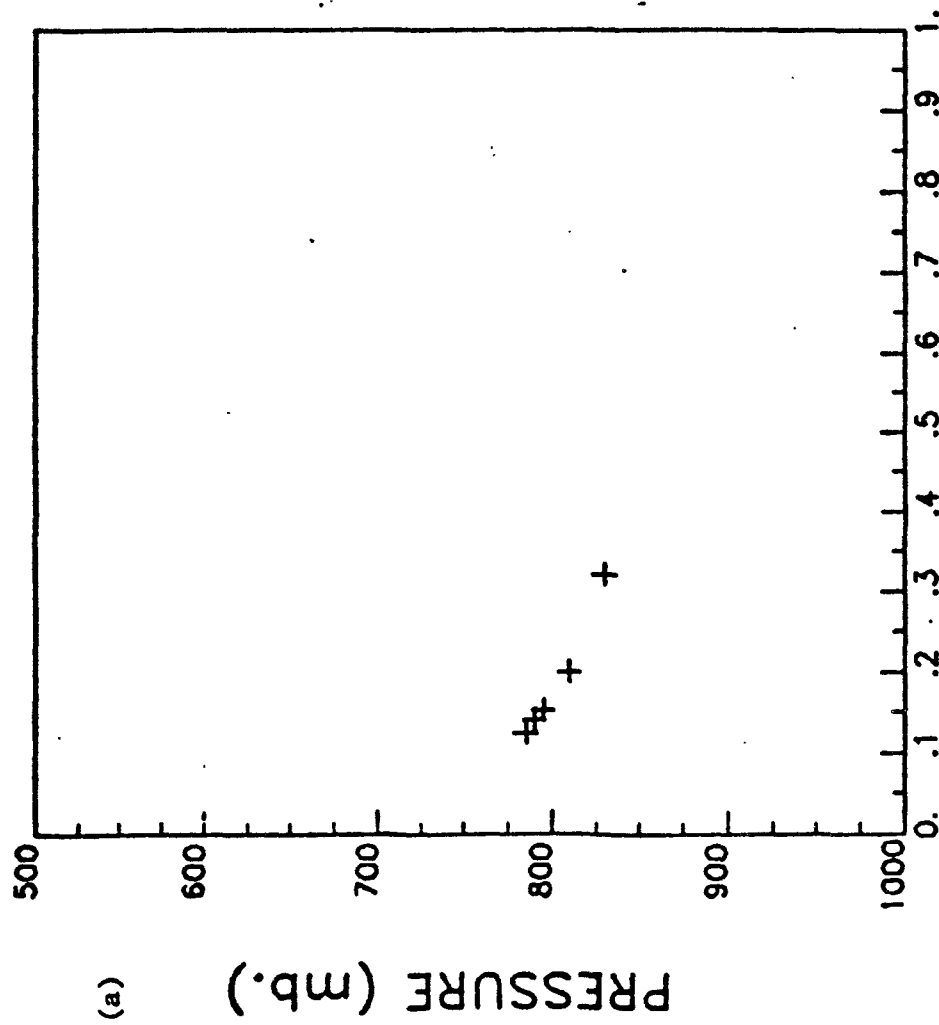
Figure 3-1. (a) fractional cumulus cloud coverage as a function of pressure as determined from satellite data, and (b) model derived entrainment rates as a function of cloud class for cell (5,20) at 20Z (case #1).



## FRACTIONAL CUMULUS COVERAGE

$\lambda_D(p)$  ( $\text{km}^{-1}$ )

Figure 3-2. (a) fractional cumulus cloud coverage as a function of pressure as determined from satellite data, and (b) model derived entrainment rates as a function of cloud class for cell (7,20) at 20Z (case #2).



## FRACTIONAL CUMULUS COVERAGE

Figure 3-3. (a) fractional cumulus cloud coverage as a function of pressure as determined from satellite data, and (b) model derived entrainment rates as a function of cloud class for cell (12,16) at 20Z (case #3).

3-1, 3-2 and 3-3 we see that  $d\lambda_D/dp$  for case #3 (Figure 3-3) is significantly less than that for the same relative portion of the  $\lambda_D(p)$  profile for cases 1 and 2. Since the solution of the Volterra equation (Equation 81) is sensitive to small  $d\lambda_D/dp$  in the region near the detrainment level (cloud top) of the lowest few cloud classes, a lower limit of  $0.0002 \text{ km}^{-1} \text{ mb}^{-1}$  for  $d\lambda_D/dp$  was therefore imposed on the system, thus preventing excessively large values of mass flux from being computed. A possible modification to the present formulation that would mitigate the problems outlined above will be mentioned later in this chapter.

The rationale for placing the profile of fractional cumulus coverage next to the profile of  $\lambda_D(p)$  is that the information contained in the calculated  $\lambda_D(p)$  profile concerning cloud-top heights should be a reflection of the information given in the observed profile of the fractional cumulus coverage. Remembering that (1) the values shown in, for example, Figure 3-1(b) are chosen at equal values of  $\Delta\lambda$ , and (2) the meaning of  $\lambda_D(p)$  (cloud-top detrainment pressure level), the regions where  $d\lambda_D/dp$  becomes large should imply that the detrainment levels (cloud-tops) of several cloud classes are calculated to be grouped near the same pressure level. Such a level exists between 700-725 mb in Figure 3-1(b). This calculated 'leveling-off' of the cloud-top heights is reflected in the observed profile of fractional cumulus coverage between 700-725 mb in Figure 3-1(a) and lends a degree of credibility to the model's depiction of the atmosphere, at least for deeper clouds. This relationship is again seen in Figure 3-2 where  $d\lambda_D/dp$  is nearly constant throughout the cloud layer as is the change in fractional cumulus cloud cover with pressure. It is difficult to

determine if this relationship is illustrated by the data shown in Figure 3-3, which represents a shallow nonprecipitating convective scenerio, due to the resolution problem outlined above.

Employing the solution of Equation (81) for  $m_B(\lambda)$  and Equations (20) and (21), the total convective upward mass flux that penetrates level  $p$  is given by,

$$M_u = \int_{\lambda=0}^{\lambda(p)} m_u(\lambda, p) d\lambda \quad (82)$$

Figure 3-4 shows the resulting profile of  $M_u$  (the vertical mass flux distribution) for the explicit and implicit models as applied to case #1. Mass conservation within the cell is then obeyed by determining the induced environmental motion ( $\bar{M}$ ) that is compensating the updraft mass flux  $M_u$  from Equation (4) given  $\bar{M}$ , which is obtained from Equations (12) and (13). One can see from the figure that the values from the two models are approximately equal at the top and bottom of the curve, with the explicit model having larger values at the intermediate levels. The difference in the shape of the profiles of  $M_u$  and  $\bar{M}$  between the explicit and implicit models is a result of their respective forcing functions which stem from an observed cumulus cloud profile (for the explicit method) or from synoptic-scale rawinsonde data (for the implicit method).

Figure 3-5 shows the cloud-base mass flux distribution,  $m_B(p)$ , resulting from the two models (for case #1) and is determined by,

$$m_B(p) = m_B(\lambda) d\lambda_D / dp \quad (83)$$

The graph of  $m_B(p) dp$  gives the cloud-base mass flux for clouds that

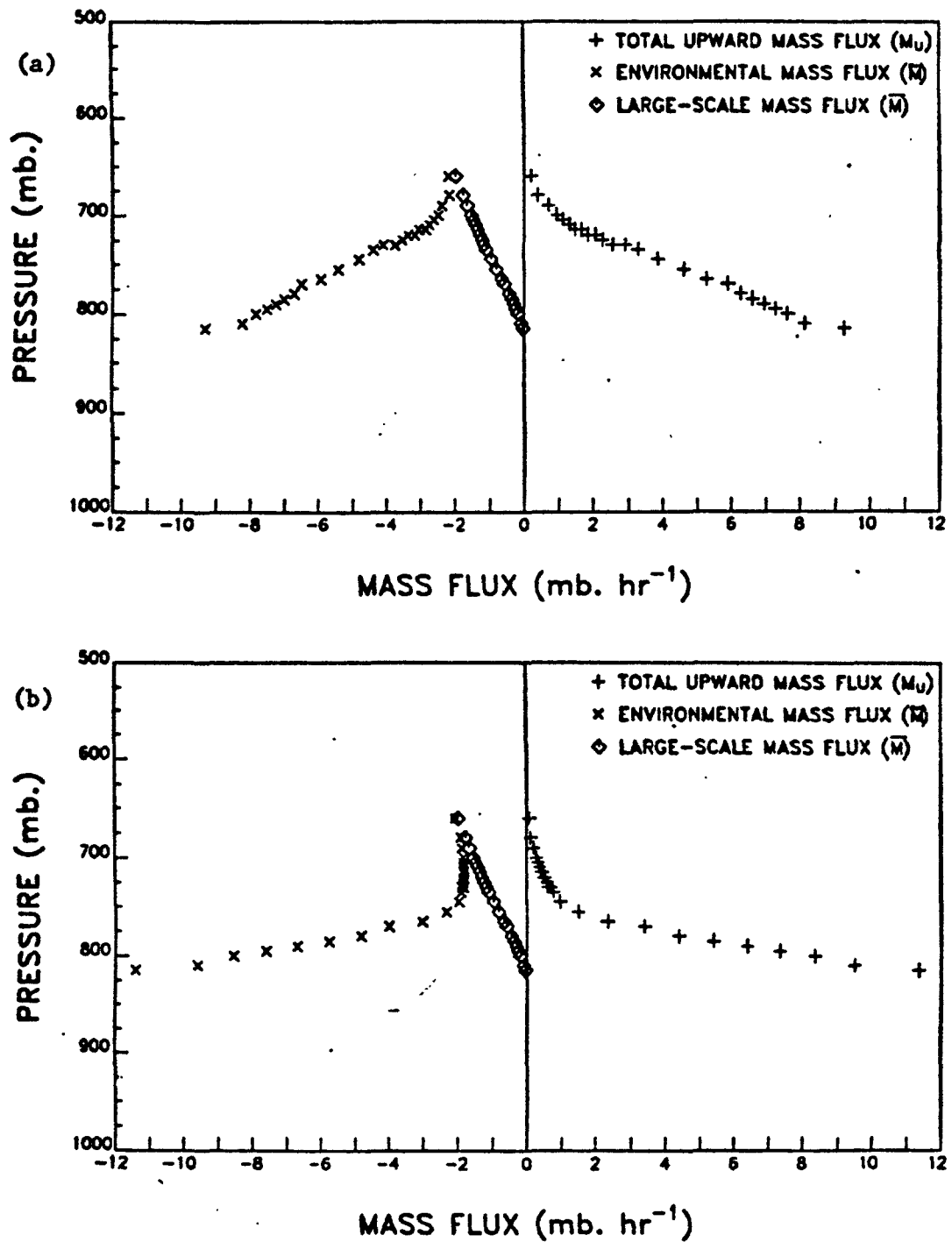


Figure 3-4. Vertical mass flux distribution for  
(a) explicit model, and (b) implicit  
model at 20Z (case #1).

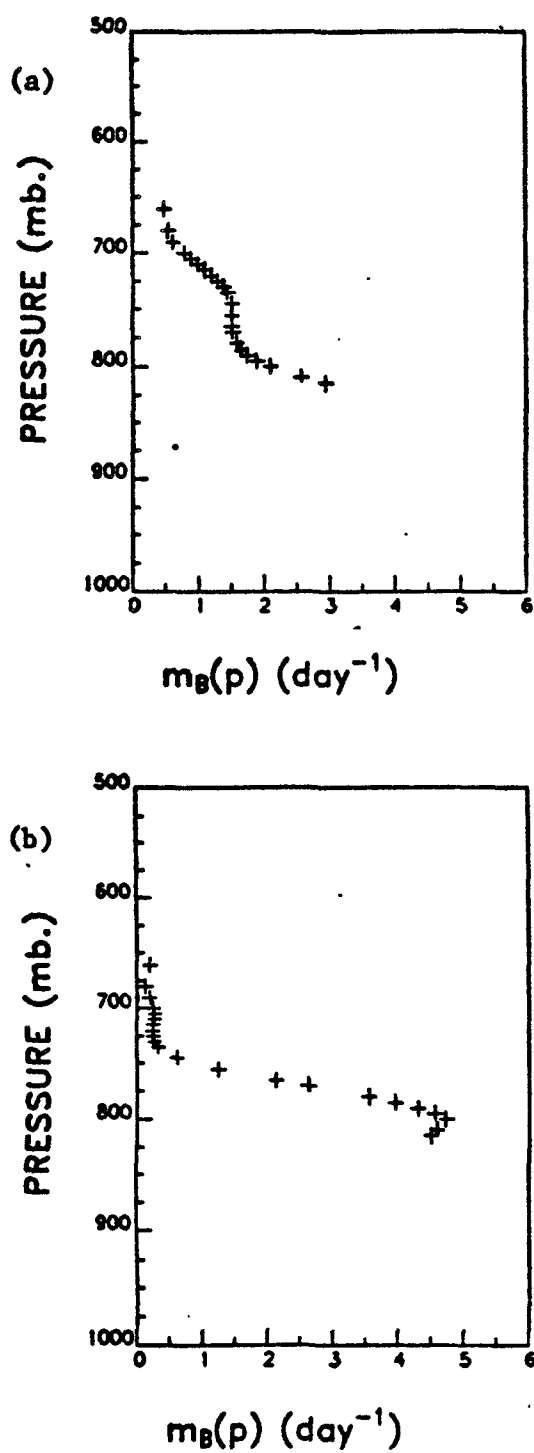


Figure 3-5. Cloud-base mass flux distribution  $m_B(p)$  for (a) explicit model, and (b) implicit model at 20Z (case #1).

detrain at a level  $p$  such that  $p + dp > p > p - dp$ . Therefore, from this graph, we are able to visualize the relative contribution to the total cloud-base mass flux from cloud classes that detrain at the various levels. From Figure 3-5(a) we see a feature between 775 and 700 mb that seems to correspond to the feature found at the same level in the fractional cumulus coverage shown in Figure 3-1(a). This is to be expected since the forcing functions used for the explicit model, derived in Section 2.5, are based on cumulus coverage. The implicit model, on the other hand, shows a sharp decrease in the mass flux contribution for clouds whose detrainment levels are between 800-735 mb, while the contribution from clouds whose tops are above 735 mb is relatively constant. The sharp decrease below 800 mb is dubious for several reasons: (1) the sensitivity of the solution of Equation (81) to  $d\lambda_D/dp$  in the region of the detrainment levels for the lowest few cloud classes; (2) the sensitivity of  $m_B(p)$  to  $d\lambda_D/dp$  (via Equation 83); and (3) the lack of spatial variability in the forcing functions for shallow clouds which would allow for boundary layer influences. The effects of (1) and (2) counteract each other since a variation of  $d\lambda_D/dp$  has opposite influences on the magnitudes of  $m_B(\lambda)$  (via Equation 81) and  $m_B(p)$  (via Equation 83) although the effect of  $d\lambda_D/dp$  on  $m_B(\lambda)$  near cloud base may be greater than linear, whereas the influence of  $d\lambda_D/dp$  on  $m_B(p)$  is linear at all levels.

Figure 3-6 shows the important result of cloud venting. In this process, air of mixed-layer origin is vented from the mixed layer and is subsequently deposited, or detrained, into the cloud layer. An increase in the cloud-layer concentration of the pollutant therefore ensues. For the purposes of these calculations a nonreactive pollu-



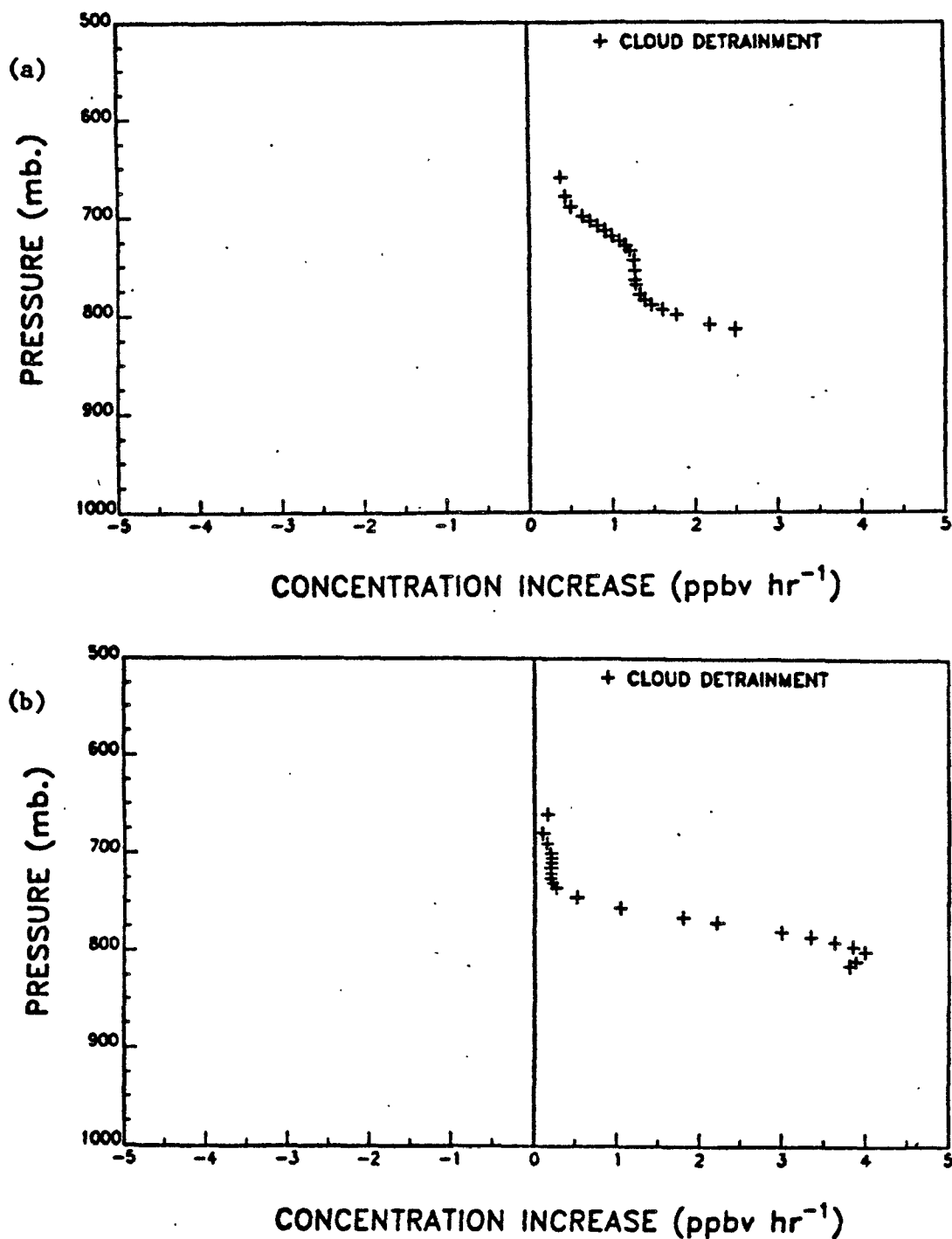


Figure 3-6. Concentration increase in the cloud layer of a conservative tracer assuming a mixing ratio of 60 ppbv in the mixed layer and 40 ppbv in the cloud layer for (a) explicit model, and (b) implicit model at 20Z (case #1).

tant tracer is assumed that experiences no production or loss during the transport. The detrainment of the tracer into the cloud environment is given by,

$$D_{TR}(p) = \delta(p)[TR_u(\lambda, p) - \bar{TR}] \quad (84)$$

where  $\delta(p)$  is given by Equation (77) and the in-cloud tracer concentration (a function of cloud class and pressure) is determined from Equation (24) with  $TR_u$  substituted for  $h_u$ . A value of 60 ppbv is assumed for the concentration of the tracer in the subcloud layer, while 40 ppbv is assumed to be the cloud layer value.

Lenschow et al. (1981), inferred the in-situ production rate of ozone to be approximately 5 ppb  $hr^{-1}$  from an ozone budget analysis of the boundary layer. While theoretical studies (Fishman et al., 1979) give production rates of approximately  $2 \times 10^{-2}$  ppbv  $O_3$   $hr^{-1}$  for the free troposphere. Therefore, if we consider the conservative tracer to be ozone, the effects of cloud venting could be much more significant than in-situ production and cannot therefore be ignored in transport models that are applied to scenarios where convective venting is possible.

Figure 3-7 shows the vertical mass flux distribution for case #2. We see that the peak value is slightly lower than that for case #1, shown in Figure 3-4. From Table 3-1 we see that (1) the maximum height is 3100 m less than that in case #1 and (2), the total and cumulus cloud coverage is slightly larger than that for case #1, and (3) the updraft area for case #2 is only slightly less than that for case #1. Since from Equation (61) we see that, for the explicit model, the forcing is directly proportional to the calculated updraft

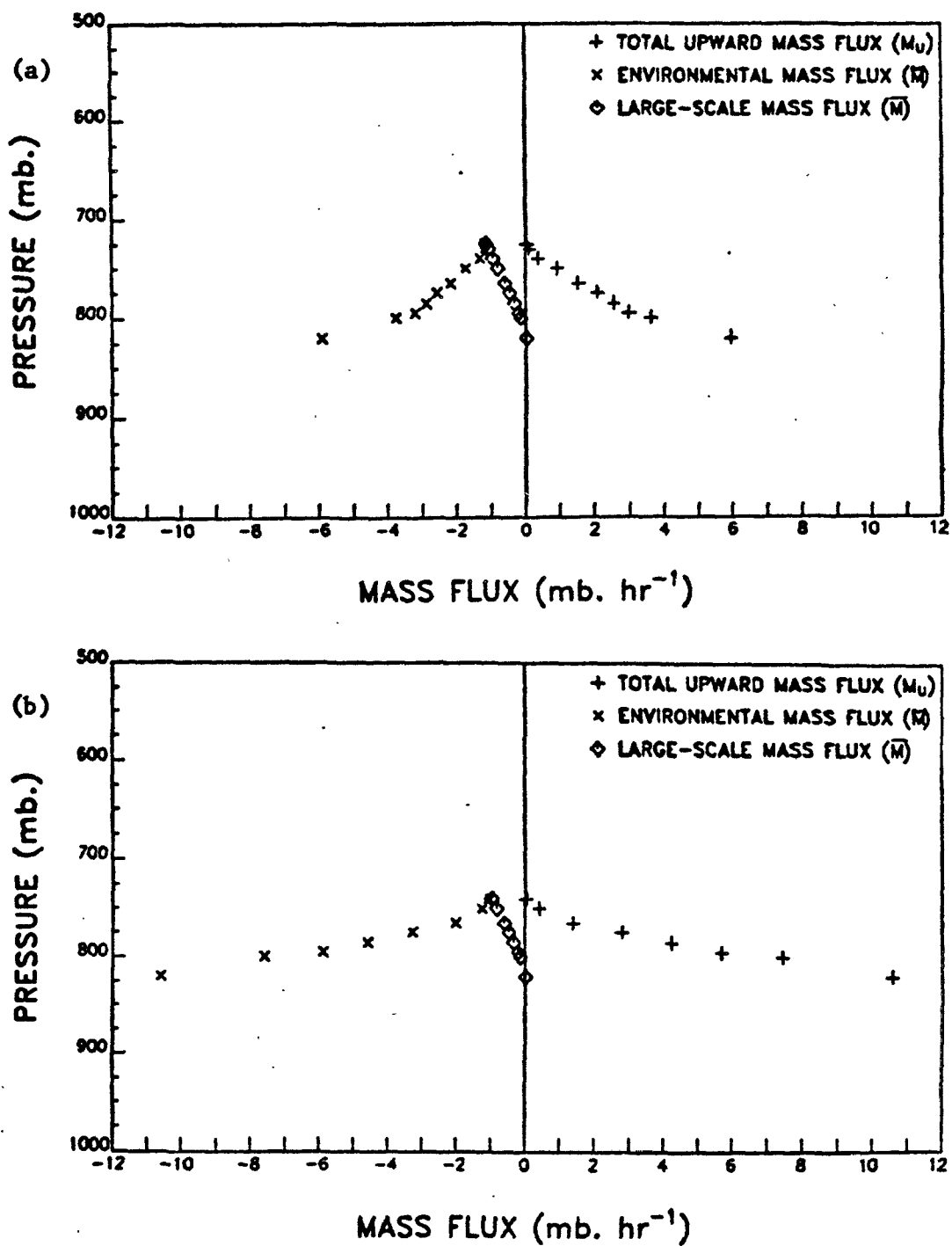


Figure 3-7. Vertical mass flux distribution for (a) explicit model, and (b) implicit model at 20Z (case #2).

area, we might not expect to see a great difference between the peak values of the vertical mass flux for these two cases for the explicit model. In fact, the results from the implicit model, whose forcing functions are calculated independently from those for the explicit model, show a similar reduction in the peak value of  $M_u$  from case #1 (Figure 3-4b) and case #2 (Figure 3-7b). Note also that the heat flux value for both the implicit and explicit models in case #2 show a decrease from that in case #1. This should be expected due to the decrease in the maximum cloud height and updraft area.

Figure 3-8 shows the cloud-base mass flux distribution for case #2. The maximum value in Figure 3-8(a) is only slightly smaller than that of case #1 due again to a smaller updraft area, which, for the explicit model, implies that the forcing would be smaller. The maximum value for the implicit model, shown in Figure 3-8(b), is also less than that in 3-5(b) due to less forcing from the observed synoptic-scale data. The sharp decrease below 800 mb in Figure 3-8(b) is similar to that in Figure 3-5(b), hence the previous discussion of this feature applies in this case as well.

The concentration increase of the tracer pollutant for case #2 is shown in Figure 3-9. We see that, as in the case of Figure 3-8, the maximum values for the explicit model are slightly less than those corresponding to case #1 since the cloud-top level detrainment is based on the cloud-base mass flux, which in Figure 3-8 has been shown to be slightly less than the corresponding values for case #1. In the same manner, the concentration increase for Figure 3-9(b) (implicit) is less than that for case #1 since the forcing from the synoptic-scale is less.

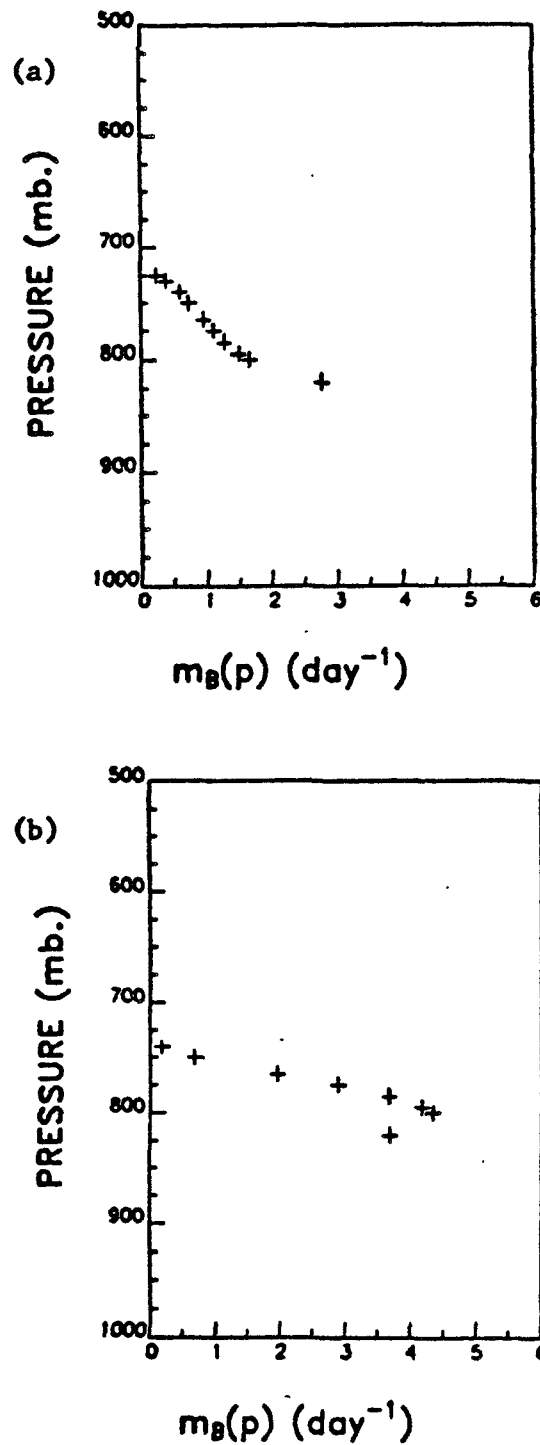


Figure 3-8. Cloud-base mass flux distribution  $m_B(p)$  for (a) explicit model, and (b) implicit model at 20Z (case #2).

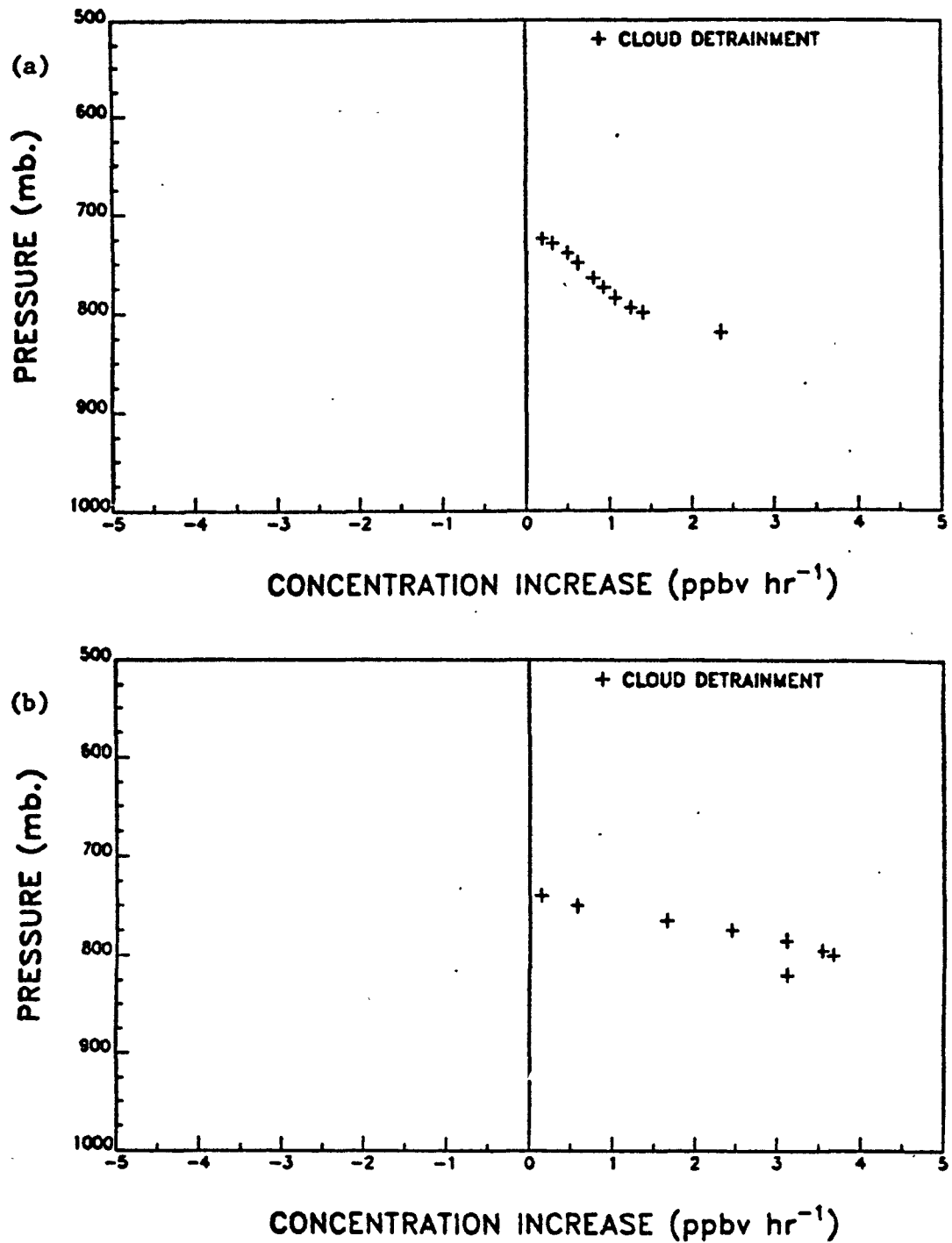


Figure 3-9. Concentration increase for the same conditions of Figure 3-6 for (a) explicit model, and (b) implicit model at 20Z (case #2).

Figure 3-10 shows the vertical mass flux distribution for case #3. We see from Table 3-1 that the cumulus cloud coverage, maximum cloud-top height, updraft area and heat flux (for both the implicit and explicit models) is the least of all three cases, hence it is not surprising that  $M_u$ , calculated from both the implicit and explicit methods, is also the least of all three cases. An interesting feature is shown in Figure 3-10(b) in that the vertical updraft mass flux increases slightly in magnitude from 830-810 mb in the implicit model. From the meaning of  $M_u$  (Equation 82) one would expect that  $M_u$  would always increase with increasing pressure. However, if the contribution to the updraft mass flux for clouds with detrainment levels below a certain pressure is small, then the total upward mass flux ( $M_u$ ) in this region will vary according to  $\eta(\lambda, p)$ , which is given by Equation (20). This however, is an explanation of how the model has treated the given input data. The question of whether or not the forcing functions, as determined from the input data, have adequately accounted for all of the physical processes influencing the cloud field at this shallow level remains unanswered and will be the subject of a future work.

In comparing the results of Figure 3-11 with those of Figure 3-8 (for case #2) and Figure 3-5 (for case #1) we see that as in the case of determining  $M_u$  for case #3 (Figure 3-10) the values of  $m_B(p)$  shown in Figure 3-11 are the least of all three cases. The sharp decrease in  $m_B(p)$  below the maximum value in Figure 3-11(b) for the implicit model is more striking than the corresponding decreases in Figures 3-5(b) and 3-8(b) and is a result of much lower values for the synoptic-scale forcing at this location. As previously mentioned,

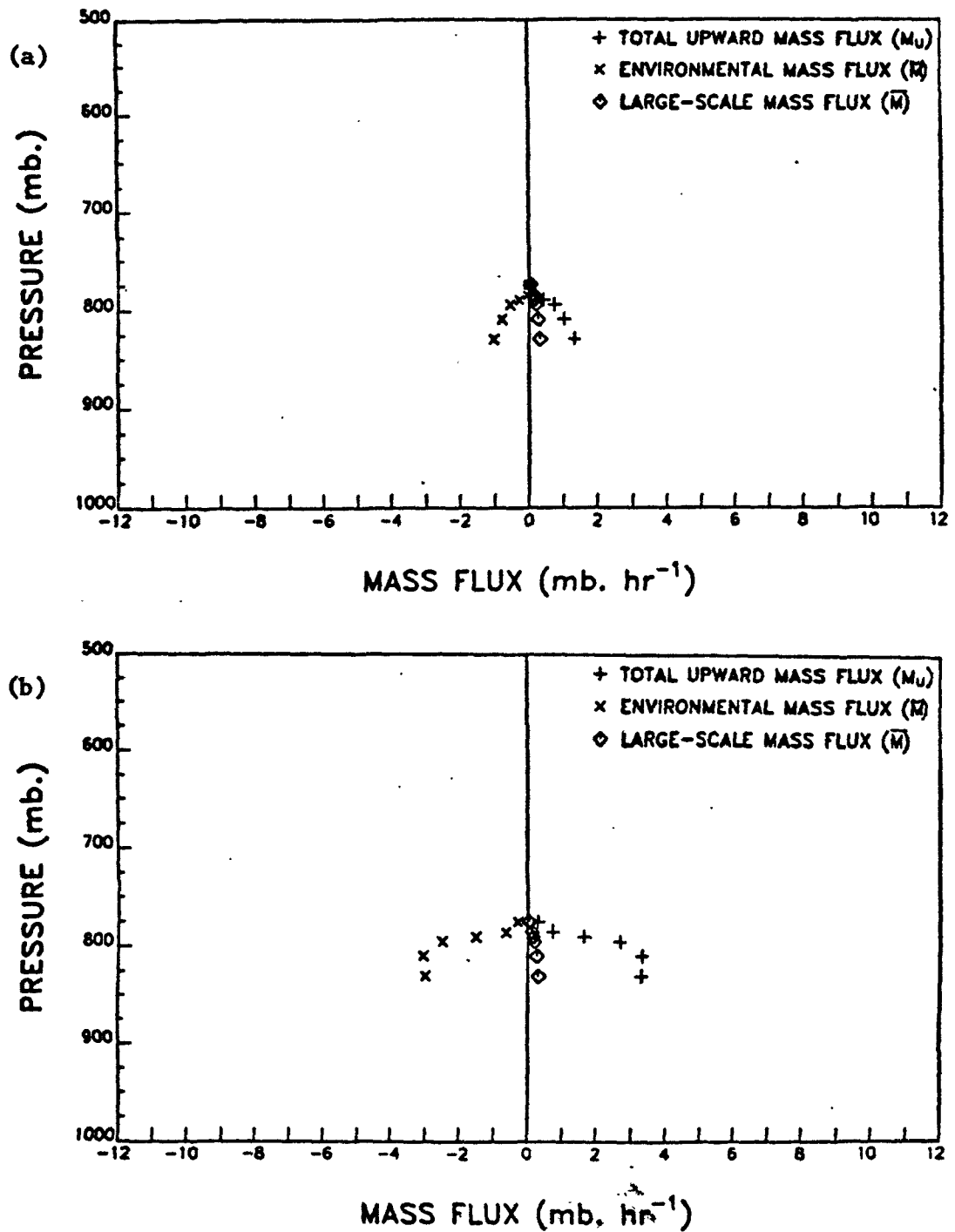


Figure 3-10. Vertical mass flux distribution for (a) explicit model, and (b) implicit model at 20Z (case #3).



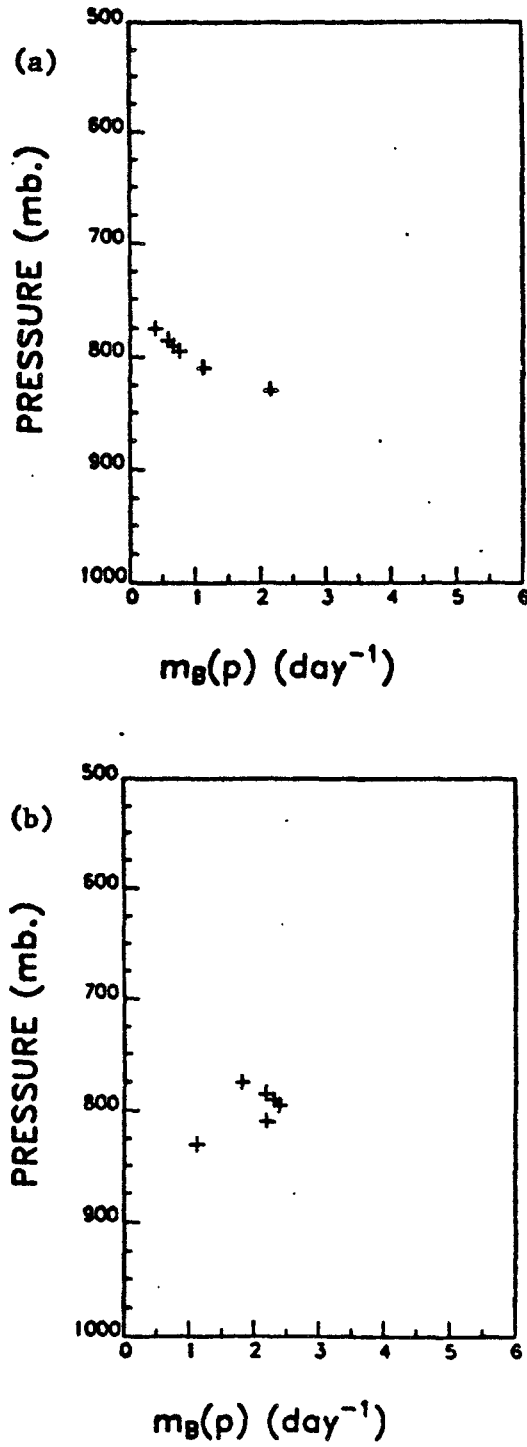


Figure 3-11. Cloud-base mass flux distribution  $m_B(p)$  for (a) explicit model, and (b) implicit model at 20Z (case #3).

the forcing functions for the implicit model at this level of the cloud depth are somewhat dubious. The results from the explicit model (Figure 3-11a) however, indicate the same close relationship to the cloud cover distribution as seen for cases #1 and #2.

Figure 3-12 shows the concentration increase ( $\text{ppbv hr}^{-1}$ ) as a function of pressure over the depth of the cumulus cloud field for case #3 (weak convection). We again see that the greatest concentration increase for the explicit model (Figure 3-12a) is associated with the shallowest clouds and decreases with decreasing pressure in proportion to the decrease in cumulus cloud cover shown in Figure 3-12(b). The now familiar feature of a sharp decrease just below the maximum value is again evident, resulting from the previously mentioned ambiguities in the  $d\lambda_D/dp$  profile and the forcing functions at these levels.

From the Figures 3-5, 3-8 and 3-11 we see that the value of  $d\lambda_D/dp$  at lower levels can have a substantial influence on the resulting values of  $m_p(p)$  and hence the detrainment values. This implies that a careful selection of  $\lambda$  is required. However, the values of  $\lambda$  for at least the shallowest clouds may be difficult to determine accurately since 1.) the profile of temperature and moisture are spatially interpolated from rawinsonde data and hence do not reflect the influence that cumulus clouds have had on the environment between observations, and 2.) the entraining plume model for shallow clouds may not be adequate since it only allows detrainment at the cloud top. In regards to the first point, progress may be made if it is accepted that the correlations between Figures 3-1(a) and (b), 3-2(a) and (b), and 3-3(a) and (b) mentioned earlier are more than fortuitous, in which case, a

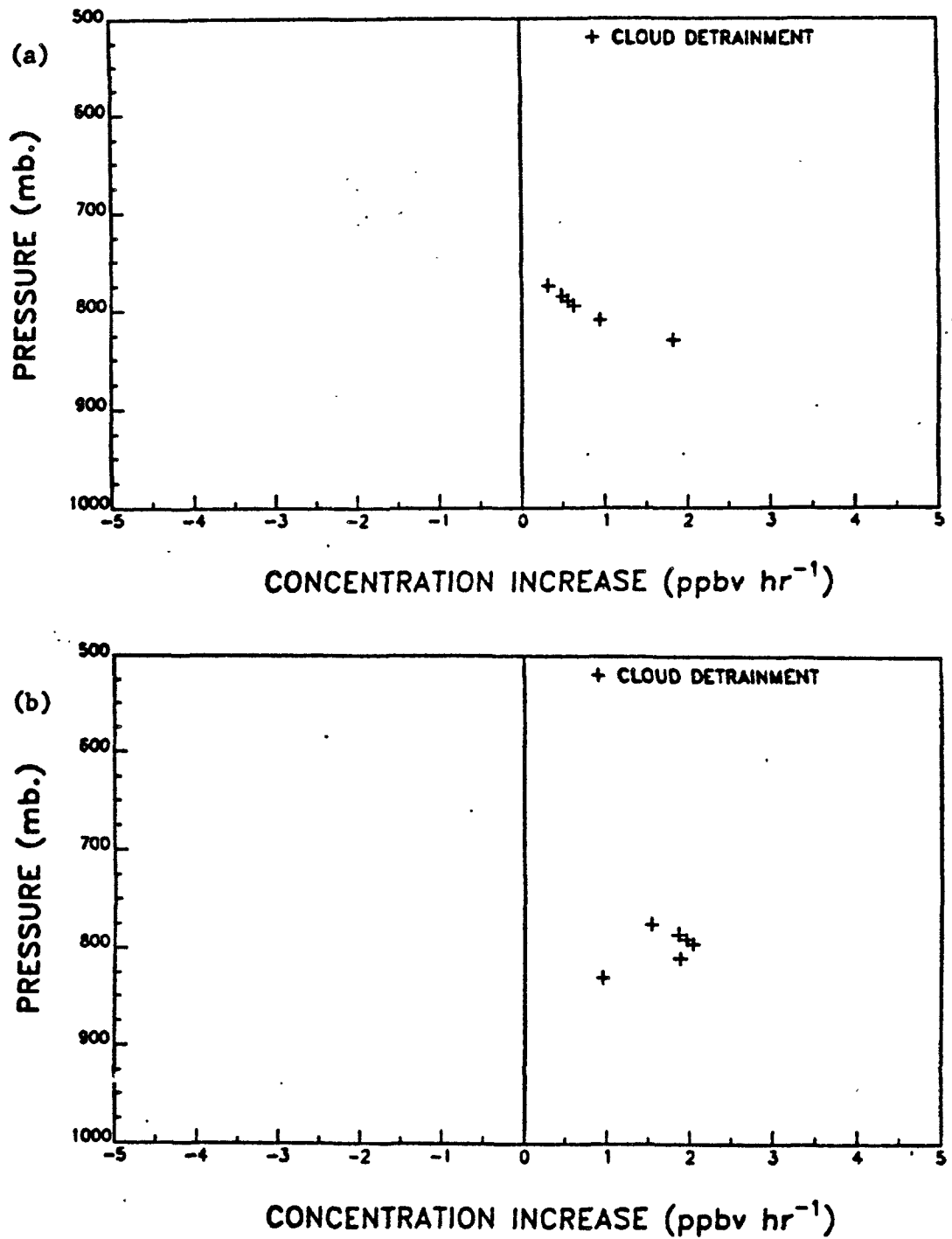


Figure 3-12. Concentration increase for the same conditions of Figure 3-6 for (a) explicit model, and (b) implicit model at 20Z (case #3).

future work may try to employ the profile of cumulus cloud cover in determining the various  $\lambda_1$  and hence  $d\lambda_D/dp$ . Such an advance would greatly enhance the ability of either the explicit or implicit model to reflect subgrid-scale variations. The problem raised by the second point above problem may be alleviated somewhat by incorporating side detrainment into the calculations at least for shallow clouds.

Johnson (1977) estimated that for the cases he studied, incorporating the affect of side detrainment into the calculations, reduced the overall mass flux by 15% - 20%, while shifting the cloud base mass flux distribution to give more influence to the taller clouds and less to the shallower ones. Since the inclusion of the process of side detrainment slightly increases the instability of the solution (Johnson, personal communication), it was decided that in order to adequately evaluate the model's performance, such instabilities should be avoided at this time. Hence, the inclusion of this process is left for a future task. Even if this factor was to be taken into account, we can see from Figures 3-6, 3-9 and 3-12 that a significant amount of pollutant can be vented from the boundary layer by convective clouds.

We have also seen that, especially for the implicit model in case #3, the large-scale forcing functions may not be adequate to determine the cloud field and its characteristics. This problem may be overcome, however, by determining an analogous 'Q' term for clouds due to boundary layer forcing and superimposing this onto the profile of  $Q_1 - Q_2 - Q_R$ . It should be noted at this point that although the forcing functions used in the implicit model are devoid of subsynoptic-scale influences, the final model results are not. As mentioned in the

discussion of Equation (34) the maximum observed cloud-top height for each grid cell is used to limit the maximum vertical extent attained by the model derived cloud field for that cell. In this way, sub-grid scale influences are introduced into the formulation of the implicit model. This variation can be seen from the results of the implicit model for the three cases considered in this chapter and is such that the total upward mass flux,  $M_u$ , is directly proportional to the vertical development of the cloud field.

The explicit model presented in this work, offers an additional degree of freedom over the implicit model in that for the hypothetical situation of 2 cases with equal vertical development, the larger value of  $M_u$  would be associated with the case having the larger computed updraft area. This additional degree of freedom may, however, be a mixed blessing since the manner in which the updraft area is calculated from the data of Deardorff et al. (1980) is not only a sensitive calculation, as the results of the next chapter will show, but it is at best a first approximation to a very complicated process. To think that the equation giving  $\sigma$  is universal in time and space may be naive. It is interesting to note that the calculated values of  $\sigma$  are well within the expected range of only a 'few' percent of the total area (Johnson, 1975; Zipser and LeMone, 1980). A further refinement of this parameterization may be possible as results from the BLX83 study (Stull, personal communication) become available.

As in the problems mentioned above, in regards to the implicit model, the inability of the rawinsonde data to resolve the effects that a convective cloud field has on the environmental temperature and moisture fields in both space and time may cause the calculated

value of  $\Gamma_c(\lambda_1)$  (Equation 59) to be inaccurate. This is because the temperature and moisture differences between the updraft and environment are used in the calculation of  $\Gamma_c(\lambda_1)$ . In addition, the methodology for determining the updraft temperature and moisture is determined from the entraining plume theory, which, as previously mentioned, may be inadequate for small clouds. Other uncertainties also exist. The equation for the half-life of each cloud class is highly empirical and if in error, it will probably give slightly high values. The assumption that the ratio of updraft area to total cumulus coverage is not a function of cloud class (Equation 54) may also place severe restrictions on the explicit model's ability to accurately simulate the physical process of cloud venting. However, until observational data can be obtained to either verify or refute this assumption, it is felt that it is a reasonable first approximation. An additional limitation of the explicit model is that caused by a high stratus or cirrus deck that may obscure any lower level convective clouds. As stated in Section 2.2c, if less than 70% of the existing cloud field was not cumulus, the frequency distribution of cloud top heights could not be obtained. However, for the situations on which the explicit formulation was tested in this study, it performed quite well.

In addition to the above mentioned problems, there is the concern that the grid area over which the variables are averaged (mentioned on page 78) may not be large enough to contain a statistically representative sample of the cumulus population. This would be most likely in cases where cumulonimbus clouds were present. However, with the availability of the cumulus cloud cover as a function of height, one can proceed in the following way: 1.) combine enough adjacent grid

cells so that the assumption of a representative sample is satisfied; 2.) do the calculations for this enlarged grid cell; 3.) using the cumulus cloud-cover distribution for each cell, within the enlarged cell, the fraction of the total mass flux from any one of the 'sub-cells' can then be determined using the cloud-cover distribution, since the cloud-base mass flux is given in terms of cloud classes which, in turn, are classified according to cloud-top height. Therefore, with the aid of the vertical distribution of cumulus coverage, the computations can include as many cells as necessary to satisfy the stated condition after which, the partitioning of the total cloud flux into each cell can be done.

In view of the ambiguities surrounding the determination of the updraft area for use in the explicit model, a direct and quantitative comparison between the absolute values obtained for the explicit and implicit models is not possible at this time. Although the shape of the mass flux profiles for the explicit model do tend to have a better intuitive feel about them, since they are related to the cloud cover distribution, a final judgement must be waived until the uncertainties mentioned above can be resolved from additional observational programs. The results shown here, however, do indicate a good degree of internal consistency within each model in that more mass flux is obtained for larger cloud fields in both models.

In spite of the uncertainties that do exist in regard to the models utilized in this study, the results shown here indicate that satellite data can be used to close the 'spectral gap' that is present when only rawinsonde data is used. The final results of any such model however, await an evaluation comparing the model results with observed data.

## CHAPTER 4

### SENSITIVITY ANALYSIS

The results of the two cloud venting models, tested on three case scenarios were discussed in the previous chapter. The sensitivity of these models to some of their input variables will be examined in this chapter. This will be accomplished by adjusting the normally assumed value of several parameters, whose specification appears to be the most critical to the model's operation. A comparison of the subsequent model results will then be made to those normally obtained.

The first parameter chosen is the lower limit of the integral in Equation (52) as it applies to the explicit model. This equation was used to obtain the fractional area coverage of updraft and is repeated here:

$$\sigma = P(Z_{LCL}) = \int_{Z_{LCL}}^{H_2} G(\xi) d\xi \quad (56)$$

As discussed in Section 2.5, the actual value of the lower limit used was set above the LCL since we were interested in the updraft area due to active clouds, instead of the sum of both active and forced clouds. However, the actual value of distance above the LCL chosen could not be explicitly calculated due to the lack of vertical resolution in the model and the lack of adequate boundary conditions. The value of 5 mb was chosen based on the assumptions that all



forced clouds would be contained within this distance from the cloud base and that the satellite data probably could not resolve clouds with a vertical extent any smaller than this so that the contribution of their updraft area to the total should be neglected.

Test runs of the model were done to see how sensitive the model calculations were to the actual determination of this value. The data in Table 4-1 shows how a change in the lower limit of integration of Equation (52) affects the determination of the fractional updraft area, heat flux and total upward mass flux ( $M_u$ ).

Table 4-1

integration limit mb. above LCL	fractional updraft area	total cloud-base heat flux $W\ m^{-2}$	$M_u$ mb. $hr^{-1}$
0.0	.2288	849.	33.7
5.0	.0671	249.	9.9
10.0	.0120	45.	1.8

Table 4-1. Sensitivity analysis of the explicit model to the selection of the lower limit of integration in Equation (52).

It is therefore evident that the operation of the explicit model is very sensitive to the specifications of the lower limit. Such a sensitivity may pose a severe limitation as to the applicability of this model in an operational sense.

Another parameter pertaining to the explicit model that was chosen for analysis was the parameter TMN involved in the calculation of the cloud's half-life appearing in Equation (60). This parameter gives an

approximate minimum bound for the calculation (depending on the environmental conditions) the value of which was adjusted from 15 to 10 min for the purposes of this analysis. Table 4-2 shows the results of the explicit model for this test case.

Table 4-2

LMN min	total cloud-base heat flux $\text{W m}^{-2}$	$M_u$ mb. $\text{hr}^{-1}$
15	249.	9.9
10	285.	11.3

Table 4-2. Sensitivity analysis of the explicit model to the selection of the approximate minimum bound for the determination of cloud half-lives.

As shown in Table 4-2, the results of the explicit model are not highly sensitive to the value of LMN in that a decrease of LMN of 33% resulted in an increase of only ~14% for  $M_u$ . An increase in  $M_u$  for a decrease in LMN should be expected since this implies a faster generation rate for the clouds, hence more mass will be vented from the subcloud layer in a given time.

Table 4-3 illustrates the sensitivity of the explicit model to a variation in  $\Delta H/Z_1$ . The results of this analysis indicate that for a constant  $Z_1$ , as  $\Delta H$  decreases (increases),  $M_u$  decreases (increases). For a 20% reduction in  $\Delta H/Z_1$ , from a mid-range value of 0.25,  $M_u$  decreases by 29%; whereas a 20% increase in  $\Delta H/Z_1$  results in a 24% increase in  $M_u$ . This is within acceptable limits. The data from Tables 4-1 and 4-3 therefore indicate that the explicit model is much

more sensitive to the selection of the lower limit of integration for Equation (52) than to the depth of  $\Delta H$ .

Table 4-3

$\Delta H/Z_1$	fractional updraft area	Total cloud-base heat flux	$M_u$ mb hr <sup>-1</sup>
0.20	.0536	199.	7.89
0.25	.0753	279.	11.09
0.30	.0931	346.	13.72

Table 4-3. Sensitivity analysis of the explicit model to the selection of  $\Delta H/Z_1$ .

The final parameter tested that is strictly applicable to the explicit model was the cloud cover distribution used to determine the cloud forcing functions. It was found that an increase of 10% in the cloud cover distribution at all levels produced an increase in  $M_u$  of 10%. This is to be expected since the cloud forcing for the explicit model is directly proportional to the fractional cloud cover as shown in Equation (61).

The sensitivity of the results from the implicit model to errors in the rawinsonde data was explored. The test was accomplished by shifting the rawinsonde data observed for a station within the study area by -10 mb at all levels. Although this created a large perturbation on the system, the gridding procedures used in this work, which have been described in Section 2.2, were quite effective in smoothing the field. The resulting value of  $M_u$  from this test was only ~37% less than that obtained in an unperturbed state. This is an extremely moderate change in  $M_u$  in view of the large perturbation that

was placed on the system. The results of this test would seem to indicate that the effects of small errors present in the rawinsonde data would be minimized as a result of the data preparation techniques employed in this study.

Table 4-4 presents the results of altering the vertical profile of several parameters important to the implicit model by the amount indicated. The data for the unperturbed or standard case are taken from a randomly chosen cell in the domain.

Table 4-4

variable	% altered	$M_u^{-1}$ mb hr <sup>-1</sup> (standard)	$M_u^{-1}$ mb hr <sup>-1</sup> (perturbed)	% change in $M_u$
$Q_R$	-10%	9.425	9.293	-1.4
$Q_1$	10%	9.425	9.588	1.7
$Q_2$	10%	9.425	10.073	6.9
$d\lambda_D/dp$	10%	9.425	8.449	10.4
$q_L$	10%	9.425	9.655	2.4

Table 4-4. Sensitivity analysis of the implicit model to the profiles of  $Q_R$ ,  $Q_1$ ,  $Q_2$ ,  $d\lambda_D/dp$  and  $q_L$ .

Of the parameters tested, Table 4-4 shows that the operation of the model is most sensitive to the profile of  $d\lambda_D/dp$ . This sensitivity was also mentioned in Chapter 3 in regard to the determination of the cloud-top detrainment of a conservative tracer. Due to these analyses, care should therefore be taken when determining  $d\lambda_D/dp$  so that a smooth profile is obtained. Table 4-4 shows that the next most sensitive parameter in the calculation is the determination of  $Q_2$ , which was defined in Section 2.4 to be the 'apparent moisture sink' of moisture from the large scale due to cumulus clouds.

However, the relative sensitivities of  $Q_2$ ,  $Q_1$  and  $Q_R$  shown in Table 4-4 are actually only valid for the environmental conditions existing at the time and location for which the model was run and should not, therefore be taken to be universal. The larger sensitivity to  $Q_2$  should therefore be interpreted to mean that for this particular location,  $Q_2$  dominated  $Q_1$  and  $Q_R$  as a cloud forcing term. The remaining parameter mentioned in Table 4-4 is the liquid-water mixing ratio  $q_l$ . Although  $q_l$  is important in determining cloud-top height of a given cloud class (Johnson, 1975), the model's operation is apparently more sensitive to other parameters.

A budget analysis showing the relative magnitude of the terms comprising  $Q_1$  and  $Q_2$  given by Equations (41) and (42) respectively, is presented in Table 4-5. By examining this budget equation we may be able to determine which, if any terms could be neglected.

Table 4-5

mb	$\frac{\partial s}{\partial t}$	$s(\nabla \cdot \underline{V})$	$\underline{V} \cdot \nabla s$	$\frac{s \partial \omega}{\partial p}$	$\frac{\omega \partial s}{\partial p}$	$\frac{\partial q}{\partial t}$	$q(\nabla \cdot \underline{V})$	$\underline{V} \cdot \nabla q$	$\frac{q \partial \omega}{\partial p}$	$\frac{\omega \partial q}{\partial p}$
700	-0.68	87.62	0.85	-89.71	-2.36	5.59	-2.92	-7.11	2.97	-3.82
800	-1.71	98.53	3.27	-80.90	-0.25	-2.63	-6.13	-7.58	5.05	0.16

Table 4-5. A budget analysis for the terms comprising  $Q_1$  and  $Q_2$  as given by Equations (41) and (42) respectively. The data are taken from that of case #1 at 700 and 800 mb. Units:  $^{\circ}\text{K day}^{-1}$ .

In order to obtain the large-scale forcing, as given in Equation (43), we subtract  $Q_2$  from  $Q_1$ . As evidenced by the 700 mb data in Table 4-5, the result would be a small difference between two large numbers, with the difference of 1.01 being on the order of the smallest entry in

Table 4-5 for that level. This would be an unsatisfactory situation if it were not for the fact that the two terms with the largest magnitudes (opposite in sign) are related by the continuity equation

$$\nabla_h \cdot \underline{V} + \frac{\partial \omega}{\partial p} = 0 \quad (12)$$

such that the magnitude of one term influences the magnitude of the other. The data from Table 4-5 indicate that  $Q_1 - Q_2$  for 800 mb is much larger than that for the 700 mb level. However, in view of the small values of  $Q_1 - Q_2$  near the top of the cloud field, it is suggested that none of the terms in the above budget analysis be neglected.

Another observation that should be made at this point is the importance of the term  $s\partial\omega/\partial p$  in determining the value of  $Q_1$ . Since the dry static energy ( $s$ ) is a large number ( $\sim 300$ ), care must be taken to obtain a smooth profile of  $\partial\omega/\partial p$ , otherwise erratic values of  $Q_1$  will result.

As mentioned in Section 2.2a, the values for  $\partial s/\partial t$  and  $\partial q/\partial t$  were the result of a linear interpolation in time. In view of the fact that the magnitude of these terms can at times be comparable to the total forcing ( $Q_1 - Q_2 - Q_R$ ), future research efforts may need to incorporate a more accurate determination of these local time derivatives.

Johnson (1975) found that radiative cooling played a larger role in accurately determining flux quantities in the tropics than in the sub-tropics. However, for the scenarios studied in this work, the convective activity was much less than that observed in Johnson's (1975) sub-tropical case study. As a result, there were many instances

where the role of radiative cooling could not be considered to be insignificant, especially for shallow cloud fields. In such instances the profile of radiative cooling rates used in this work is admittedly a crude approximation. Pollutant mass flux computations in these cases may be in error by a factor of 2-3. Future research efforts focusing on scenarios with similar convective patterns as those examined in this work should involve a determination of the radiative cooling profile that is influenced by the existing cloud cover.

The sensitivity of the explicit and implicit models to various parameters has been discussed in this chapter. It was determined that the explicit model, as it is presently configured, is probably too sensitive to its input parameters to be employed as an operational model. The sensitivity of the implicit model to its various input parameters however, does seem to be acceptable if care is exercised in determining the gridded fields required as input and in determining the vertical derivatives of  $\lambda$  and  $\omega$ . More sophisticated methods of determining the local time derivatives of the dry static energy and specific humidity should be explored in future works, as well as efficient methods for determining radiative cooling rates based on observed cloud cover instead of using a universal profile.

## CHAPTER 5

### SUMMARY AND CONCLUSIONS

Two models have been described that present a formalism for assessing the role that a convective cloud field has on the vertical redistribution of pollutant species vented from the boundary layer. The first model, adapted from Johnson (1975), implicitly assumes the existence of a cloud field if the atmosphere is conditionally unstable and derives the forcing functions for the cloud field solely from synoptic-scale rawinsonde data and tabulated radiational cooling data. This model has been labeled the 'implicit' approach in this work. The second model uses the vertical distribution of cumulus cloud cover, as determined from satellite data, to determine the cloud forcing functions, thereby explicitly incorporating features of the existing cloud field into the model calculations in a dynamic way. This model has therefore been labeled the 'explicit' approach in this work. Both models assume that the cloud field can be partitioned into cloud classes based on cloud-top height and that each cloud class can be appropriately described by a characteristic updraft uniquely identified by an entrainment rate. It was also assumed that the model of an entraining plume was able to adequately depict the updraft characteristics of each cloud class. The cloud-base mass flux for each cloud class was then determined by solving a Volterra integral equation which connects the convective-scale



fluxes for each cloud class with the large-scale forcing function profile that is provided. Therefore, the two models described and evaluated in this report differ only in the manner in which the cloud forcing functions were derived. The major accomplishments and problems encountered in this work will now be discussed, as well as a view towards future research needs.

Prior to this work there had been no model available to determine the vertical redistribution of a pollutant tracer due to cumulus convection for use in an operational regional-scale model. This work presents a formalism for providing two such models. This formalism, embodied in the explicit and implicit approaches, can be seen as a tool which has led to a better understanding of the complex problem of cloud venting. Especially helpful was the use of satellite data in the depiction of subsynoptic scale phenomena and how this phenomena influences cloud-base pollutant flux calculations as determined by the explicit model which is unique to this study. The subsynoptic scale phenomena, which was not incorporated in the forcing functions for the implicit model, appeared to be reflected in the more realistic shape of the cloud-top detrainment profiles, shown in Chapter 3, for the explicit model, since the cloud forcing was assumed to be proportional to the cumulus cloud cover. However, the actual amount of pollutant detrained from the clouds was difficult to obtain with any certainty due to the sensitivities involved. The implicit model on the other hand, appeared to be much more reliable than the explicit model and may contain the flexibility needed to incorporate subsynoptic-scale influences into its formalism as part of future research efforts.

The results of the sensitivity analysis presented in Chapter 4 of this work indicated that the operational use of the explicit model proposed in this work is dependent on future research efforts in at least three areas. First, further study on the concept of an entrainment zone to see how the distribution function given in Equation (53) varies in space and time is needed. The effects of the stability of the overlying layer on this distribution function for various conditions also needs to be determined more precisely. Secondly, more observations on the life-time of cumulus clouds, especially in relationship to the rate of entrainment and the environmental moisture content need to be made. Finally, observations of the ratio of updraft area to total cumulus area need to be made for varying cloud sizes and for various times in their life cycle.

It was indicated by the results shown in Chapter 3 that the contribution of the cloud-base mass flux due to shallow clouds may be over-estimated as a result of the assumption that clouds detrain only at their cloud tops. This follows directly from the entraining plume theory. A better depiction of the cloud-base mass flux may be obtained in future works by incorporating side detrainment at least for the shallower clouds. It has also been suggested in Chapter 3 that the profile of fractional cumulus coverage may be able to be used to determine  $d\lambda_D/dp$  and hence invoke a stronger influence of subsynoptic scale effects, via satellite data, on the results of either model.

Although the two models considered in this report differ in the manner in which they determine the cloud scale forcing, both rely on temperature and moisture data that has been interpolated spatially and temporally from rawinsonde data. This implies that the effects

that the cumulus cloud field has had on the environment between observations (in both a spatial and temporal sense) is implicitly neglected in the computations. Future works along this line may need to incorporate actual temperature and moisture profiles as determined from satellite observations.

In spite of the abovementioned areas that need future research, this study has provided two methods by which satellite data can be used to incorporate the subscale effects of cumulus clouds into regional-scale transport models. In what has been called the implicit approach, the vertical cloud development is limited by the satellite observed value, but the cloud forcing is determined solely from synoptic-scale rawinsonde data. In the second, or explicit approach, the vertical development is similarly limited, but the satellite data is dynamically incorporated into the determination of the cloud forcing functions. The two models give internally consistent results for varying conditions and give similar results for the total convective upward mass flux ( $M_u$ ). The manner in which the upward mass flux is apportioned to the various cloud classes, however, differs for the two models and is shown to affect the vertical profile of detrainment for a conservative tracer. This is seen as a consequence of the vertical profile of forcing functions used in the respective models. For the examples shown in this study, the explicit model gave more reasonable looking profiles since the forcing functions were related to the observed profile of cumulus cloud cover. The close agreement mentioned above for the calculated  $M_u$  values between the two approaches must, however, be viewed with caution. Until further observational data are made available, which will enable the uncertainties inherent in

this approach to be better known, the sensitivity of this model to its required input may preclude it from being used in an operational manner. It has also been shown that regardless of the method chosen, the concentration increase in the cloud-layer due to the venting action of cumulus clouds can be as, if not more important than the in-situ production of some species and should therefore not be neglected in regional-scale transport models for scenerios involving convective cloud fields.

## BIBLIOGRAPHY

## BIBLIOGRAPHY

- Arakawa, A. and Schubert, W. H., Interaction of a cumulus cloud ensemble with the large-scale environment, Part I, J. Atmos. Sci., 31, 674-701, 1974
- Baboolal, L. B., Pruppacher, H. R. and Topalian, J. H., A sensitivity study of a theoretical model of SO<sub>2</sub> scavenging by water drops in air, J. Atmos. Sci., 38, 856-870, 1981
- Barnes, S. L., A technique for maximizing details in numerical weather map analysis, J. Appl. Meteor., 3, 396-409, 1964
- Barnes, S. L., Mesoscale objective map analysis using weighted time-series observations, NOAA Technical Memorandum ERL NSSL-62, 1973
- Bates, J. R., Tropical disturbances and the general circulation, J. R. Met. Soc., 98, 1-16, 1972
- J. L., Vonder Haar, T. H. and Laybe, P., Determination for cloud parameters for NEROS II from digital satellite data, Draft Report EPA Contract No. 68-02-3731, 1983
- Bellamy, J. C., Objective calculations of divergence, vertical velocity and vorticity, Bull. Am. Met. Soc., 30, 45-49, 1949
- Betts, A. K., A composite mesoscale cumulonimbus budget, J. Atmos. Sci., 30, 597-610, 1973a
- Betts, A. K., Non-precipitating cumulus convection and its parameterization, Quart. J. R. Met. Soc., 99, 178-196, 1973b
- Betts, A. K., Modeling subcloud layer structure and interaction with a shallow cumulus layer, J. Atmos. Sci., 33, 2363-2382, 1976
- Bjerknes, J., Saturated-adiabatic ascent of air through dry-adiabatically descending environment, Quart. J. R. Met. Soc., 64, 325-330, 1938
- Browell, E. V., Carter, A. F., Shipley, S. T., Allen, R. J., Butler, C. F., Mayo, M. N., Siviter, J. H., Jr. and Hall, W. M., NASA multi-purpose airborne DIAL system and measurements of ozone and aerosol profiles, Appl. Optics, 22, 522-534, 1983

Bullock, O. R., Spatial and temporal interpolation of NEROS radiosonde winds, U. S. Environmental Protection Agency Technical Report, Research Triangle Park, N. C., 1983

Carson, D. J., The development of a dry inversion-capped convectively unstable boundary, Quart. J. R. Met. Soc., 99, 450-467, 1973

Chameides, W. L. and Stedman, D. H., Tropospheric ozone: coupling transport and photochemistry, J. Geophys. Res., 82, 1787-1794, 1977

Charney, J. G. and Eliassen, A., On the growth of the hurricane depression, J. Atmos. Sci., 21, 68-75, 1964

Chatfield, R. B., 1982, Remote tropospheric sulfur-dioxide: Cloud transport of reactive sulfur emissions, Ph.D. thesis, Colorado State University, 227 p.

Chen, C-H. and Orville, H. D., Effects of mesoscale convergence on cloud convection, J. Appl. Meteor., 19, 256-274, 1980

Cho, H-R. and Ogura, Y., A relationship between cloud activity and the low-level convergence as observed in Reed-Recker's composite easterly waves, J. Atmos. Sci., 31, 2058-2065, 1974

Clarke, J. F., Ching, J. K. S., Clark, T. L. and Posseil, N. C., Regional-scale pollutant studies in the northeastern United States, Atmos. Environment, 1983 (in press)

Cressman, G. P., The influence of the field of horizontal divergence on convective cloudiness, J. Meteor., 3, 83-88, 1946

Deardorff, J. W., Comments "On the interaction between the subcloud and cloud layers in tropical regions", J. Atmos. Sci., 32, 2363-2364, 1975

Deardorff, J. W., Willis, G. E. and Stockton, B. H., Laboratory studies of the entrainment zone of a convectively mixed layer, J. Fluid Mech., 100, 41-64, 1980

Dopplick, T. G., Global radiative heating of the earth's atmosphere, Ref. No. 24, Planetary Circulations Project, Dept. of Meteorology, Massachusetts Institute of Technology, 128 p.

Eliassen, A., Hov, O., Isaksen, I. S. A., Saltbones, J. and Stordal, F., A Lagrangian long-range transport model with atmospheric boundary layer chemistry, J. Appl. Meteor., 21, 1645-1661, 1982

Emmitt, G. D., Tropical cumulus interaction with and modification of the subcloud region, J. Atmos. Sci., 35, 1485-1502, 1978

Endlich, R. M. and Clark, J. R., Objective computation of some meteorological quantities, J. Appl. Meteor., 2, 66-81, 1963

Fishman, J., Solomon, S. and Crutzen, P., Observational and theoretical evidence in support of a significant in-situ photochemical source of tropospheric ozone, Tellus, 31, 432-446, 1979

Fraederich, K., A mass budget of an ensemble of transient cumulus clouds determined from direct cloud observations, J. Atmos. Sci., 33, 262-268, 1976

Fritsch, J. M. and Maddox, R. A., Convectively driven mesoscale weather systems aloft. Part I: Observations, J. Appl. Meteor., 20, 9-19, 1981a

Fritsch, J. M. and Maddox, R. A., Convectively driven mesoscale weather systems aloft. Part II: Numerical simulations, J. Appl. Meteor., 20, 20-26, 1981b

Gidel, L. T., Cumulus cloud transport of transient tracers, J. Geophys. Res., 88, 6587-6599, 1983

Greenhut, G. K., Ching, J. K. S., Pearson, R., Jr. and Repoff, T. P., Transport of ozone by turbulence and clouds in an urban boundary layer, Submitted to J. Geophys. Res., 1983

Johnson, R. H., 1975, The role of convective-scale precipitation downdrafts in cumulus-synoptic-scale interactions, Ph.D. thesis, University of Washington, 136 p.

Johnson, R. H., The role of convective-scale precipitation downdrafts in cumulus and synoptic-scale interactions, J. Atmos. Sci., 33, 1890-1910, 1976

Johnson, R. H., The effects of cloud detrainment on the diagnosed properties of cumulus populations, J. Atmos. Sci., 34, 359-366, 1977

Johnson, R. H., Characteristic structure and growth of the non-precipitating cumulus layer over South Florida, Mon. Wea. Rev., 106, 1495-1504, 1978

Johnson, R. H., Diagnosis of convective and mesoscale motions during Phase III of GATE, J. Atmos. Sci., 37, 733-753, 1980

Johnson, W. B., Interregional exchange of air pollution: Model types and application, J. A. P. C. A., 33, 563-574, 1983

Kitchen, M. and Caughey, S. J., Tethered-balloon observations of the structure of small cumulus clouds, Quart. J. R. Met. Soc., 107, 853-874, 1981

Kuo, H. L., On formation and intensification of tropical cyclones through latent heat release by cumulus convection, J. Atmos. Sci., 22, 40-63, 1965



- Kuo, H. L., Further studies of the parameterization of the influence of cumulus convection on large-scale flow, J. Atmos. Sci., 31, 1232-1240, 1974
- Lamb, R., A regional scale (1000 km.) model of photochemical air pollution - Part I: Theoretical formulation, U. S. Environmental Protection Agency Technical Report, Research Triangle Park, N. C., 1983
- Lenschow, D., Pearson, R., Jr. and B. Stankov, Estimating the ozone budget in the boundary layer by use of aircraft measurements of ozone eddy flux and mean concentration, J. Geophys. Res., 86, 7291-7297, 1981
- Lewis, J. M., Test of the Ogura-Cho model on a prefrontal squall line case, Mon. Wea. Rev., 103, 764-778, 1975
- Liu, S. C., Possible effects on tropospheric O<sub>3</sub> and OH due to NO emissions, Geophys. Res. Lett., 4, 325-328, 1977
- Lopez, R. E., The lognormal distribution and cumulus cloud populations, Mon. Wea. Rev., 105, 865-872, 1977
- Manabe, S. and Strickler, R. F., Thermal equilibrium of the atmosphere with a convective adjustment, J. Atmos. Sci., 21, 361-365, 1964
- Manins, P. C., The daytime planetary boundary layer: A new interpretation of Wangara data, Quart. J. R. Met. Soc., 108, 689-705, 1982
- Morton, B. R., Buoyant plumes in a moist atmosphere, J. Fluid Mech., 2, 127-144, 1957
- Nitta, T., Observational determination of cloud mass flux distributions, J. Atmos. Sci., 32, 73-91, 1975
- Ogura, Y. and Cho, H-R., Diagnostic determination of cumulus cloud populations from observed large-scale variables, J. Atmos. Sci., 30, 1276-1286, 1973
- Ogura, Y. and Cho, H-R., On the interaction between the subcloud and cloud layers in tropical regions, J. Atmos. Sci., 31, 1850-1859, 1974
- Ogura, Y., Russell, J. and Cho, H-R., A semi-empirical model of the trade-wind inversion, J. Met. Soc. Japan, 55, 209-220, 1977
- Ooyama, K., A dynamical model for the study of tropical cyclone development, Geofis. Intern., 4, 187-198, 1964
- Ooyama, K., A theory on parameterization of cumulus convection, J. Met. Soc. Japan, 49, 744-756, 1971
- Orville, H. D., Ambient wind effects on the initiation and development of cumulus clouds over mountains, J. Atmos. Sci., 25, 385-403, 1968

- Pielke, R., A three-dimensional numerical model of the sea south Florida, Mon. Wea. Rev., 102, 115-139, 1974
- Pitts, D. E., Reeser, W. K. and Mendlowitz, M. A., Equivalent blackbody temperature of the top of a severe storm, J. Appl. Meteor., 14, 609-618, 1975
- Reynolds, D. W. and Vonder Haar, T. H., A bispectral method for cloud parameter determination, Mon. Wea. Rev., 105, 446-457, 1977
- Reed, R. J. and Recker, E. J., Structure and properties of synoptic-scale wave disturbances in the equatorial western Pacific, J. Atmos. Sci., 28, 1117-1133, 1971
- Riehl, H. and Malkus, J. S., On the heat balance in the equatorial trough zone, Geophysica, 6, 503-538, 1958
- Riehl, H. and Malkus, J. S., Some aspects of hurricane Daisy, 1958, Tellus, 13, 181-213, 1961
- Rodhe, H. and Crutzen, P., Formation of sulfuric and nitric acid in atmosphere during long-range transport, Tellus, 33, 132-141, 1981
- Samson, P. J. and Ragland, K. W., Ozone and visibility reduction Midwest: Evidence for large-scale transport, J. Appl. Met., 16, 1106, 1977
- Schaefer, J. T. and Doswell, C. A., III, On the interpolation vector field, Mon. Wea. Rev., 107, 458-476, 1979
- Scorer, R. S. and Ludlam, F. H., Bubble theory of convection, Quart. J. R. Met. Soc., pp. 79, 94, 10
- Seguin, W. R. and Garstang, M., Some evidence on the structure of the tropical sub-  
33, 660-666, 1976
- Simpson, J., On cumulus entrainment, Atmos. Sci., 28, 449-455, 1971
- Spicer, C. W., Joseph, D. r sources and transport in  
and Tech., 13, 975-98
- Squires, E., Penetr  
1958
- Squires, P. and Turner, updraughts, Tellus, XIV,
- Stommel, H., Entrainment of  
91-94, 1947

- Stommel, H., Entrainment of air into a cumulus cloud II, J. Meteor., **8**, 127-129, 1951
- Stull, R. B., Fair-weather cumulus cloud forecasting using an operational boundary-layer model, personal communication
- Vaughan, W. M., Chan, M., Cantrell, B. and Pooler, F., A study of persistent elevated pollution episodes in the northeastern United States, Bull. Am. Met. Soc., **63**, 258-266, 1982
- White, W. H., Anderson, J. A., Blumenthal, D. L., Husar, R. B., Gillani, N. V. and Husar, J. D., Wilson, W. E., Jr., Formation and transport of secondary air pollutants: Ozone and aerosols in the St. Louis urban plume, Science, **194**, 187-189, 1976
- Wolff, G. T., Liou, P. J., Meyers, R. E., Cederwall, R. T., Wight, G. D., Pasceri, R. E. and Taylor, R. S., Anatomy of two ozone transport episodes in the Washington D. C. to Boston, Massachusetts corridor, Environ. Sci. and Tech., **11**, 506-510, 1977
- Warner, J., The water content of cumuliform cloud, Tellus, **7**, 449-457, 1955
- Warner, J., On steady-state one-dimensional models of cumulus convection, J. Atmos. Sci., **27**, 1035-1040, 1970
- Yanai, M., Esbensen, S. and Chu, J-H., Determination of bulk properties of tropical cloud clusters from large-scale heat and moisture budgets, J. Atmos. Sci., **30**, 611-627, 1973
- Yanai, M., Chu, J-H., Stark, T. and Nitta, T., Response of deep and shallow tropical maritime cumuli to large-scale processes, J. Atmos. Sci., **33**, 976-991, 1976
- Man, O., Parameterization of the dynamics of stable boundary layers nocturnal jets, J. Atmos. Sci., **36**, 792-804, 1979
- r, E. J. and LeMone, M. A., Cumulonimbus vertical velocity events E. Part II: Synthesis and model core structure, J. Atmos. Sci., **38**, 2469, 1980





Pielke, R., A three-dimensional numerical model of the sea breezes over south Florida, Mon. Wea. Rev., 102, 115-139, 1974

Pitts, D. E., Reeser, W. K. and Mendlowitz, M. A., Equivalent blackbody temperature of the top of a severe storm, J. Appl. Meteor., 14, 609-618, 1975

Reynolds, D. W. and Vonder Haar, T. H., A bispectral method for cloud parameter determination, Mon. Wea. Rev., 105, 446-457, 1977

Reed, R. J. and Recker, E. J., Structure and properties of synoptic-scale wave disturbances in the equatorial western Pacific, J. Atmos. Sci., 28, 1117-1133, 1971

Riehl, H. and Malkus, J. S., On the heat balance in the equatorial trough zone, Geophysica, 6, 503-538, 1958

Riehl, H. and Malkus, J. S., Some aspects of hurricane Daisy, 1958, Tellus, 13, 181-213, 1961

Rodhe, H. and Crutzen, P., Formation of sulfuric and nitric acid in the atmosphere during long-range transport, Tellus, 33, 132-141, 1981

Samson, P. J. and Ragland, K. W., Ozone and visibility reduction in the Midwest: Evidence for large-scale transport, J. Appl. Met., 16, 1101-1106, 1977

Schaefer, J. T. and Doswell, C. A., III, On the interpolation of a vector field, Mon. Wea. Rev., 107, 458-476, 1979

Scorer, R. S. and Ludlam, F. H., Bubble theory of penetrative convection Quart. J. R. Met. Soc., pp. 79, 94, 1953

Seguin, W. R. and Garstang, M., Some evidence of the effects of convection on the structure of the tropical subcloud layer, J. Atmos. Sci., 33, 660-666, 1976

Simpson, J., On cumulus entrainment and one-dimensional models, J. Atmos. Sci., 28, 449-455, 1971

Spicer, C. W., Joseph, D. W., Sticksel, P. R. and Ward, G. F., Ozone sources and transport in the northeastern United States, Environ. Sci. and Tech., 13, 975-985, 1979

Squires, E., Penetrative downdraughts in cumuli, Tellus, 10, 381-389, 1958

Squires, P. and Turner, J. S., An entraining jet model for cumulonimbus updraughts, Tellus, XIV, 422-434, 1962

Stommel, H., Entrainment of air into a cumulus cloud, J. Meteor., 4, 91-94, 1947

Stommel, H., Entrainment of air into a cumulus cloud II, J. Meteor., 8, 127-129, 1951

Stull, R. B., Fair-weather cumulus cloud forecasting using an operational boundary-layer model, personal communication

Vaughan, W. M., Chan, M., Cantrell, B. and Pooler, F., A study of persistent elevated pollution episodes in the northeastern United States, Bull. Am. Met. Soc., 63, 258-266, 1982

White, W. H., Anderson, J. A., Blumenthal, D. L., Husar, R. B., Gillani, N. V. and Husar, J. D., Wilson, W. E., Jr., Formation and transport of secondary air pollutants: Ozone and aerosols in the St. Louis urban plume, Science, 194, 187-189, 1976

Wolff, G. T., Liou, P. J., Meyers, R. E., Cederwall, R. T., Wight, G. D., Pasceri, R. E. and Taylor, R. S., Anatomy of two ozone transport episodes in the Washington D. C. to Boston, Massachusetts corridor, Environ. Sci. and Tech., 11, 506-510, 1977

Warner, J., The water content of cumuliform cloud, Tellus, 7, 449-457, 1955

Warner, J., On steady-state one-dimensional models of cumulus convection, J. Atmos. Sci., 27, 1035-1040, 1970

Yanai, M., Esbensen, S. and Chu, J-H., Determination of bulk properties of tropical cloud clusters from large-scale heat and moisture budgets, J. Atmos. Sci., 30, 611-627, 1973

Yanai, M., Chu, J-H., Stark, T. and Nitta, T., Response of deep and shallow tropical maritime cumuli to large-scale processes, J. Atmos. Sci., 33, 976-991, 1976

Zeman, O., Parameterization of the dynamics of stable boundary layers and nocturnal jets, J. Atmos. Sci., 36, 792-804, 1979

Zipser, E. J. and LeMone, M. A., Cumulonimbus vertical velocity events in GATE. Part II: Synthesis and model core structure, J. Atmos. Sci., 37, 2458-2469, 1980

## **APPENDICIES**



## LIST OF APPENDICES

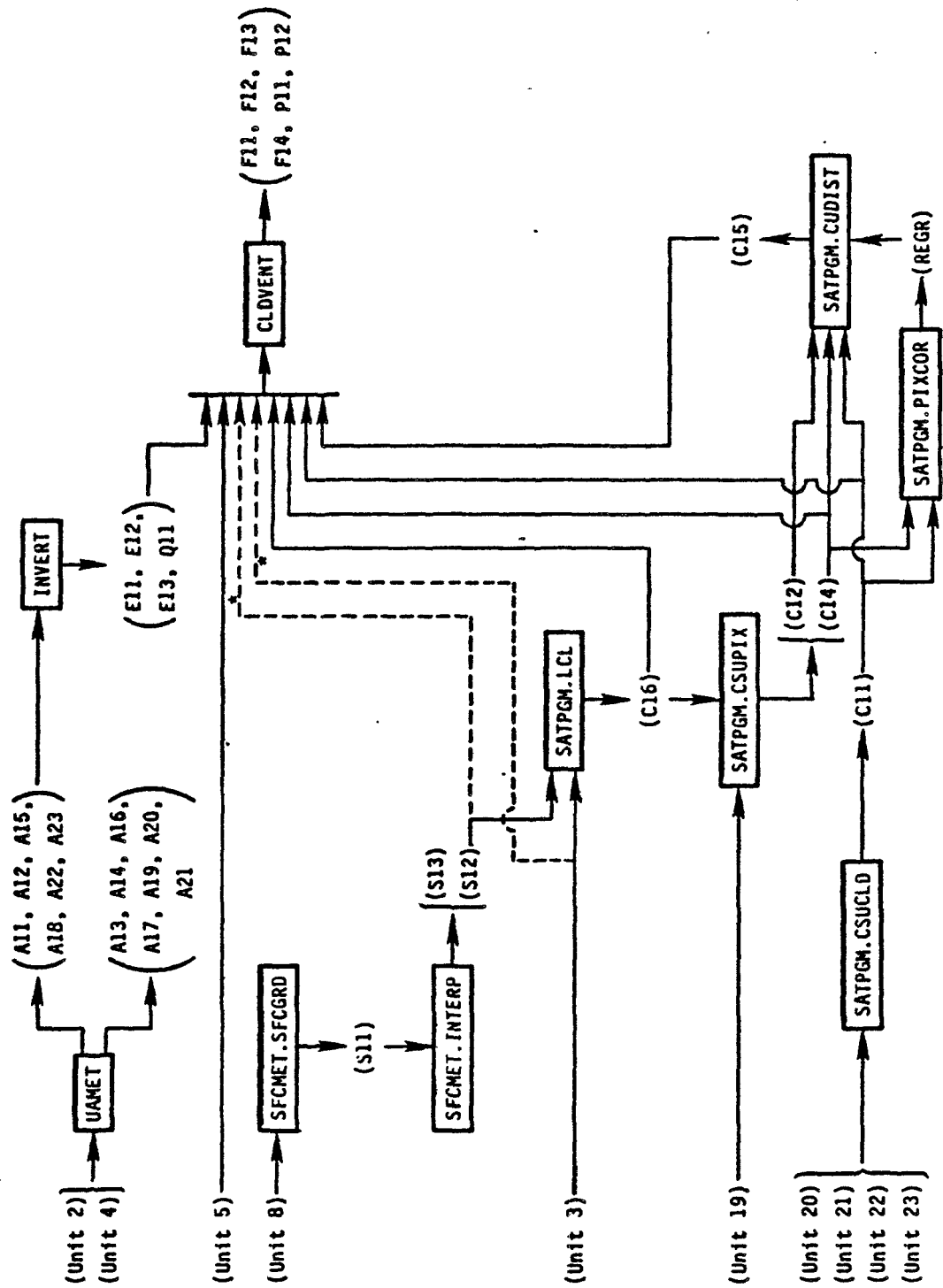
- I. A list and brief description of the files needed to process the required data and perform the necessary cloud-flux computations.....145
- II. Flow diagram of the cloud-base pollutant flux program network.....146
- III. Flow diagram of the cloud-base pollutant flux module.....147
- IV. Cross-reference listing of file specifications used in Appendix II and their corresponding file names, showing what routine created them, and where they are subsequently referenced.....151
- V. Listing and description of each file specified in Appendix IV.....153

## APPENDIX I

A list and brief description of the files needed to process the required data and perform the necessary cloud-flux computations.

<u>Program file</u>	<u>Function</u>
UAMET	This program takes normally obtainable RAOB data (in the 'NEROS' format), produces objectively analyzed fields of the variables on each of several pressure surfaces and interpolates the data in time.
INVERT	This program takes the objectively analyzed fields, on the various pressure surfaces, as determined by UAMET, and changes the data structure so that profiles for each variable are obtained for each small-scale grid cell for each hour of the data.
SFCMET	This program takes normally obtainable surface meteorological data and performs an objective analysis to obtain grid point values of the parameters of interest over the grid. The data is then interpolated in time and space to obtain a small-scale gridded field for each variable for each hour.
SATPGM	This program assimilates the cloud data provided by CSU for each small-scale grid cell, obtains the cloud-base height for each grid cell for each hour of data, and determines the vertical profile of cumulus cloud coverage.
CLDVENT	This program obtains several parameters related to the convective updraft mass flux, occurring in a given grid cell, based on the presence of a cumulus cloud field in the cell and the state of the environment as defined from the objectively analyzed fields, using either the the implicit or explicit models. For a description of the output fields see the description of files (Appendix V, files 37-48).

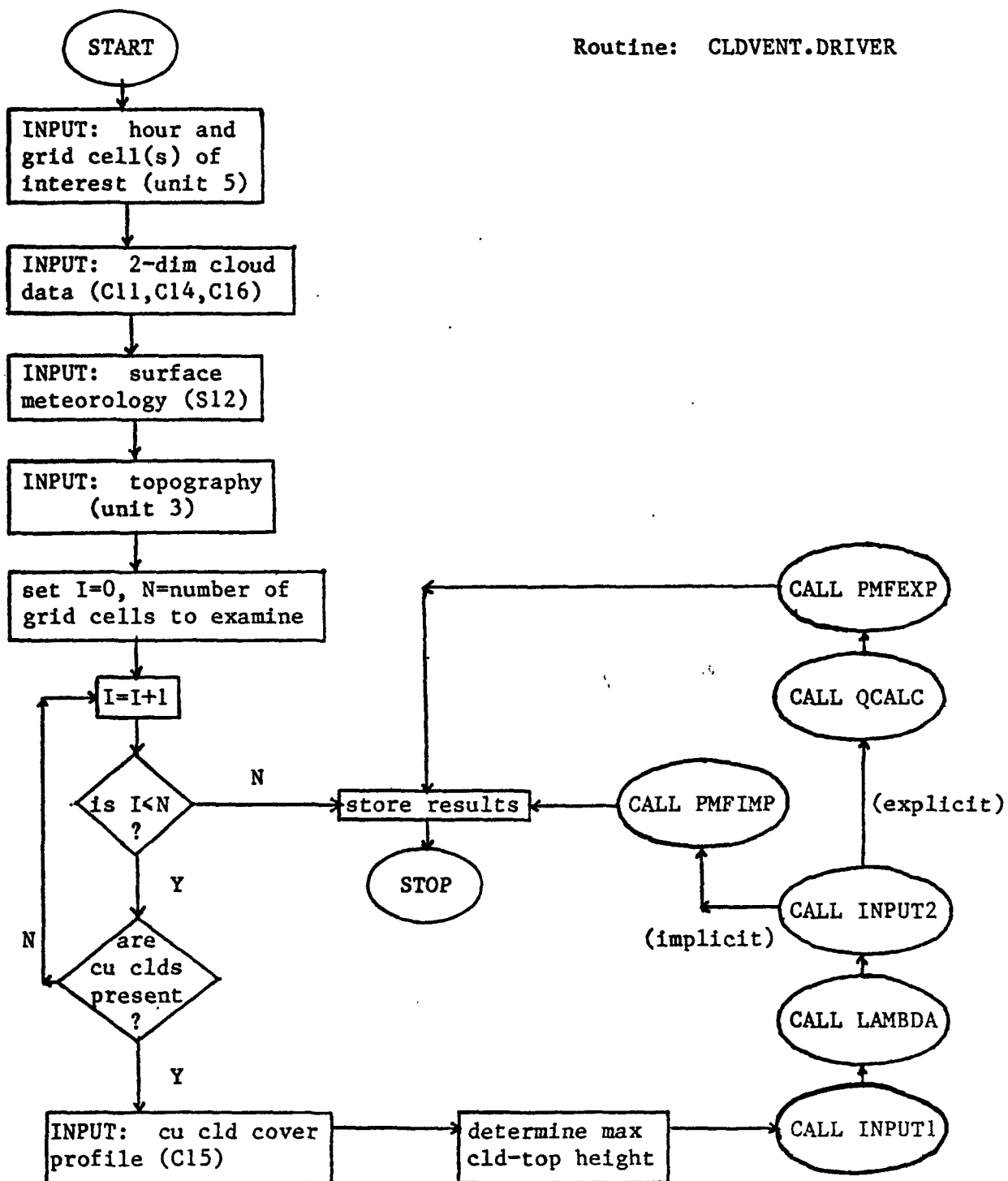
APPENDIX II - Flow diagram of the cloud-base pollutant flux program network

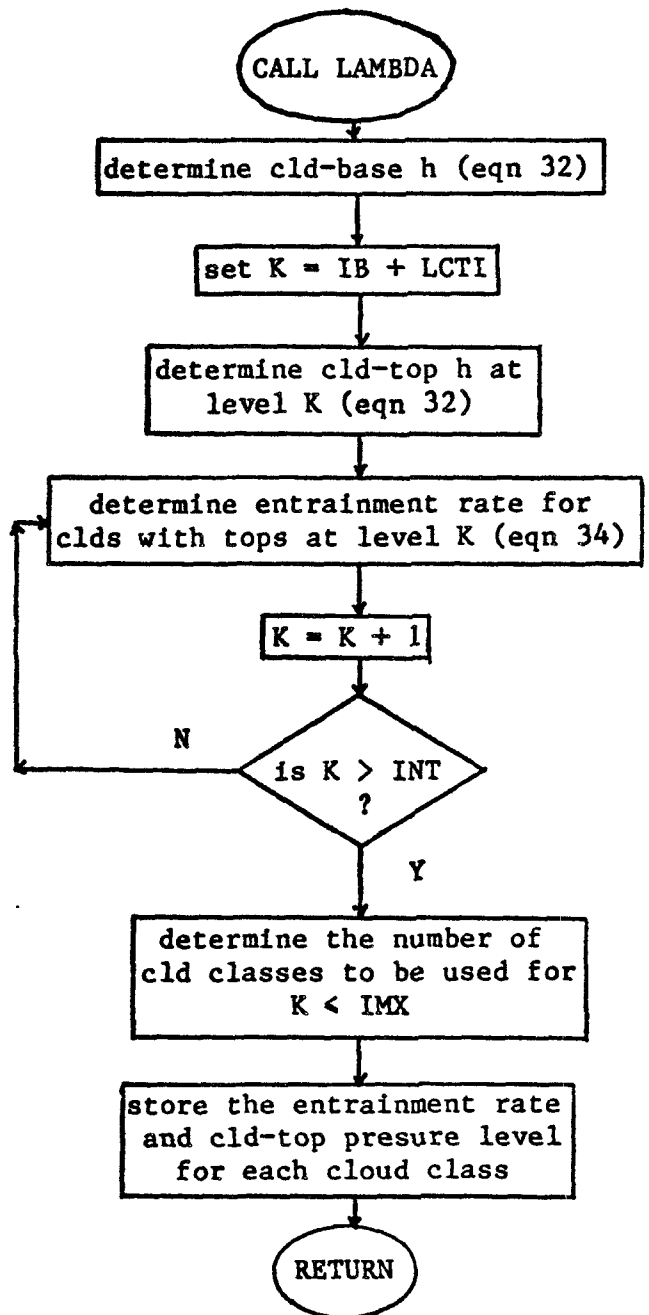
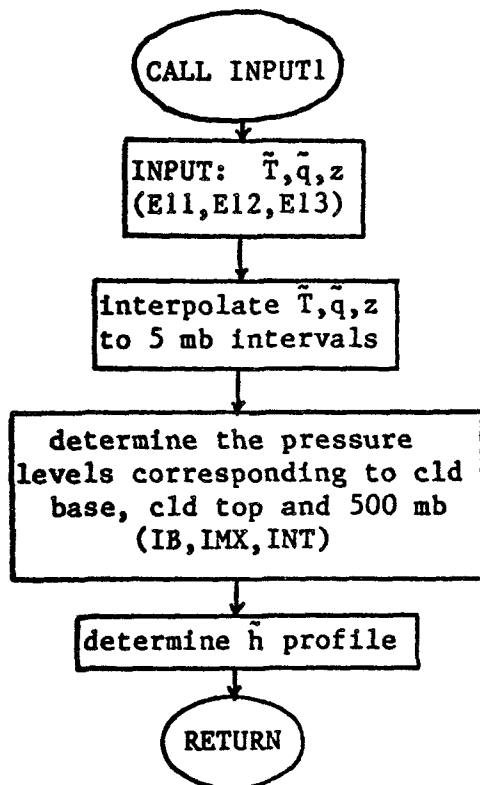


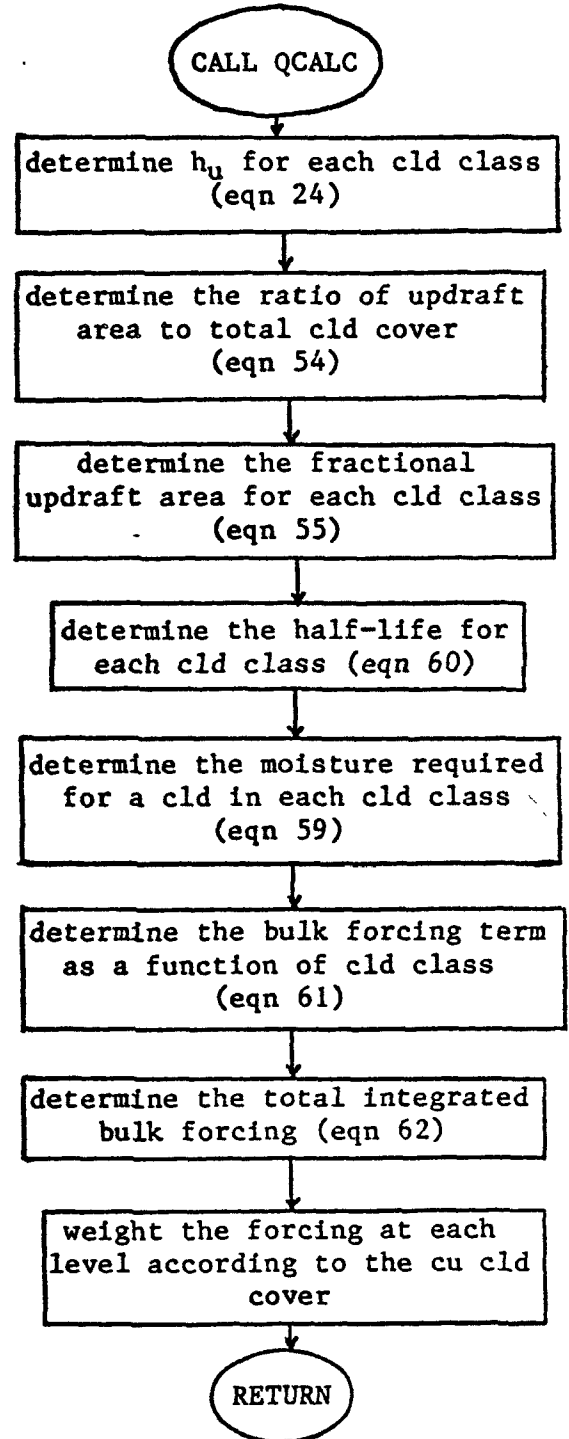
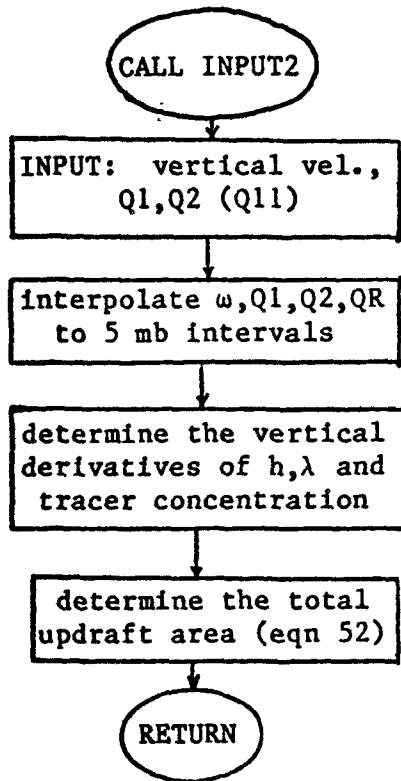
\*This input is optional — see CLDVENT.ADVISE

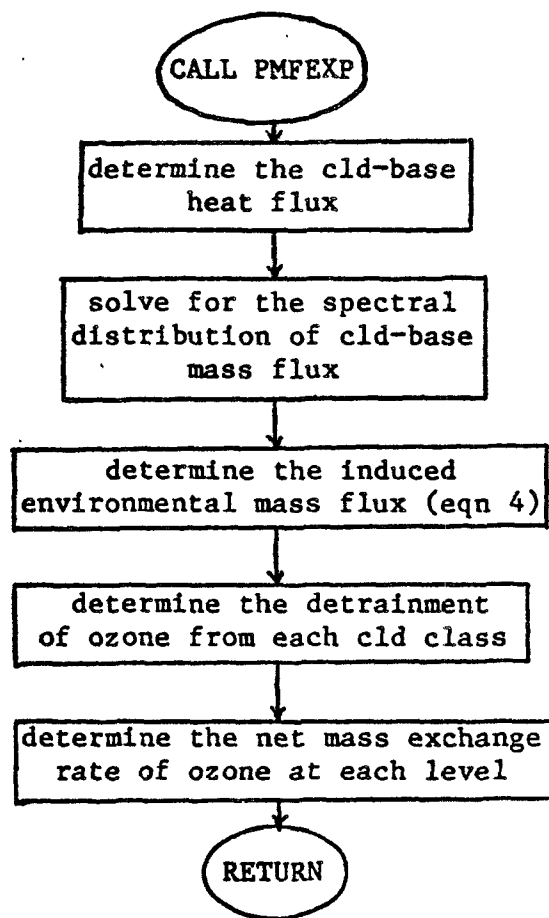
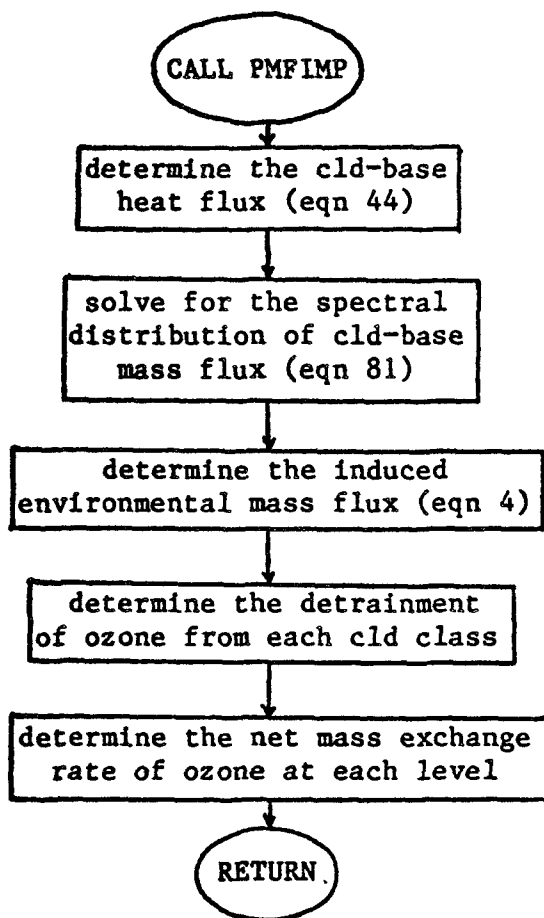
## APPENDIX III

Flow diagram of the cloud-base pollutant flux module









## APPENDIX IV

Cross-reference listing of file specifications used in Appendix II and their corresponding file names, showing what routine created them, and where they are subsequently referenced.

Unit # or File Specification	File Name	Created in Routine	Used in Routine(s)
1. UNIT 2	SEXP1HRLY	-†	UAMET
2. UNIT 3	CELLTOPO	-†	SATPGM.LCL,CLDVENT
3. UNIT 4	SITSEXP1	-†	UAMET
4. UNIT 5	'CARD READER'	-†	UAMET
5. UNIT 8	SEXP1SFCOBS	-†	SFCMET.SFCGRD
6. UNIT 19	CLDFREQPIX	-†	SATPGM.CSUPIX
7. UNIT 20	CLDCOVER-TOT	-†	SATPGM.CSUCLD
8. UNIT 21	CLDCOVER-CUM	-†	"
9. UNIT 22	CUM-AVEHGT	-†	"
10. UNIT 23	CUM-PKHGT	-†	"
11. A11	LSZSEXP1	UAMET	UAMET, INVERT
12. A12	LSTSEXP1	"	" "
13. A13	LSPTSEXP1	"	"
14. A14	LSTDSEXP1	"	"
15. A15	LSQSEXP1	"	" , INVERT
16. A16	LSUSEXP1	"	"
17. A17	LSVSEXP1	"	"
18. A18	LSWSEXP1	"	" , INVERT
19. A19	SEXP1DIVORT	"	"
20. A20	LSAVSESEXP1	"	"
21. A21	LSAVQSEXP1	"	"
22. A22	LSQ1SEXP1	"	" , INVERT
23. A23	LSQ2SEXP1	"	" , "
24. A24	UTILITY1	"	"
25. E11	SSTSEXP1	INVERT	CLDVENT
26. E12	SSQSEXP1	"	"
27. E13	SSZSEXP1	"	"
28. Q11	SSWQ1Q2SEXP1	"	"
29. S11	SEXP1SFCLG	SFCMET.SFCGRD	SFCMET.INTERP
30. S12	SEXP1SFC	SFCMET.INTERP	SATPGM.LCL,CLDVENT
31. S13	SEXP1SFCLGHR	"	"
32. C11	SEXP1CSUCLDS	SATPGM.CSUCLD	SATPGM.PIXCOR, SATPGM.CUDIST, CLDVENT
33. C12	SEXP1CSUPIX	SATPGM.CSUPIX	SATPGM.CUDIST
34. C14	SEXP1TOTPIX	"	SATPGM.PIXCOR, SATPGM.CUDIST, CLDVENT
35. C15	SEXP1CUMCOVD	SATPGM.CUDIST	CLDVENT
36. C16	SEXP1CLDBHTS	SATPGM.LCL	SATPGM.CSUPIX, CLDVENT
37. F11	FLUXPARAMIMP	CLDVENT	"
38. F11	FLUXPARAMEXP	"	"



39.	F12	MBOFPIMP	CLDVENT
40.	F12	MBOFPEXP	"
41.	F13	O3BUDIMP	"
42.	F13	O3BUDEXP	"
43.	F14	MFBUDIMP	"
44.	F14	MFBUDEXP	"
45.	P11	CBPLIMP	"
46.	P11	CBPLEXP	"
47.	P12	CSTATSIMP	"
48.	P12	CSTATSEXP	"
49.	REGR <sup>s</sup>		

↑ These files are assumed to be supplied by the user.

REGR<sup>s</sup> This is not an actual file, but is the output displayed on a CRT. The required regression coefficients are to be read from the display and inserted into routine SATPGM.CUDIST via a data statement.

## APPENDIX V

Listing and description of each file specified in Appendix IV

File Name	Description
1. SEXPIHRLY	Hourly RAOB data from 7/21/81 12Z through 7/23/81 12Z for stations within the lat-lon boundaries of 45° - 25° N, 91° - 60° W in NEROS format.
2. CELLTOPO	Grid averaged topography (M) for each grid cell in the lat-lon region of 38° - 34° N, 81° - 76° W. Each cell has the dimensions of 1/6° lat X 1/4° lon.
3. SITESEXP1	Station ID, lat, lon and altitude (m) for each RAOB station in the space-time window described in SEXPIHRLY.
4. 'CARD READER'	Hour (GMT) and grid cell(s) of interest.
5. SEXPISFCOBS	Surface meteorological data from 7/22/81 12Z through 7/23/81 6Z for stations within the lat-lon boundaries of 39° - 33° N, 82.5° - 75° W.
6. CLDFREQPIX	Frequency distribution of cloud-top heights as given by IR pixel data for 1200 LST through 2300 LST for each grid cell (1/6° lat X 1/4° lon) within the region of 38° - 34° N, 81° - 76° W. The pixel data are given at 500 ft intervals.
7. CLDCOVER-TOT	Fractional cloud cover of all clouds for each grid cell, time window given in CLDFREQPIX.
8. CLDCOVER-CUM	Fractional cloud cover of cumulus clouds, for each grid cell, for the space-time window in CLDFREQPIX.
9. CUM-AVEHGT	Average cumulus height, for each grid cell, for the space-time window given in CLDFREQPIX.
10. CUM-PKHGT	Peak cumulus height, for each grid cell, for the space-time window given in CLDFREQPIX.
11. LSZSEXP1	Hourly geopotential height data (m) for each of the large-scale (synoptic) grid points, at 25 mb intervals from 500 - 1000 mb, from 7/22/81 12Z through 7/23/81 12Z, for the region bounded by 41° - 31° N, 86° - 71° W. Each grid cell has the dimensions of 2.0° lat X 2.5° lon.

12. LSTSEXP1      Hourly temperature data ( $K^{\circ}$ ) for each grid cell as defined in the pressure-space-time window specified in LSZSEXP1.
13. LSPTSEXP1    Hourly isentropic analysis data for the 315 K surface for the space-time window specified in LSZSEXP1. For each hour, the following information given for each grid point: pressure (mb), specific humidity (g/kg), u-comp of wind (m/s), v-comp of wind (m/s), Montgomery stream function (J/g).
14. LSTDSEXP1    Hourly dew-point temperature data (k) for each grid cell as defined in the pressure-space-time window specified in LSZSEXP1.
15. LSQSEXP1     Hourly specific humidity data (g/kg) for each grid cell as defined in the pressure-space-time window specified in LSZSEXP1.
16. LSUSEXP1     Hourly data for the u-comp of wind (m/s), for each grid cell as defined in the space-time window specified in LSZSEXP1, with 50 mb intervals from 500 mb to 1000 mb.
17. LSVSEXP1     Hourly data for the v-comp of wind (m/s) for each grid cell as defined in the pressure-space-time window specified in LSUSEXP1.
18. LSWSEXP1     Hourly data for large-scale environmental vertical velocity (mb/hr) for each grid cell as defined in the pressure-space-time window specified in LSUSEXP1.
19. SEXPIDIVORT   Hourly vorticity and divergence data (1/s) for the space-time window specified in LSUSEXP1. At each 50 mb level from 500 mb to 1000 mb, 3 sets of vorticity and divergence data are given for the large-scale grid points. The first set is derived from the initial u and v gridded wind component data. The second set is derived from the Bellamy triangle technique. The third set is derived from the final u and v gridded data resulting from the Schaefer-Doswell analysis.
20. LSAVSESEXP1   Hourly, layer-averaged static energy data (J/g) for each grid cell as defined in the pressure-space-time window specified in LSUSEXP1.
21. LSAVQSEXP1    Hourly, layer-averaged specific humidity data (g/kg) for each grid cell as defined in the pressure-space-time window specified in LSUSEXP1.

22. LSQ1SEXP1      Hourly data for each component of the large-scale dry static energy budget (deg/day) for each grid cell as defined in the pressure-space-time window in LSUSEXP1.
23. LSQ2SEXP1      Hourly data for each component of the large-scale moisture budget (deg/day) for each grid cell as defined in the pressure-space-time window in LSUSEXP1.
24. UTILITY1        Working file to facilitate the computations of Q1 and Q2.
25. SSTSEXP1        Hourly profiles of temperature data (K) for each of the small-scale grid cells from 7/22/81 12Z through 7/23/81 12Z for the region bounded by 38° - 34° N, 81° - 76° W. Each grid cell has the dimensions of 1/6° lat X 1/4° lon. Data are given at 25 mb intervals from 500 mb to 1000 mb.
26. SSQSEXP1        Hourly profiles of specific humidity data (g/kg) for each grid cell as defined in the pressure-space-time window specified in SSTSEXP1.
27. SSZSEXP1        Hourly profiles of geopotential height data (m) for each grid cell as defined in the pressure-space-time window specified in SSTSEXP1.
28. SSWQ1Q2SEXP1   Hourly data for the large-scale environmental vertical velocity (mb/hr), Q1, and Q2 (deg/day) are given at 50 mb intervals from 500 mb to 1000 mb for each grid cell as defined in the space-time window specified in SSTSEXP1.
29. SEXP1SFCLG      Gridded 3-hourly surface data for each grid cell for 7/22/81 12Z through 7/23/81 6Z for the region bounded by 38° - 34° N, 81° - 76° W. The grid cells have the dimensions of 1.0° lat X 1.25° lon. The data at each time level are: sea level press (mb), station press (mb), u-comp of wind (m/s), v-comp of wind (m/s), temp (K), dew-point temp (K).
30. SEXP1SFC        Hourly surface data for each grid cell for 7/22/81 12Z through 7/23/81 6Z for the region bounded by 38° - 34° N, 81° - 76° W. The grid cells have the dimensions of 1/6° lat X 1/4° lon. The data component given for each hour are the same as in SEXP1SFCLG.
31. SEXP1SFCLGHR    Hourly surface data for each grid cell as defined in the space-time window specified in SEXP1SFCLG. The data components given for each hour are the same as in SEXP1SFCLG.

32. SEXPLCSUCLDS      Hourly cloud data for each grid cell from 1200 LST through 2300 LST on 7/22/81 within the lat-lon region of  $38^{\circ}$  -  $34^{\circ}$  N,  $81^{\circ}$  -  $76^{\circ}$  W. Each cell has the dimensions of  $1/6^{\circ}$  lat X  $1/4^{\circ}$  lon. The four data fields, for each hour, from the files CLDCOVER-TOT, CLDCOVER-CUM, CUM-AVEHGT, and CUM-PKHGT have been assimilated into this one direct access file.
33. SEXPLCSUPIX      This is a direct access file containing the data of CLDFREQPIX.
34. SEXPLTOTPIX      Hourly, vertically integrated IR pixel counts for each grid cell as defined in the space-time window of SEXPLCSUCLDS.
35. SEXPLCUMCOVD      Hourly profiles of the fractional cumulus cloud coverage for each grid cell as defined in the space-time window of SEXPLCSUCLDS. The data are given at 500 ft intervals.
36. SEXPLCLDBHTS      Hourly cloud-base heights (msl) for each grid cell as defined in the space-time window of SEXPLCSUCLDS.
37. FLUXPARAMIMP      Hourly, grid cell averaged output from the implicit version of CLDVENT for any grid cell from 1200 LST through 2300 LST on 7/22/81 within the bounds of  $38^{\circ}$  -  $34^{\circ}$  N,  $81^{\circ}$  -  $76^{\circ}$  W. The grid cells have dimensions of  $1/6^{\circ}$  lat X  $1/4^{\circ}$  lon. For each cloud class determined from the model 7 components are given: (1) cloud-base mass flux as a function of entrainment rate (mb-km/day). (2) entrainment rate interval (1/km). (3) entrainment rate (1/km). (4) normalized mass flux. (5) the derivative of the entrainment rate profile with respect to pressure at the cloud top (1/km-mb). (6) incloud ozone concentrations at the cloud top (ppbv). (7) no data given for implicit model for this component.
38. FLUXPARAMEXP      Hourly, grid cell averaged output from the explicit version of CLDVENT. The data structure is identical to that of FLUXPARAMIMP with the exception for component (7): fractional coverage of updraft area.
39. MBOFPIMP      Hourly, grid cell averaged output from the implicit version of CLDVENT for any grid cell in the space-time window as defined in FLUXPARAMIMP. For each cloud class 2 components are given: (1) cloud-top pressure (mb). (2) cloud-base mass flux as a function of cloud-top pressure (1/day).
40. MBOFPEXP      Hourly, grid cell averaged output from the explicit version of CLDVENT. The data structure is identical to that of MBOFPIMP.

41. O3BUDIMP Hourly grid cell averaged output from the implicit version of CLDVENT for any grid cell in the space-time window as defined in FLUXPARAMIMP. For each cloud class 4 components are given: (1) cloud-top pressure (mb). (2) cloud-top detrainment rate of ozone (ppbv/hr). (3) vertical net mass exchange rate of ozone ( $\mu\text{g}$  ozone/hr) at the cloud-top pressure. (4) induced environmental transport of ozone, at the cloud-top pressure, caused by the upward mass flux (ppbv/hr).
42. O3BUDEXP Hourly, grid cell averaged output from the explicit version of CLDVENT. The data structure is identical to that of O3BUDIMP.
43. MFBUDIMP Hourly, grid cell averaged output from the implicit version of CLDVENT for any grid cell in the space-time window as defined in FLUXPARAMIMP. For each cloud class 4 components are given: (1) cloud-top pressure (mb). (2) total upward convective mass flux at the cloud-top pressure (mb/hr). (3) induced environmental mass flux at the cloud-top pressure, caused by the upward mass flux (mb/hr). (4) large-scale (synoptic mass flux (mb/hr) at the cloud-top pressure (as determined from RAOB data).
44. MFBUDEXP Hourly, grid cell averaged output from the explicit version of CLDVENT. The data structure is identical to that of MFBUDIMP.
45. CBPLIMP Hourly, grid cell averaged output from the implicit version of CLDVENT for any grid cell in the space-time window as defined in FLUXPARAMIMP. The value of the total net ozone exchange rate at cloud base ( $\mu\text{g}$  ozone/hr) is given.
46. CBPLEXP Hourly, grid cell averaged output from the explicit version of CLDVENT. The data structure is identical to that of CBPLIMP.
47. CSTATSIMP Hourly, grid cell averaged output from the implicit version of CLDVENT for any grid cell in the space-time window as defined in FLUXPARAMIMP. For each hour, 3 data fields are given: (1) Convective cloud-base heat flux ( $\text{W}/\text{m}^2$ ). (2) no data given for the implicit model. (3) total fractional updraft area.
48. CSTATSEXP Hourly, grid cell averaged output from the explicit version of CLDVENT. The data structure is identical to that of CSTATSIMP with the exception of component (2): ratio of updraft area to total cloud cover.

<b>TECHNICAL REPORT DATA</b> <i>(Please read Instructions on the reverse before completing)</i>		
1. REPORT NO.	2.	3. RECIPIENT'S ACCESSION NO.
4. TITLE AND SUBTITLE  THE VERTICAL REDISTRIBUTION OF A POLLUTANT TRACER DUE TO CUMULUS CONVECTION		5. REPORT DATE 12/84 (Approved)
		6. PERFORMING ORGANIZATION CODE
7. AUTHOR(S)  John A. Ritter and Donald H. Stedman		8. PERFORMING ORGANIZATION REPORT NO.
9. PERFORMING ORGANIZATION NAME AND ADDRESS University of Michigan Department of Atmospheric and Oceanic Sciences Ann Arbor, Michigan 48109		10. PROGRAM ELEMENT NO. CDWA1A/02 - 0651 (FY-85)
		11. CONTRACT/GRANT NO.  CA CR807485
12. SPONSORING AGENCY NAME AND ADDRESS Atmospheric Sciences Research Laboratory--RTP, NC Office of Research and Development U.S. Environmental Protection Agency Research Triangle Park, North Carolina 27711		13. TYPE OF REPORT AND PERIOD COVERED Final (1980-84)
		14. SPONSORING AGENCY CODE EPA/600/09
15. SUPPLEMENTARY NOTES		
16. ABSTRACT  Mathematical formalisms that incorporate the physical processes responsible for the vertical redistribution of a conservative pollutant tracer due to a convective cloud field are presented. Two modeling approaches are presented differing in the manner in which the cloud fields are forced. In the first or implicit approach, the vertical cloud development is limited by the satellite observed value, and cloud forcing is determined from synoptic-scale heat and moisture budgets. In the explicit approach, the vertical development is similarly limited, but the forcing functions are obtained by explicitly incorporating the vertical distribution of cumulus cloud cover, thereby dynamically incorporating the influences of sub-synoptic scale phenomena. The two approaches give internally consistent results and give similar results for the convective mass flux. The manner in which the upward mass flux is apportioned to the various cloud classes, however, differs as consequence of the different vertical profile of forcing functions used. The explicit model gave more reasonable profiles but the predictions are highly sensitive to input conditions. The implicit model, was somewhat less sensitive to its input parameters if the data are prepared judiciously. This study shows that the concentration increase in the cloud-layer due to the venting action of cumulus clouds can be as, if not more important than, the in-situ production and this process should therefore be incorporated in regional-scale transport models.		
17. KEY WORDS AND DOCUMENT ANALYSIS		
a. DESCRIPTORS	b. IDENTIFIERS/OPEN ENDED TERMS	c. COSATI Field/Group
18. DISTRIBUTION STATEMENT  RELEASE TO PUBLIC	19. SECURITY CLASS (This Report) UNCLASSIFIED 20. SECURITY CLASS (This page) UNCLASSIFIED	21. NO. OF PAGES  22. PRICE